Atmospheric Regimes: Past, Present and Future

by

Qiaobin Teng

B.Sc., Nanjing Institute of Meteorology, 1992
M.Sc., Nanjing Institute of Meteorology and
Chinese Academy of Meteorological Sciences, 1995

A Dissertation Submitted in Partial Fulfillment of the
Requirements for the Degree of

Doctor of Philosophy

in the School of Earth and Ocean Sciences

Co-supervisors: Drs. John Fyfe and Adam Monahan

Abstract

This study concerns Northern Hemisphere low-frequency atmospheric regimes as they have been observed in the recent past and simulated for the near future. Nonlinear principal component analysis is applied to observed and simulated daily sea level pressure. The objectives are to: 1) characterize the three dimensional spatial, temporal and dynamical signature of the regimes; 2) assess a global climate model reproduction of the regimes and 3) determine the simulated regime response to enhanced levels of greenhouse gases and sulphate aerosols. The main conclusions are that the atmosphere supports three regime states with an average residence time of about seven days. Low- and high-frequency dynamics are both involved in the formation, maintenance and decay of the regimes. The model produces three similar regimes with similar residence times and underlying dynamics. Under enhanced levels of greenhouse gases and sulphate aerosols both the regime residence times and spatial structures are predicted to change. This is in contrast to some earlier studies which suggest that only the residence times would be affected. Finally, it is demonstrated that an overly coarse characterization of regime behavior is obtained when the data is smoothed over time-scales much longer than the intrinsic residence time of the regimes. Importantly, this result helps to reconcile some earlier contradictory results.

Examiners:

Table of Contents

List of Tables

List of Figures

Acknowledgments

I would like to express my deep gratitude to my co-supervisors Dr. John Fyfe and Dr. Adam Monahan for their guidance, insightful advice, invaluable help and support during the course of my doctoral research. I am indebted to Dr. John Fyfe for his efforts and many hours he has spent with me on discussing and polishing the dissertation. My special thanks also go to my committee members: Drs. Greg Flato, Chris Garrett and Andrew Weaver for their suggestions and their time on my committee. I would also like to thank Dr. Hisashi Nakamura for email discussions on some dynamical diagnoses.

I wish to extend my sincere thanks to the scientists and staff at the Canadian Centre for Climate Modelling and Analysis. They have provided me with great working facilities and a very friendly studying environment. Particularly, I thank Mike Berkley, Fouad Majaess, Dr. Slava Kharin, Dr. Steve Lambert, Dr. Francis Zwiers, Debby Scott, Deborah Tubman and Warren Lee for their kind help with computer problems, data, software and scientific questions and administrative work. I am very grateful for the LaTex help of this dissertation provided by Michael Roth. I also wish to thank all my colleagues and friends, past and present, for their help and care during my Ph.D. study.

The Canadian Climate Variability Research Network is gratefully acknowledged for their financial support.

Finally, special thanks go to my husband, Bin Yu, and my parents for their love, understanding, encouragement and support.

Chapter 1

Introduction

The atmosphere exhibits variability on a range of time scales. High-frequency variations, with periods less than a week or so, are associated with synoptic-scale transient eddies such as those seen on daily weather maps. Low-frequency variations, with periods greater than 10 days or so, involve large-scale coherent patterns of variability such as the North Atlantic Oscillation (NAO) and the North Pacific Oscillation (NPO). In the past, studies of atmospheric low-frequency variability typically assumed linear relationships between the variables of concern. The NAO and NPO have all been identified under this assumption of linearity. However, due to the inherent nonlinear processes in the atmosphere, that is, the governing equations are nonlinear, the superposition of solutions from linear approaches are unable to appropriately reveal the nonlinear atmospheric variability. With the recent development of more sophisticated nonlinear statistical techniques it has become increasingly apparent that atmospheric variability should be treated as such. In this study we apply one of these nonlinear techniques to characterize the dominant nonlinear modes of atmospheric low-frequency variability, as well as the dynamics which is responsible for them. We

also determine how these nonlinear modes and their dynamics may change in the future under global warming.

As noted, most previous studies of atmospheric low-frequency variability have proceeded under the assumption of linearity. An early example is the landmark paper of Walker and Bliss (1932). Here the authors applied linear correlation analysis to widely dispersed station time series of wintertime-mean sea level pressure (SLP) and surface air temperature to identify the NAO and NPO. With the increase in surface and upper-air observations these linear modes of variability have been characterized in greater and greater detail, and more and more linear modes identified. For example, Wallace and Gutzler (1981) applied linear correlation analysis to SLP and mid-tropospheric height data and Principal Component Analysis (PCA) or Empirical Orthogonal Function (EOF) Analysis to the corresponding correlation matrix and obtained a wide array of linear modes including the Pacific North American pattern (PNA) and the eastern Atlantic pattern. A useful review of the early linear studies can be found in Panagiotopoulos et al. (2002). Recently, the PCA-based SLP pattern known as the Arctic Oscillation (AO) has received considerable attention (e.g., Thompson and Wallace 1998; 2000). A key feature of the AO is its approximately zonally symmetric appearance characterized by a primary center of action over the Arctic and oppositely-signed anomalies over mid-latitudes (Figure 1.1). Recently, some researchers have questioned the actual existence of the AO as a distinct physical entity for a number of reasons. For example, 1) regressing or correlating the observed Northern Hemisphere (NH) wintertime monthly SLP anomalies upon the leading EOF time series from both the Atlantic and Pacific sector, Deser (2000) found that patterns were not of hemispheric extent. 2) Ambaum et al. (2001) confirm the weak correlation between the Pacific and Azores centers of action of the AO, studied

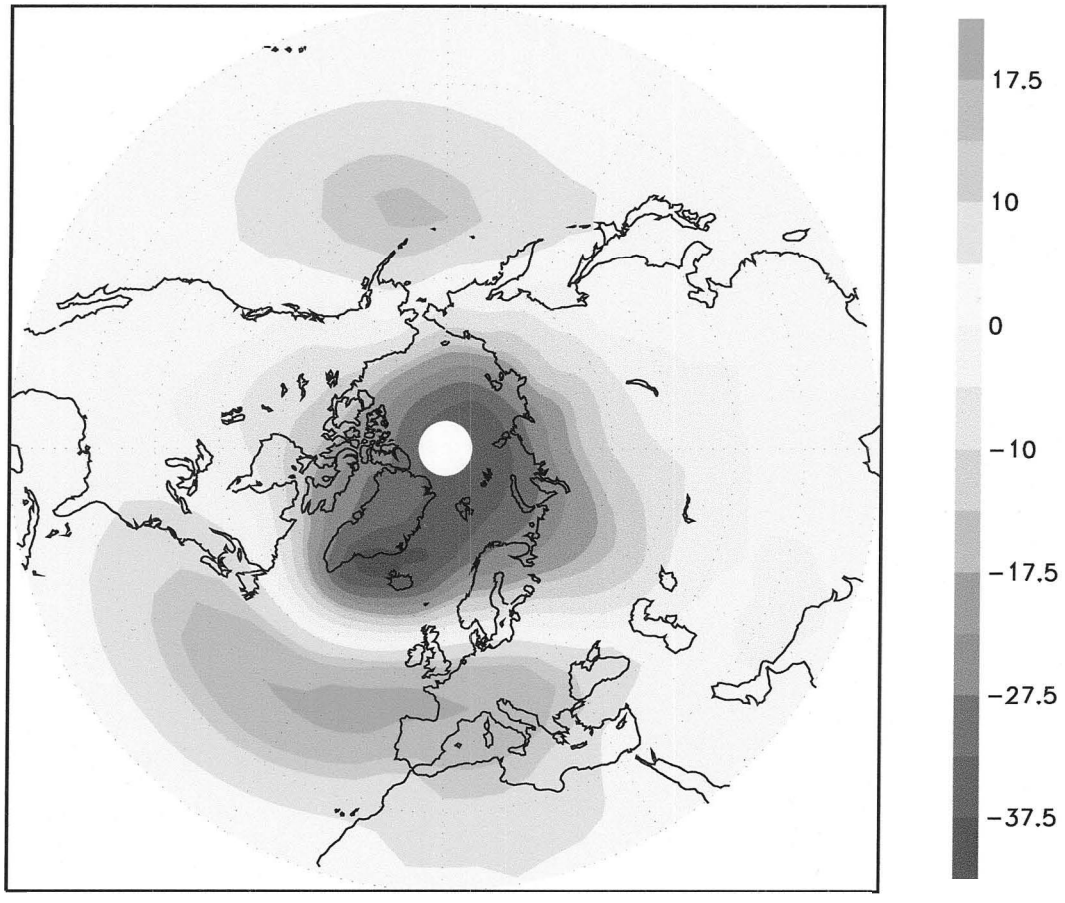

Figure 1.1: Geopotential height at 1000 hPa regressed on the standardized AO index based upon monthly data for Jan 1958-Dec 1997. Units are in meters per standard deviation of the AO time series. This figure was downloaded from http://horizon.atmos.colostate.edu/ao/Figures, and it originally appeared in Thompson and Wallace (2000).

by Deser (2000). They further demonstrate that the lack of teleconnections arises from the inherent limitations of the EOF method itself. 3) Dommenget and Latif (2002) show that different linear statistical methods of representing SLP variability over the NH give different results. 4) Monahan et al. (2001; 2003) also show that the AO's shortcomings follow, in large measure, from the underlying assumption of linearity.

Over the past several decades the concept of atmospheric regimes (also called weather, planetary and climate regimes) has emerged in dynamical meteorology. Atmospheric regimes represent preferred states of atmospheric variability, for which atmospheric blocking is a good example. Atmospheric blocks appear as quasi-stationary, long-lived (from several days to even weeks) large-scale circulation patterns often associated with extreme weather (e.g., long dry and warm spells). Modern interest in regimes began with Charney and DeVore (1979) who used a highly simplified nonlinear barotropic model to obtain multiple equilibria with the same fixed external forcing. One stable equilibrium exhibits a weak wave structure and a strong zonal flow, while the other exhibits a strong wave structure and a weak zonal flow. The authors related these model equilibria to zonal and blocked atmospheric states identified many years earlier in observations (e.g., Rex 1950; Namias 1950; 1964 and Bauer 1951).

Motivated by the theoretical, and fundamentally nonlinear, results of Charney and DeVore (1979, the nonlinearity here refers to nonlinear wave-mean flow interactions), researchers have begun approaching the characterization of atmospheric variability with nonlinear statistical techniques. Examples include: probability density function (PDF) estimation (e.g., Hansen and Sutera 1986; Molteni et al. 1990; Kimoto and Ghil 1993a; Corti et al. 1999; Smyth et al. 1999) and cluster analysis (e.g., Mo and

Ghil 1988; Cheng and Wallace 1993; Michelangeli et al. 1995).

In the PDF estimation method, maxima of the PDF are sought. Each regime is formed by the points in the neighborhood of a PDF maximum, which represents a high probability of occurrence. As an example of this category Kimoto and Ghil (1993a) identified four NH regimes, namely, PNA, reversed PNA, zonal phase NAO and blocked phase NAO using 37 winters of NH 10-day low-pass filtered anomalous heights at 700 hPa. Cluster analysis localizes high concentrations of points (or maps), called clusters. There are two main types of clustering algorithm: hierarchical and partitioning as reviewed in Ghil and Robertson (2002). In hierarchical algorithms (e.g., Cheng and Wallace 1993), one builds a classification tree iteratively, starting from single data points and merging them into clusters according to a similarity criterion such as squared Euclidean distance or pattern correlation. In partitioning algorithms (e.g., Michelangeli et al. 1995), a prescribed number of clusters is chosen, and data points are agglomerated around kernels initially chosen from random seeds. The kernels are iteratively modified so as to globally minimize the data scatter about the kernels. As an example of this second category Cheng and Wallace (1993) identified three hemispheric regimes (closely resembling three of the four regimes obtained in Kimoto and Ghil 1993a) using 40 winters of NH 10-day low-pass filtered 500 hPa height field. These results have been reproduced in Wallace (1996) using updated observations.

An example from the two categories of nonlinear techniques is given in Figure 1.2. The right column is from Smyth et al. (1999), who apply a mixture model that approximates the PDF of 44 winters of NH 10-day low-pass filtered anomalous 700 hPa heights by the sum of a small number of multivariate Gaussians. Their results confirmed the same three hemispheric regimes found in Wallace (1996) discussed

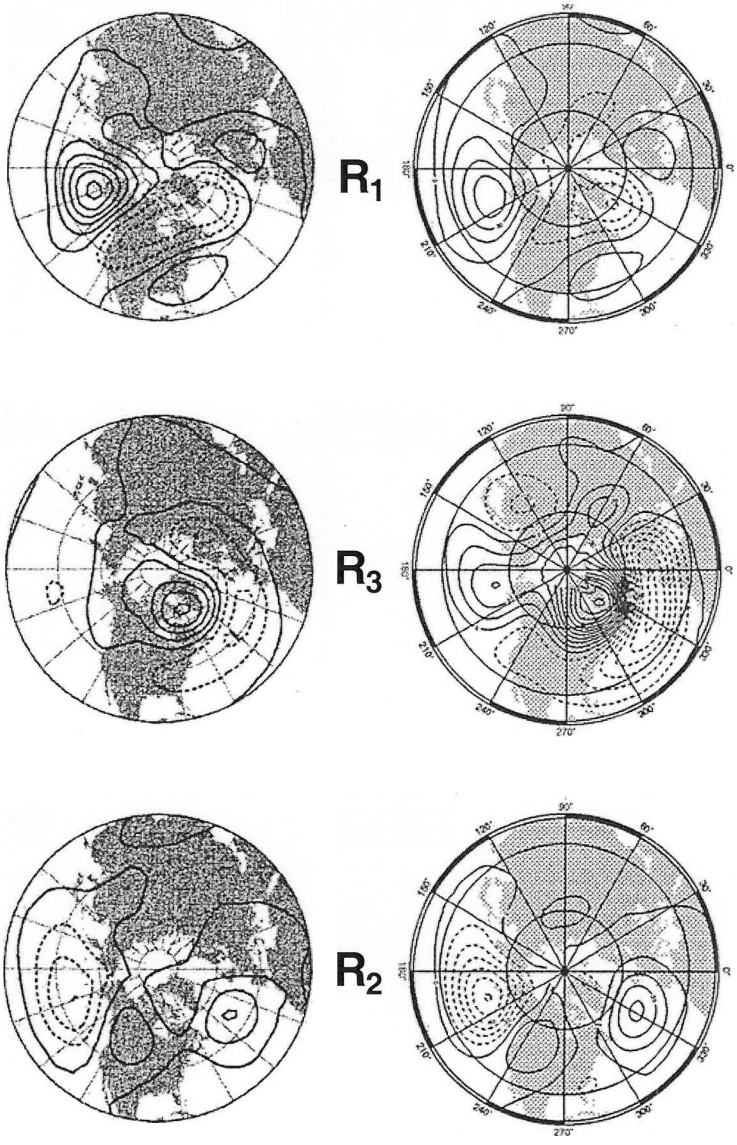

Figure 1.2: Height anomaly maps for the three regimes identified by Wallace (1996) (left) and Smyth et al. (1999) (right). Contour intervals are 50 m (left) for anomalous Z_{500} (left) and 15 m for anomalous Z_{700} (right). Negative contours are dashed and the zero and positive contours are solid. Adapted from Smyth et al. (1999).

above, which are shown in the left column. The top panels in Figure 1.2 show a regime characterized by a strong positive anomaly in the North Pacific. The middle panels show a negative phase NAO-like regime with anomaly centers over Greenland and the Azores. Finally, the bottom panels show a regime structure characterized by negative anomalies over the North Pacific and a weaker positive center over the Rockies. For future reference these regime patterns are labelled R_1, R_3 and R_2, respectively.

In this study we will utilize a new and very powerful nonlinear statistical technique known as Nonlinear Principal Component Analysis (NLPCA; Monahan 2000a). As discussed in Monahan (2000a) this technique has a number of desirable characteristics including: 1) it is a natural generalization of linear PCA and 2) it allows for the straightforward characterization of temporal evolution. This technique has been applied to simulated data (Monahan et al. 2000c) and observations (Monahan et al. 2001; 2003) and in both cases has confirmed that atmospheric low-frequency variability is manifestly regime-like. In these studies and this one, regimes are defined as those averaged maps (or points) in the neighborhood of PDF peaks of NLPCA time series. While very useful these studies have left a number of important questions unanswered:

1. **What are the regime dynamics?**

   Monahan et al. (2001; 2003) considered the leading nonlinear mode obtained from 10-day low-pass filtered geopotential height data. Three regimes were obtained as in previous nonlinear analyses of Wallace (1996) and Smyth et al. (1999). The question remains as to what are the dynamics responsible for regime formation, maintenance and decay? Studies of atmospheric blocking suggest that synoptic eddy feedback is instrumental in the generation of large-

scale flow anomalies (e.g., Shutts 1983; Tsou and Smith 1990). Other studies suggest that Rossby wave propagation on longer time-scales may be important (e.g., Nakamura 1994; Nakamura et al. 1997). In this study we assess both the high- and low-frequency dynamics involved in regime formation, maintenance and decay.

2. **Can regimes be reproduced with a GCM?**

   Monahan et al. (2000c) considered the leading nonlinear mode from NH extended winters of monthly-mean SLP from a 1000-year control simulation of the Canadian Centre for Climate Modelling and Analysis (CCCma) first-generation coupled global climate model (CGCM1). However, to make a direct comparison with the observationally-based studies of Monahan et al. (2001; 2003), which use 41 winters of NH 10-day low-pass filtered data, it remains to apply NLPCA to 10-day low-pass filtered output from the GCM. In this study we obtain the leading nonlinear mode from GCM-simulated 10-day low-pass SLP. In this way the observed and model regimes can be compared directly.

3. **Will regimes change under global warming?**

   Monahan et al. (2000c) considered the leading nonlinear mode from monthly-mean SLP from a 500-year 4 $\times$ CO_2 stabilization simulation of the CCCma CGCM1. It was concluded that while the regime structures were essentially unchanged under global warming the time spent in the various regime states did. This is consistent with Palmer's (1999) hypothesis that climate change is reflected in changed regime occupancy. Here we address whether or not this simple picture changes when daily rather than monthly-mean data is used.

4. **Are regimes sensitive to time filtering?**

   The studies of Monahan et al. (2000c) and Monahan et al. (2001; 2003) are contradictory in that the former reports on two regimes, while the later reports on three. Are the differences due to the different smoothing applied to the data (monthly-mean vs. 10-day low-pass), the different variables used (e.g., SLP vs. Z_{500}) or are observed and GCM-simulated regimes intrinsically different? By obtaining the leading nonlinear mode using a range of temporal filter parameters we will address this question.

This dissertation is organized as follows. Chapter 2 describes the data sources, data pre-processing and NLPCA. Chapter 3 answers questions 1) and 2). Chapter 4 answers question 3), while Chapter 5 answers question 4). Conclusions are presented in Chapter 6.

Chapter 2

Data and Methodology

2.1 Data Sources

The observational dataset used in this study is the National Centers for Environmental Prediction (NCEP)/National Center for Atmospheric Research (NCAR) reanalyses (Kalnay et al. 1996). The reanalysis system uses a frozen global data assimilation system and a reasonably complete database (including rawinsonde, ship, aircraft, satellite and other data). The data assimilation model is a global spectral T62 model (with grid resolution of 1.9° latitude-longitude) with 28 vertical levels with the top level at about 3 hPa. These data are referred to throughout the thesis as "observations", when in fact they are a combination of observations and model data. The observational period used in this study is Jan. 1, 1958 to Dec. 31, 1999.

The model datasets used in this study are from the CCCma first generation coupled global climate model CGCM1 (Flato et al. 2000). The atmospheric component of CGCM1 is a global primitive equation spectral model with T32 triangular truncation (with grid resolution of 3.75° latitude-longitude) and 10 vertical levels with

the top level at about 12 hPa (McFarlane et al. 1992). The ocean component of CGCM1 is a global primitive equation grid point model with horizontal resolution of 1.875° longitude × 1.856° latitude and 29 vertical levels [based on the Geophysical Fluid Dynamics Laboratory (GFDL) Modular Ocean Model (MOM) 1.1 code described in Pacanowski et al. (1993)]. The atmosphere and ocean components exchange their daily averaged quantities once per day. One control and two stabilization simulations are available.

Control: A 100-year sample from a 1000-year simulation with equivalent CO_2 concentration fixed at 330 parts per million (ppm). The control climate, as described in Flato et al. (2000), generally reproduces the broad features of observed contemporary climate. Other 100-year samples will be used to assess statistical robustness of the NLPCA approximation.

Stabilization: Two 100-year samples from 1000-year simulations with the equivalent CO_2 and sulphate aerosol concentrations representative of year 2050 and 2100, based on IPCC IS92a scenario following Mitchell et al. (1995). These simulations follow a transient simulation from 1850 (Boer et al. 2000a; 2000b). The CO_2 concentrations are roughly equivalent to a tripling and a quadrupling over that used in the control simulation.

2.2 Data Preprocessing

The variables used in this study are twice-daily SLP, 500 hPa and 250 hPa geopotential height (Z_{500}, Z_{250}) and 250 hPa horizontal wind (u_{250}, v_{250}). The variables were averaged to once daily and placed onto a common 96 × 48 Gaussian grid (equivalent to about a 3.75° latitude-longitude horizontal resolution). Extended wintertime data

(Nov. 1 to Apr. 30) north of 20°N were used. Daily anomalies were computed relative to the daily climatological-mean annual cycle, and low-frequencies were isolated using a low-pass filter (Koopmans 1974) with a cut-off period of ten days. A Hanning taper (von Storch and Zwiers 1999) was employed to reduce variance leakage. The data dimensionality was reduced by using only the first ten linear EOFs (after equal area weighting) based on covariance matrix. In all cases the first ten EOFs explain over 60% of the total variance of the 10-day low-pass filtered data.

2.3 Nonlinear Principal Component Analysis

The theory of NLPCA is detailed in Monahan (2000a; 2000b). NLPCA attempts to extract a representative low-dimensional structure from a high-dimensional dataset. Take, for example, a typical geophysical field expressed as $X_i(t_n)$, where $i = 1, 2, \ldots, M$ is an index of spatial location and $n = 1, 2, \ldots, N$ denotes the time index. Since field values at different locations often evolve dependently it is possible to reduce the dimensionality of the data as follows:

$$\mathbf{X}(t_n) = f_E\{f_P[\mathbf{X}(t_n)]\} + \epsilon_n = \hat{\mathbf{X}}(t_n) + \epsilon_n, \tag{2.1}$$

where f_P is a projection function which maps $\mathbf{X}(t_n)$ from M to L dimensions ($L < M$), and f_E is an expansion function which maps back to the original M dimensions. The two functions f_P and f_E are determined by minimizing the mean squared difference between the approximation $\hat{\mathbf{X}}(t_n)$ and the original data $\mathbf{X}(t_n)$. In other words,

$$\epsilon^2 = \langle \|\mathbf{X} - \hat{\mathbf{X}}\|^2 \rangle \tag{2.2}$$

is minimized such that $\hat{\mathbf{X}}$ is the optimal approximation to the original data in the least squares sense. Here, $\|\cdots\|$ denotes the Euclidean norm and $\langle\cdots\rangle$ denotes the

sample average in time. Also, Eq. (2.1) represents classic PCA if the functions f_P and f_E are constrained to be linear.

A schematic representation of NLPCA is displayed in Figure 2.1. The top panel displays a scatter plot of arbitrary data showing a clear nonlinear structure in some abstract Cartesian space. This space could be, for example, the original grid point space or the phase space spanned by PCs. In NLPCA, the nonlinear projection function f_P maps the original data to a one dimensional time series $\lambda(t)$ (middle). The nonlinear expansion function f_E then maps the time series to an approximation curve $\hat{\mathbf{X}}(t)$ in the original data space (bottom). In this example, the approximation is seen as a U-shaped curve passing through the middle of the scatter of points. At any given time the position on the approximation curve can be obtained from the time series $\lambda(t)$. Specifically, $\lambda(t)$ measures the arc-length along the approximation curve, being zero at the left-most extreme and one at the right-most extreme. It is shown in Monahan (2000a) that NLPCA is a nonlinear generalization of linear PCA. The fundamental difference between NLPCA and PCA is that NLPCA allows for nonlinear projection and expansion functions while PCA only allows for linear functions. The leading PCA would, for example, inefficiently approximate the scatter in Figure 2.1.

The projection and expansion functions are obtained using an artificial neural network. Here, as in Kramer (1991), we use the five-layer feed-forward neural network shown in Figure 2.2. The first and last layers are the input and output layers, each containing L processing elements, or neurons. The second and fourth layers are encoding and decoding layers each containing H neurons. The third layer is a bottleneck layer containing P neurons. The output of each neuron in the ith layer is used as input to the $(i+1)$th layer. If $x_j^{(i)}$ is the output of jth neuron in the ith

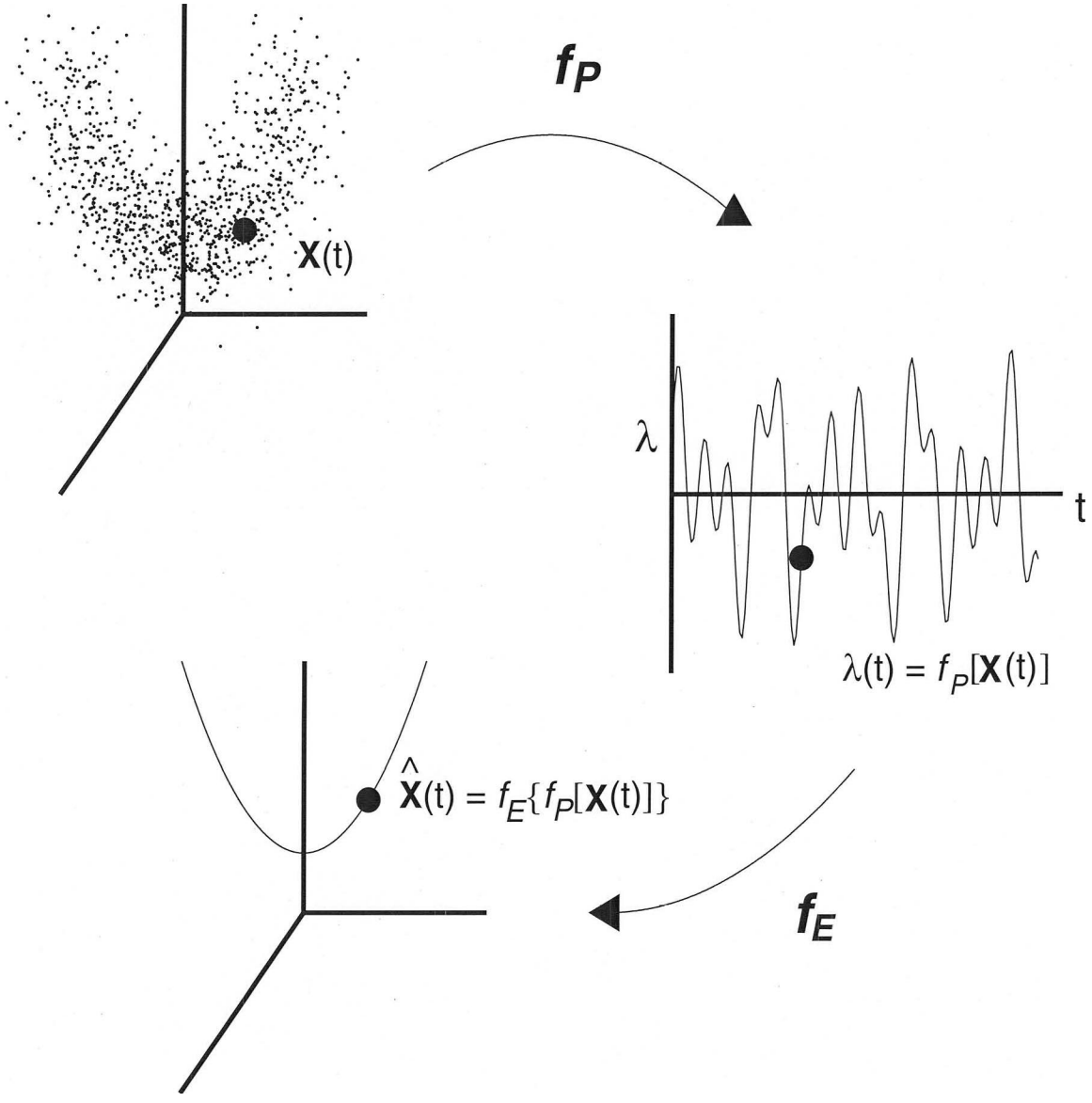

Figure 2.1: Schematic representation of NLPCA. Top: Scatter of data $\mathbf{X}(t)$ in some abstract Cartesian space (see text); Middle: Nonlinear time series $\lambda(t)$; Bottom: NLPCA approximation $\hat{\mathbf{X}}(t)$. The large black dot in each panel denotes an arbitrary data point. f_P and f_E represent the projection and expansion functions, respectively. Adapted from Monahan et al. (2003).

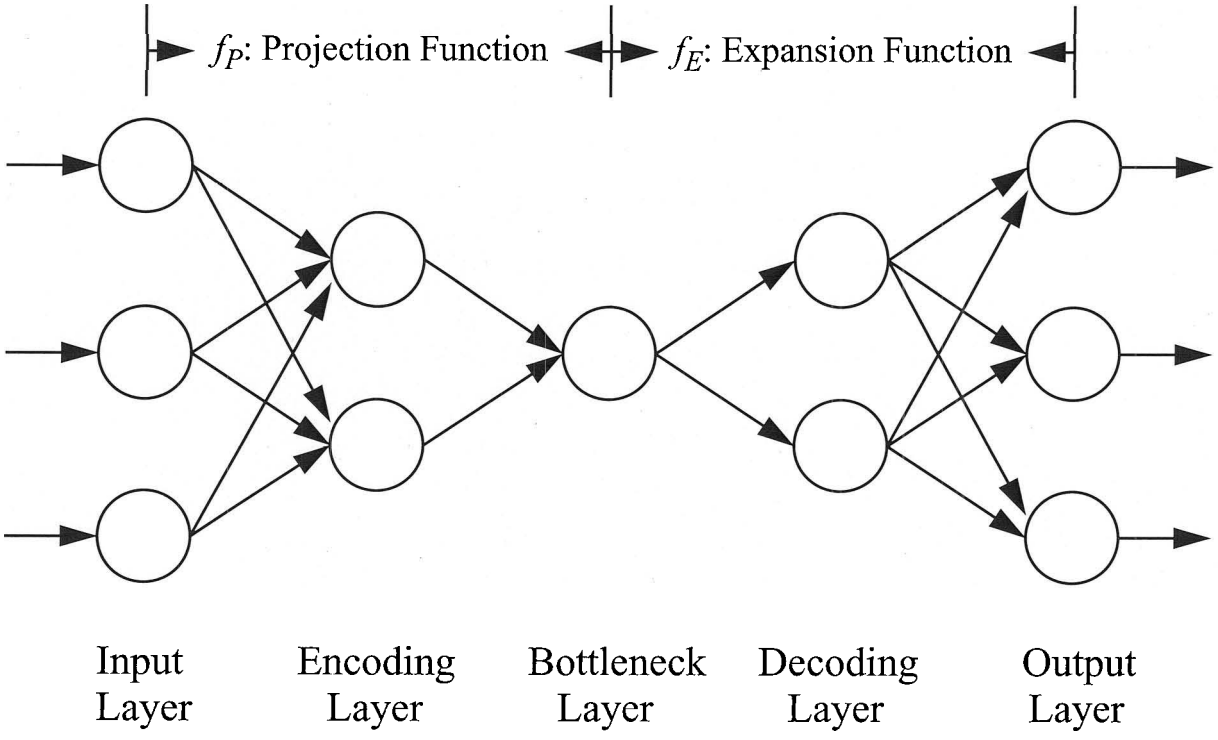

Figure 2.2: Five-layer feed-forward neural network used to implement NLPCA.

layer, then the output of the kth neuron in the $(i+1)$th layer $x_k^{(i+1)}$ is

$$x_k^{(i+1)} = f^{(i+1)}[\sum_{j=1}^{N_i} w_{jk}^{(i+1)} x_j^{(i)} + b_k^{(i+1)}], \tag{2.3}$$

where $f^{(i+1)}$ is the $(i+1)$th layer transfer function and N_i is the number of neurons in the ith layer. In this implementation the transfer functions are hyperbolic tangent functions. The weights (w) and biases (b) are adjusted using a conjugate gradient algorithm (Press et al. 1992) which minimizes the mean squared difference between the input and output layers. Here we set $H = 2$ and $P = 1$.

As shown in Figure 2.2 the first three layers generate the projection function while the last three layers produce the expansion function. The minimization procedure leading to estimates of f_P and f_E is carried out iteratively given initial guesses for the weights and biases. This process is referred to as "network training", which in practice is subject to constraints such as reproducibility and smoothness of the approximation. Furthermore, an early stopping technique (Finnoff et al. 1993) is employed to avoid over-fitting, i.e., to ensure the robustness of the model to introduction of new data. This is done by training on a randomly selected fraction of the data, and then validating on the remainder. When the errors and/or the number of iterations exceed preset thresholds the procedure is stopped. In this implementation 20% of the data are used for validation and the procedure is stopped when fractional errors exceed 2% or when the number of iterations exceed 20000, whichever comes first. The results shown in this thesis are not sensitive to reasonable changes in any of these quantities.

There is no guarantee that the minimum obtained as above is global (Hsieh and Tang 1998). For this reason an ensemble of at least twenty training runs is carried out with randomly selected initial weights and biases to ensure the robustness of

the model to changes in initial values of the statistical parameters. Those runs with errors in the validation set which exceed those in the training set are discarded. From the remaining members the run with the smallest mean squared error is taken as the ultimate solution. Finally, we mention that in order to reduce the data dimensionality inputs to the neural network are given by the first ten linear PCs. This greatly reduces the amount of computation and the number of statistical parameters to be estimated.

Chapter 3

Nonlinear Variability in the Recent Past

Here we compare the leading nonlinear variability modes derived from the NCEP observations and the CGCM1 control simulation. We remind the reader that the NCEP observations are for the 1958-1999 period, while the CGCM1 control simulation is a 100-year segment of a long control run with fixed equivalent CO_2 forcing. Section 3.1 compares some basic statistics, while Section 3.2 compares the leading nonlinear modes themselves. Section 3.3 summarizes the results.

3.1 Basic Statistics

Figure 3.1 shows winter-means for the observations (top), the control simulation (middle) and their difference (bottom). Mean SLP shows three major centers known as the Aleutian low, the Icelandic low and the Siberian high. The model reproduces these centers, however each is slightly eastward-shifted and overestimated (i.e., the

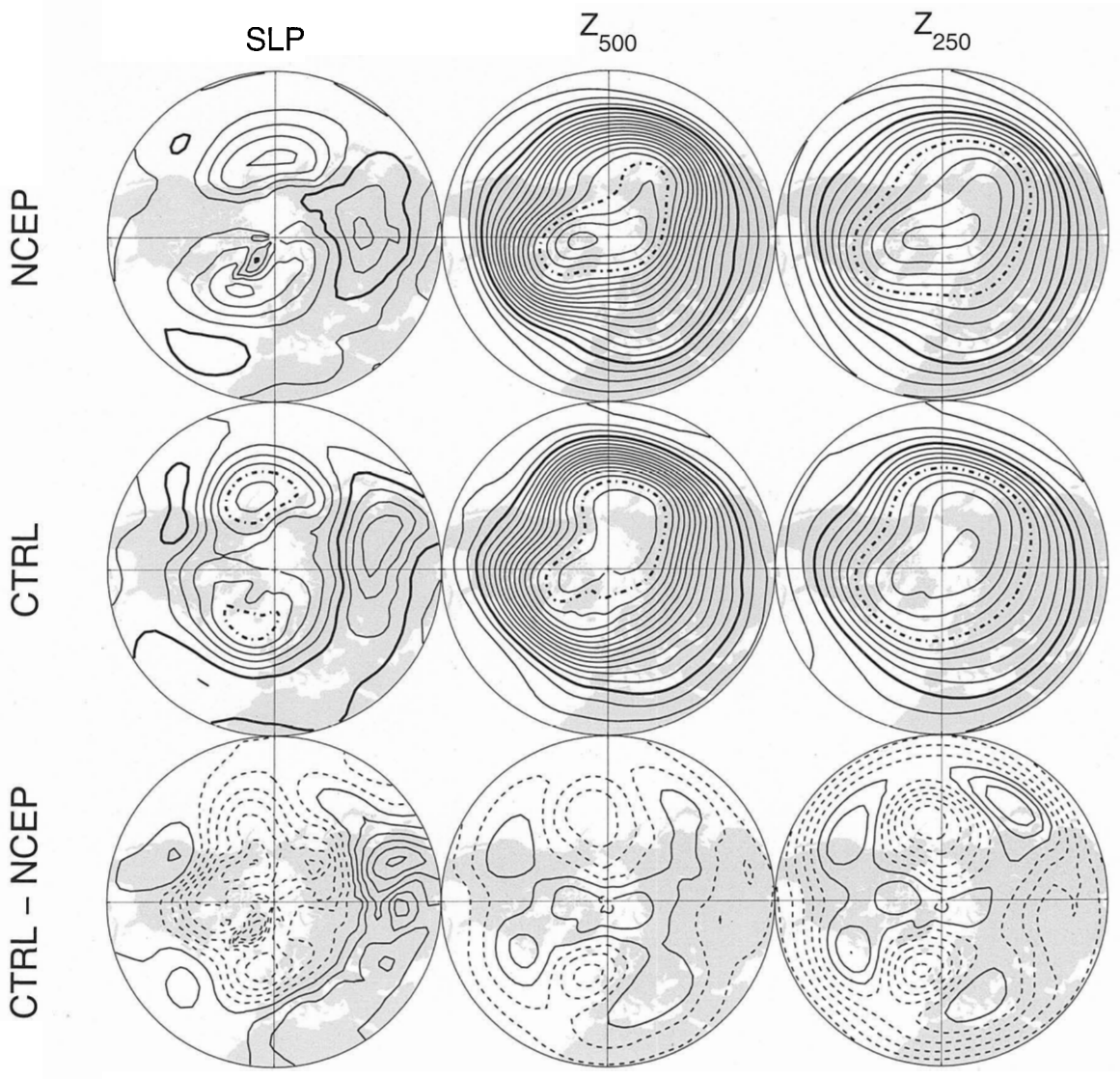

Figure 3.1: Winter-mean SLP (left), Z_{500} (middle) and Z_{250} (right) as observed, simulated and their difference. Contour intervals are 4 hPa (SLP), 40 m (Z_{500}) and 100 m (Z_{250}), respectively, with 1000 (1020) hPa for SLP, 5200 (5680) m for $\boldsymbol{Z_{500}}$ and 10000 (10500) m for Z_{250} in bold dash-dot (bold solid). For the differences, the contour intervals are 2 hPa, (..., -3, -1, 1, ...) for SLP and 30 m (..., -45, -15, 15, ...) for $\boldsymbol{Z_{500}}$ and Z_{250}. Positive (negative) contours are solid (dashed). Here, and in subsequent spatial maps, the fields have been slightly smoothed with a 5-point Shapiro (1970) filter.

simulated lows are too low and simulated highs are too high). Mean Z_{500} and Z_{250} show major troughs over the east coasts of Asia and North America and major ridges over the eastern Pacific and eastern Atlantic. In addition, a minor trough exists over western Europe. The model reproduces the major troughs and ridges, but the minor trough over western Europe is less clear. We also note that the simulated troughs are too high and that the simulated ridges are too low. There is also an eastward bias in the position of the ridge and trough lines.

Figure 3.2 shows the winter SLP variance for the observations (top), control simulation (middle) and their difference (bottom). Shown are results given unfiltered (left), 10-day low-pass filtered (middle) and 10-day high-pass filtered (right: calculated as a residual) data. The unfiltered data shows two maxima corresponding to the positions of the Aleutian and Icelandic lows. The model reproduces these maxima however they are shifted eastward and underestimated. The difference field shows that the model overestimates variability over Canada and underestimates variability over the North Atlantic and North Pacific. Figure 3.3 is as in Figure 3.2 except for Z_{500}. In both the observations and the model the total variability is dominated by low frequencies as in SLP. The high-frequency variance highlights the midlatitude storm tracks. The model reproduces the storm tracks reasonably well, however the Pacific storm track is displaced somewhat eastward and there is too little synoptic variability in the Greenland and Norwegian seas (probably owing to the climatological flow being too zonal over the North Atlantic, cf. Figure 3.1).

Figure 3.4 compares the leading observed (top) and simulated (bottom) EOFs of 10-day low-pass filtered SLP. The observations and model agree well in this regard. The leading EOF is associated with the AO, with one center of action over high latitudes and two others with opposite polarity over the North Pacific and Atlantic

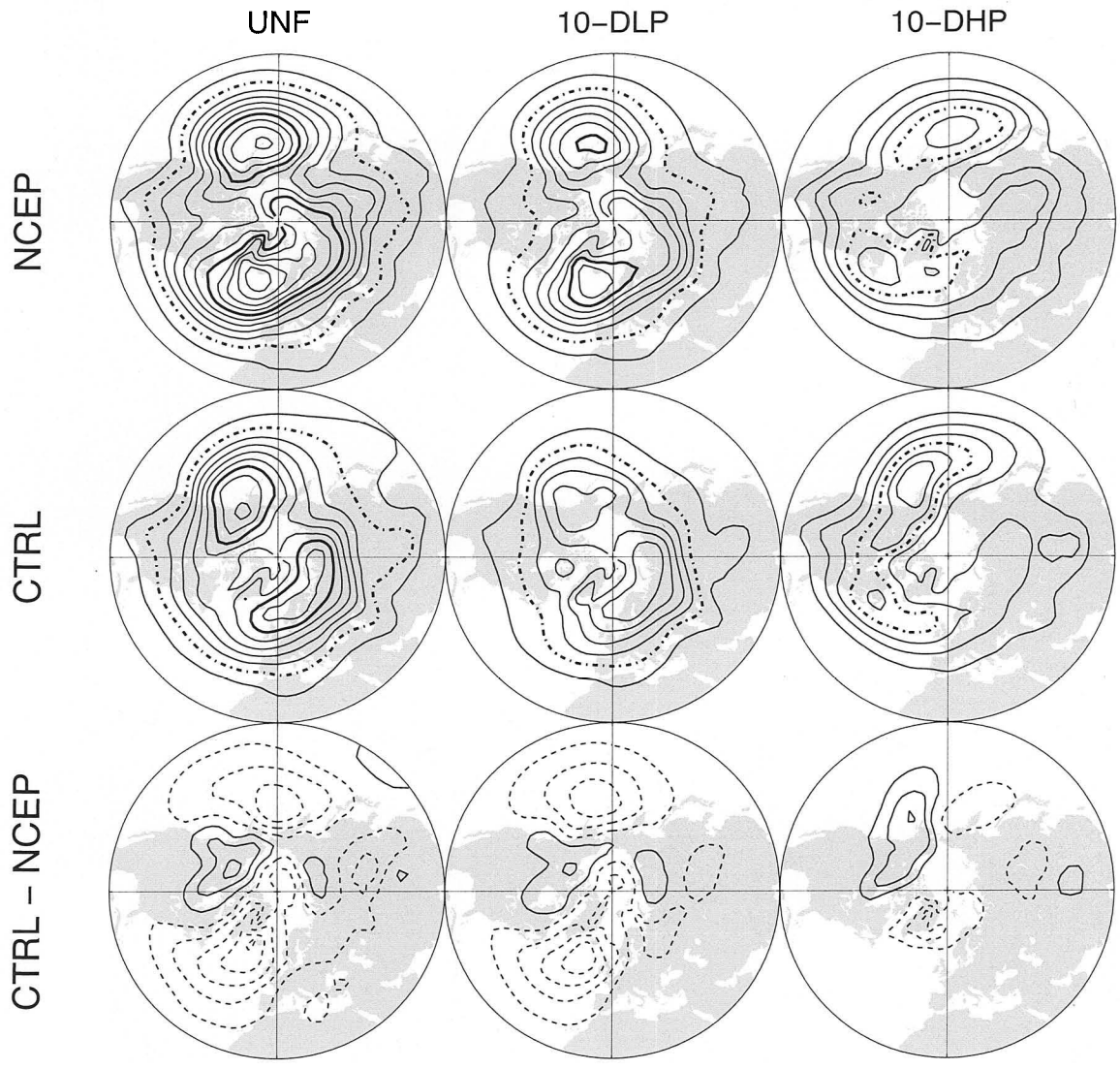

Figure 3.2: Day-to-day variance for winter SLP as observed, simulated and their difference. Contour interval for the top two panels are 20 hPa^2, with 40 (140) hPa^2 in bold dash-dot (bold solid). Contour interval for the difference (bottom panels) is also 20 hPa^2 (..., -30, -10, 10, ...), with positive (negative) contours solid (dashed). The contour intervals for 10-day high-pass (10-DHP) maps are half that of the unfiltered (UNF) and 10-day low-pass (10-DLP) maps.

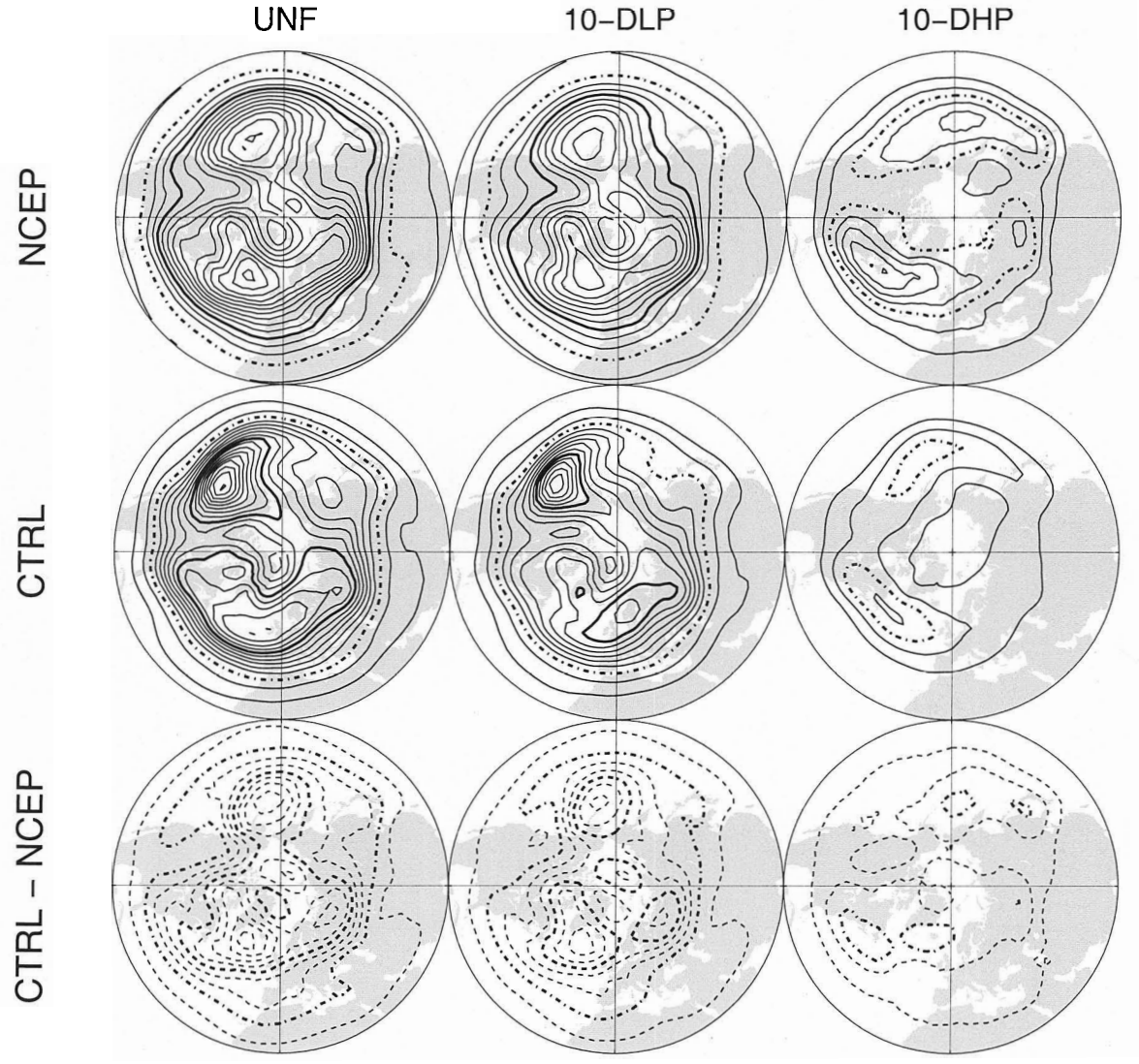

Figure 3.3: As in Figure 3.2 but for Z_{500}. Contour intervals are 2000 (1000) m^2 for UNF and 10-DLP (10-DHP) from NCEP and 1000 m^2 for CTRL, with 3000 (9000) m^2 in bold dash-dot (bold solid). Contour intervals for the difference are 2000 m^2 (..., -3000, -1000, 1000, ..., for UNF and 10-DLP), with -3000 (-9000) m^2 in bold dash-dot (bold dash), and 1000 m^2 (..., -1500, -500, 500, ... for 10-DHP) with -2500 m^2 in bold dash-dot.

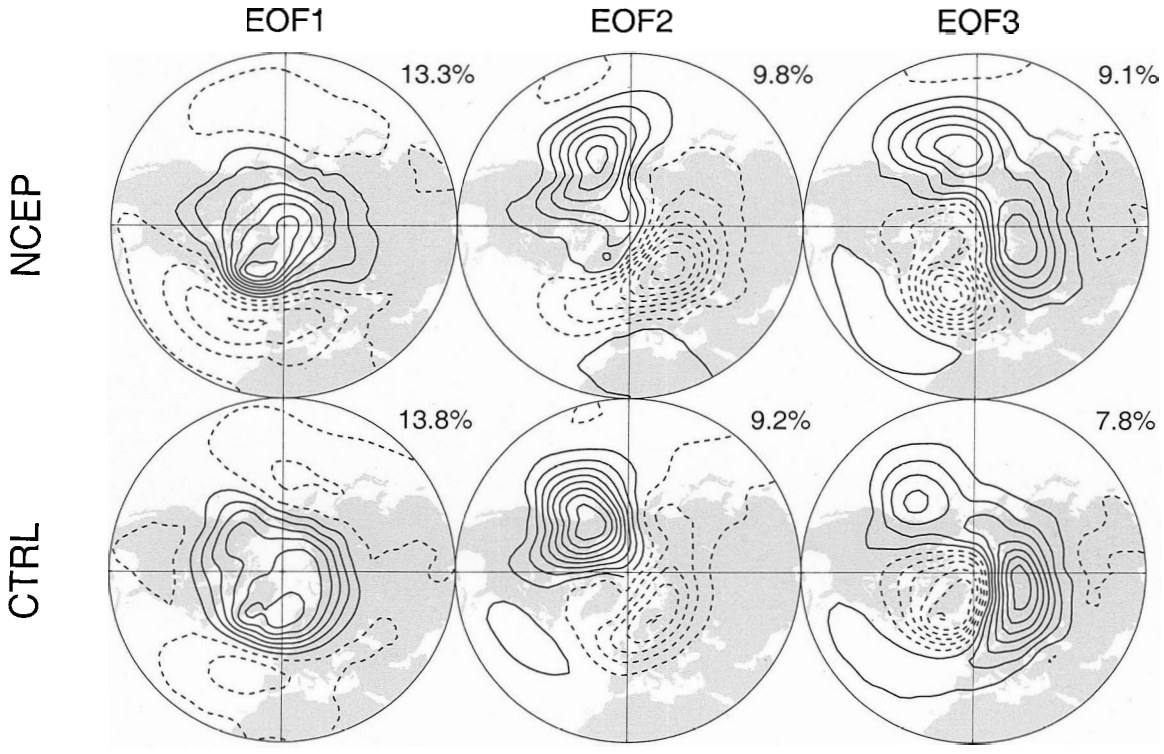

Figure 3.4: Leading EOFs for 10-day low-pass filtered SLP. Contour interval is 0.5 (..., -0.75, -0.25, 0.25, ...), with positive (negative) contours in solid (dashed). The number in the upper right corner of each panel indicates the percentage of the total variance explained by each PC.

(cf. Figure 1.1). As discussed in Monahan et al. (2001) the leading linear modes of 10-day low-pass filtered data are statistically dependent despite being uncorrelated by construction. In fact, two uncorrelated variables do not imply that they are independent although the converse is true. A simple example of this is given by the random variables x and $y = x^2$. For the random variables x and y, although they are uncorrelated they are clearly not independent. Figure 3.5 shows the difference between the observed joint linear PC_1 and PC_2 distribution and the product of their individual distributions. Non-zero values of this quantity are indicative of statistical dependence. The leading linear modes are statistically dependent and hence cannot be considered as fundamental modes of variability (although the values in Figure 3.5 are small). This is one of the motivations for the present application of NLPCA, which we turn to now.

3.2 Leading Nonlinear Modes

We now derive the leading nonlinear modes of observed and simulated 10-day low-pass filtered SLP. In order, we describe the spatial structure, temporal evolution and underlying dynamics.

3.2.1 Spatial Structure

Figure 3.6 shows the observed leading nonlinear mode (explaining about 14.8% of the total variance). The leading nonlinear mode has a U-shaped approximation in linear PC_1 and PC_2 space (upper left) and a time-series which is clearly tri-modal (upper right). In fact, the NLPC approximation curve is embedded in a ten-dimensional space. Here only two dimensions are retained since the approximation projects

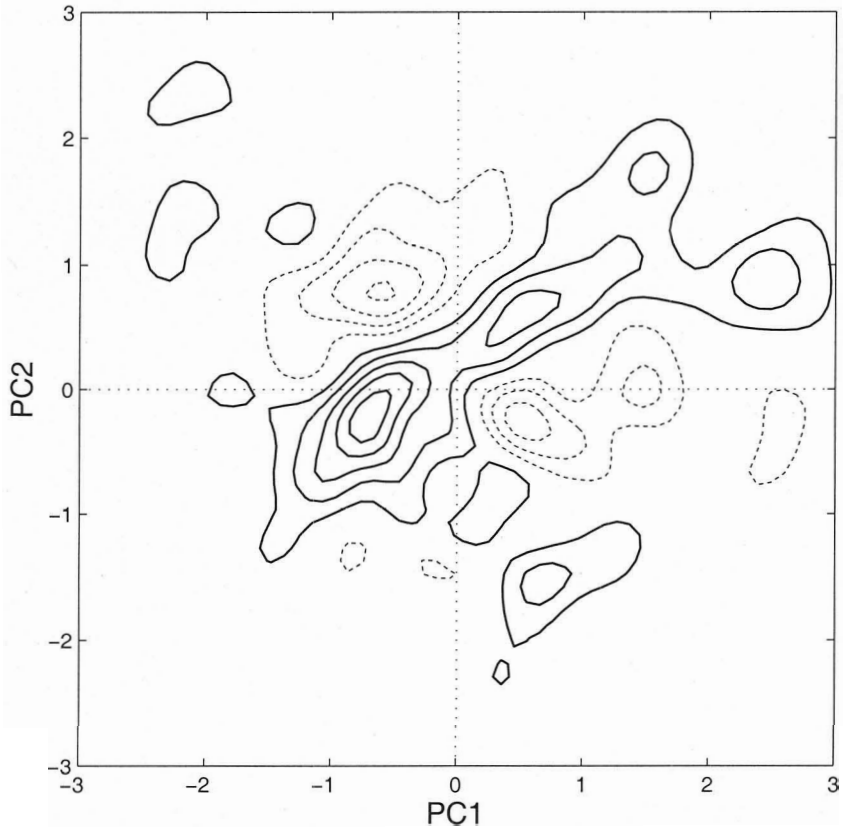

Figure 3.5: Observed difference PDF, i.e., PDF(PC_1, PC_2) - PDF(PC_1)PDF(PC_2). The PDFs are estimated using a Gaussian kernel estimator with a window width h = 0.2. Contour interval is (..., -5.0, -2.5, 2.5, ...) $\times 10^{-5}$. PC_1 and PC_2 are the leading linear principal component time series.

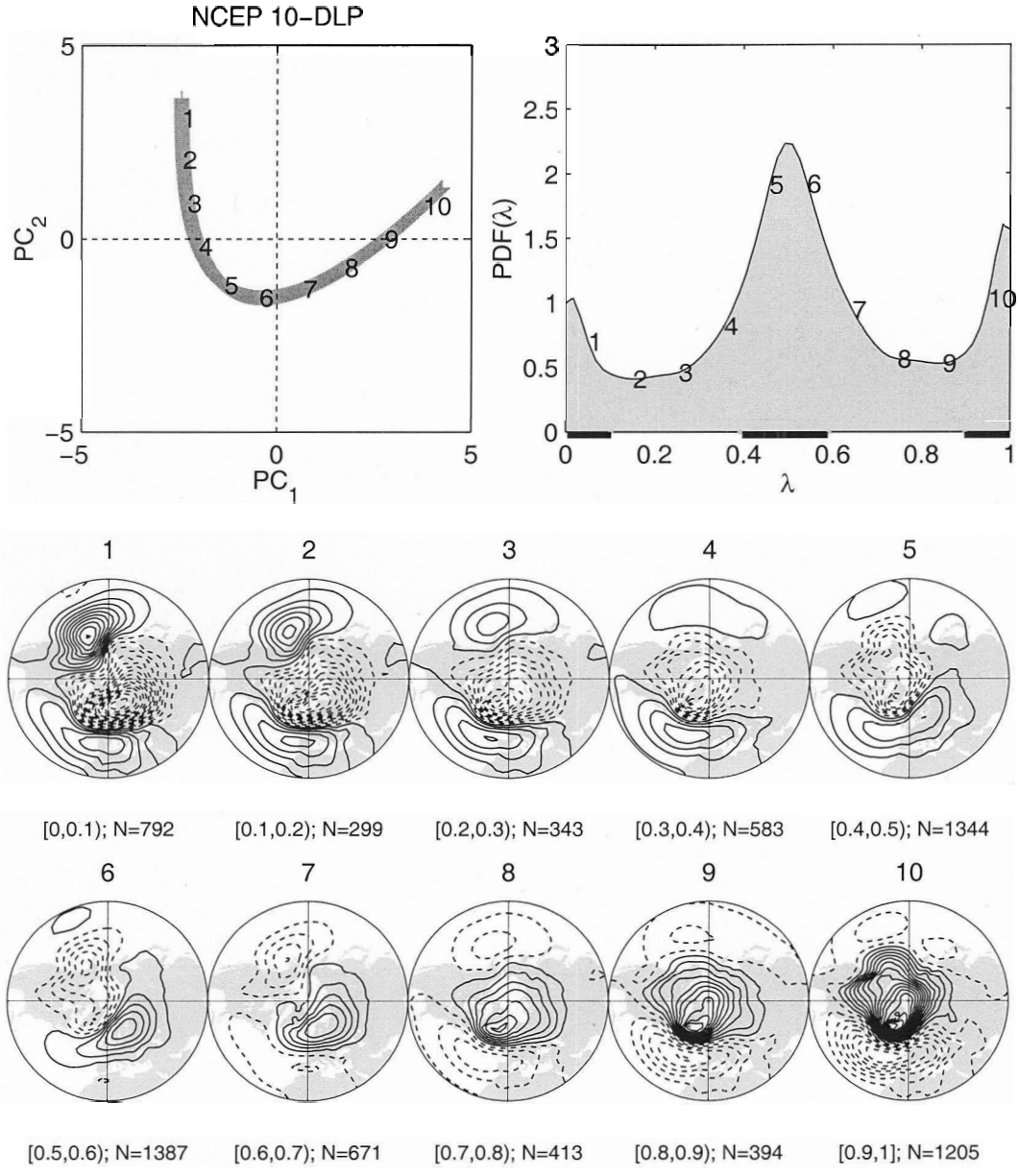

Figure 3.6: Upper left: Observed leading NLPCA approximation for 10-day low-pass filtered SLP in the space of the leading linear PCs; Upper right: PDF of the NLPCA time series $\lambda(t)$. The numbers on the curve indicate the $\lambda(t)$ locations corresponding to the maps. The bars on the $\lambda(t)$ axis define R_1, R_2 and R_3 regime boundaries, namely, [0.0,0.1], [max(pdf($\lambda(t)$)) $\pm$ 0.1] and [0.9, 1.0]. Lower: Approximation maps with contour interval: 1.0 hPa (..., -1.5, -0.5, 0.5, ...). Positive (negative) contours are in solid (dashed). The maps are averaged over the indicated $\lambda(t)$ interval. The number of maps comprising a given average is given by N.

strongly on the first two linear PCs and weakly on the higher ones. Representative spatial maps (constructed from the leading ten linear modes) along the approximation are also shown. In addition, a plot of the NLPCA time series $\lambda(t)$ for each observed winter is displayed in Figure 3.7. The time series $\lambda(t)$ shows recurrence and/or persistence in the three shaded regions associated with the three regimes, thus giving the three distinct PDF peaks of $\lambda(t)$ shown in Figure 3.6. Besides, it is also clearly evident that $\lambda(t)$ shows considerable interannual variability in the time spent in a given regime. By examining the annual occupation frequency of each regime for each observed winter, Monahan et al. (2003, their Figure 7) show that the interannual variability is partly influenced by ENSO events. This influence is also apparent in Figure 3.7. For example, during El Niño winters (e.g., 1987, 1988), regime R_2 is favored over regime R_1, whereas during La Niña winters (e.g., 1989), regime R_1 is favored over regime R_2. Figure 3.8 shows the simulated leading nonlinear mode (explaining about 15.0% of the total variance). It is remarkable how realistic the simulated mode is. Figure 3.9 directly compares the leading nonlinear modes. The regime spatial structures shown here are defined as the spatial maps corresponding to neighborhoods of the λ distribution peaks. We note the strong agreement between the observed and simulated regimes maps.

We now characterize the regime maps, and their stability. Regime R_1 has positive anomalies centered over the Aleutians and the northeast Atlantic and negative anomalies centered over Scandinavia. Regime R_2 has negative anomalies extending from the Northeast Pacific to Greenland and positive anomalies extending across the North Atlantic and Siberia. Regime R_3 consists of a meridional dipole over the North Atlantic which is very similar to the negative phase of the AO (cf. Figure 1.1). Figure 3.10 shows the corresponding Z_{500} regime maps. Here we see that the observed

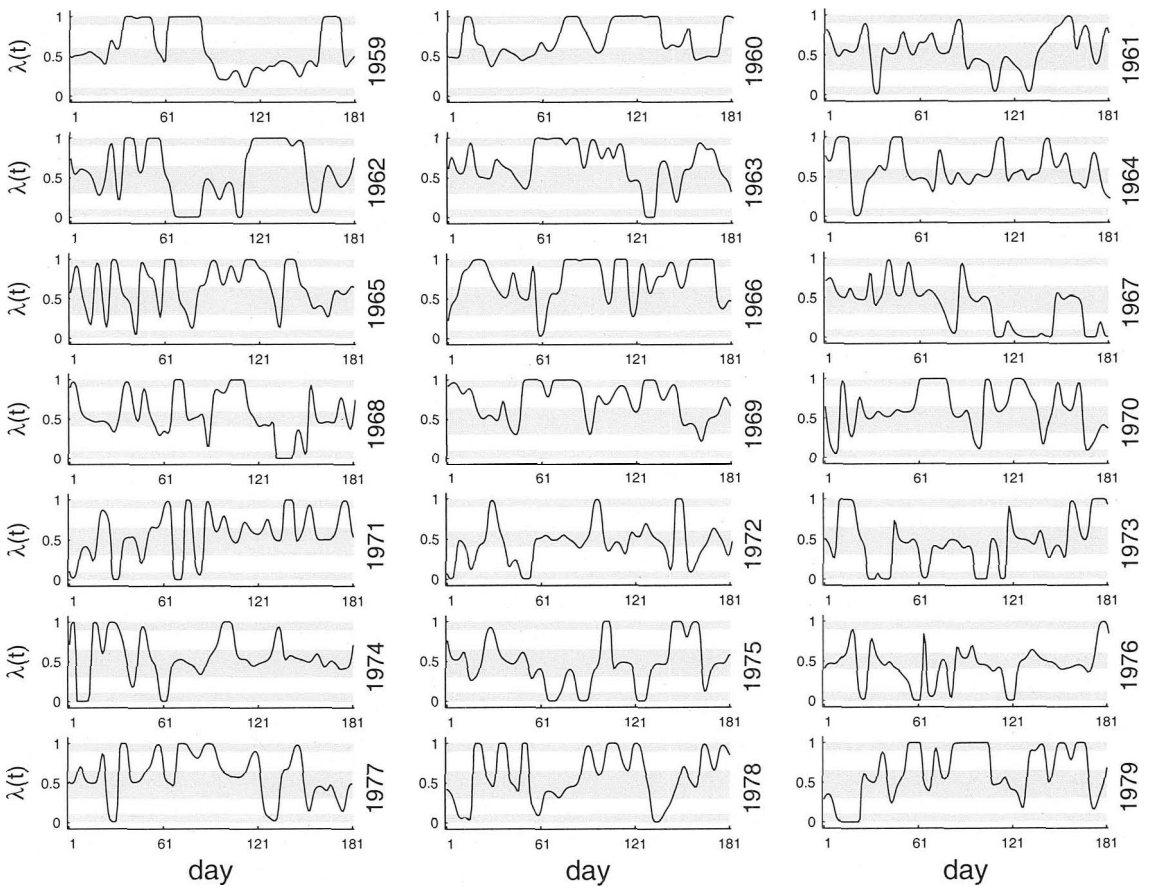

Figure 3.7: Distribution of the NLPCA time series $\lambda(t)$ for each of the extended winters (Nov. 1 to Apr. 30) from observations. The shaded regions represent the $\lambda(t)$ intervals associated with the three regimes as shown in Figure 3.6. The date on the right-hand-side of each panel indicates the year of January of the corresponding winter.

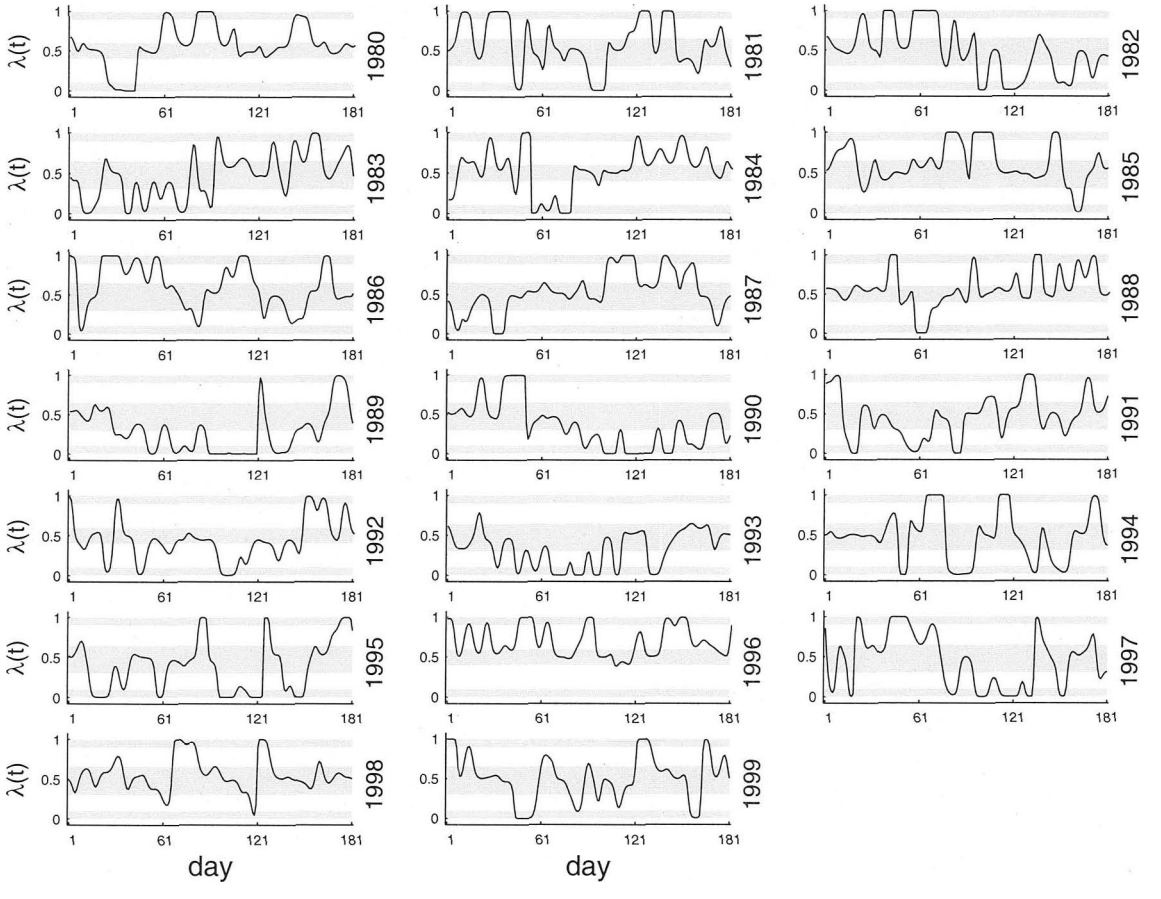

Figure 3.7: Continued.

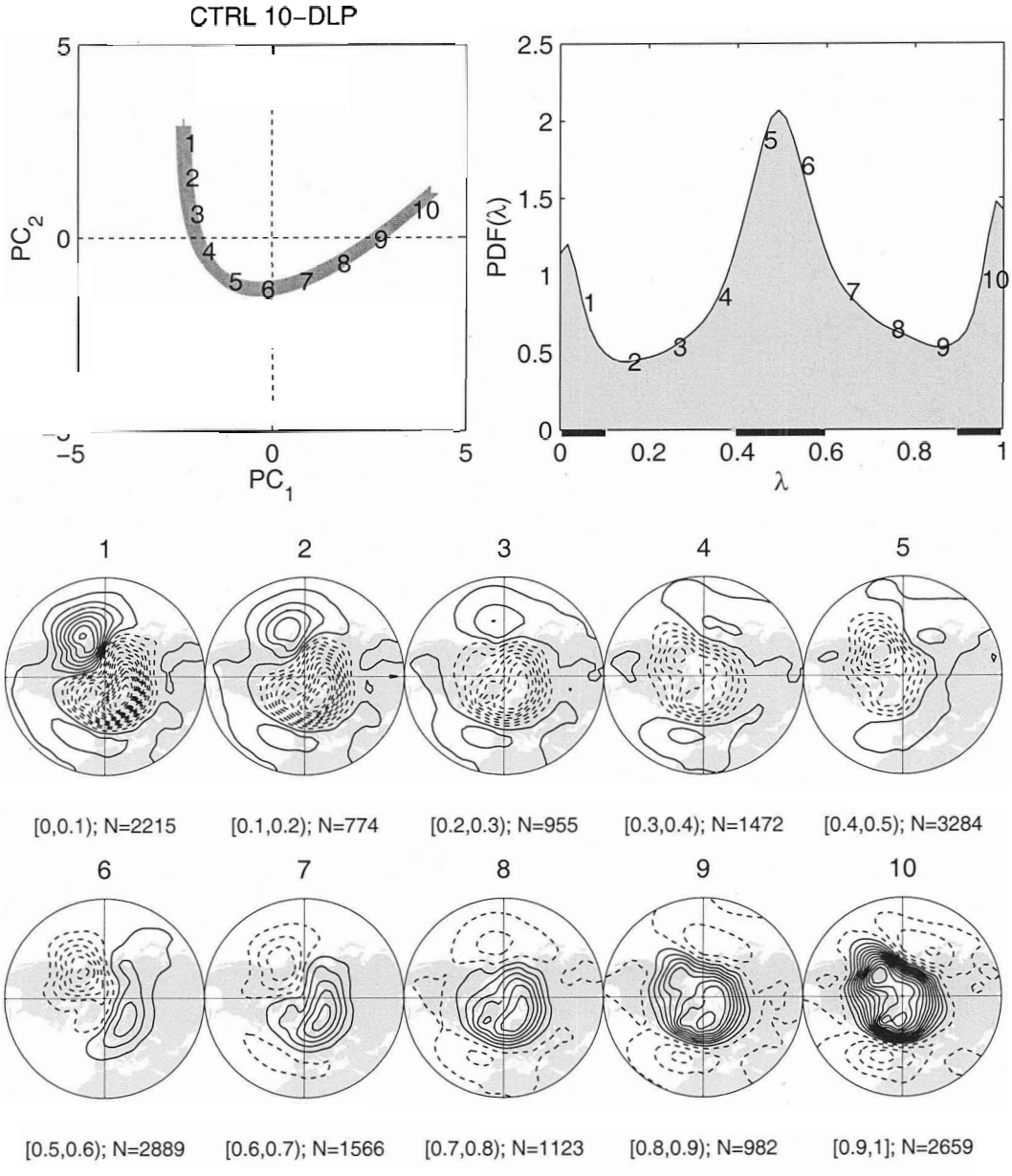

Figure 3.8: As in Figure 3.6, but for the control simulation.

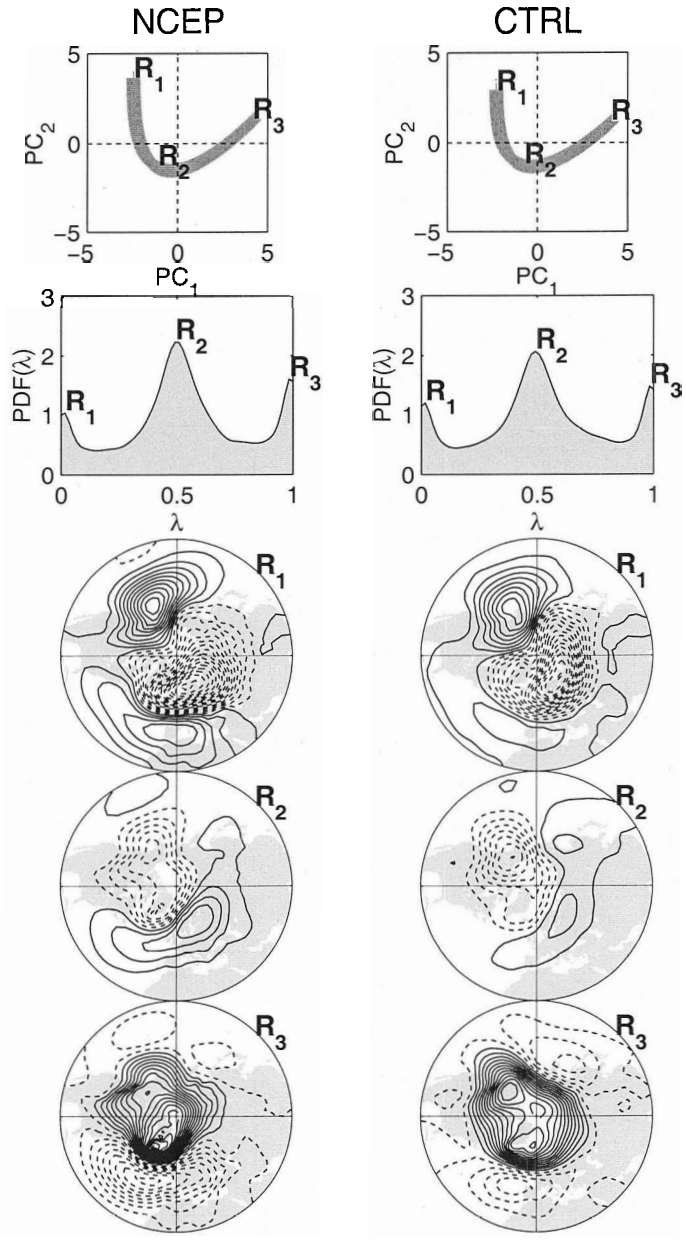

Figure 3.9: Leading nonlinear modes with representative regime maps. Observed (left) and simulated (right). Contour interval: 1.0 hPa (..., -1.5, -0.5, 0.5, ...). Positive (negative) contours are solid (dashed).

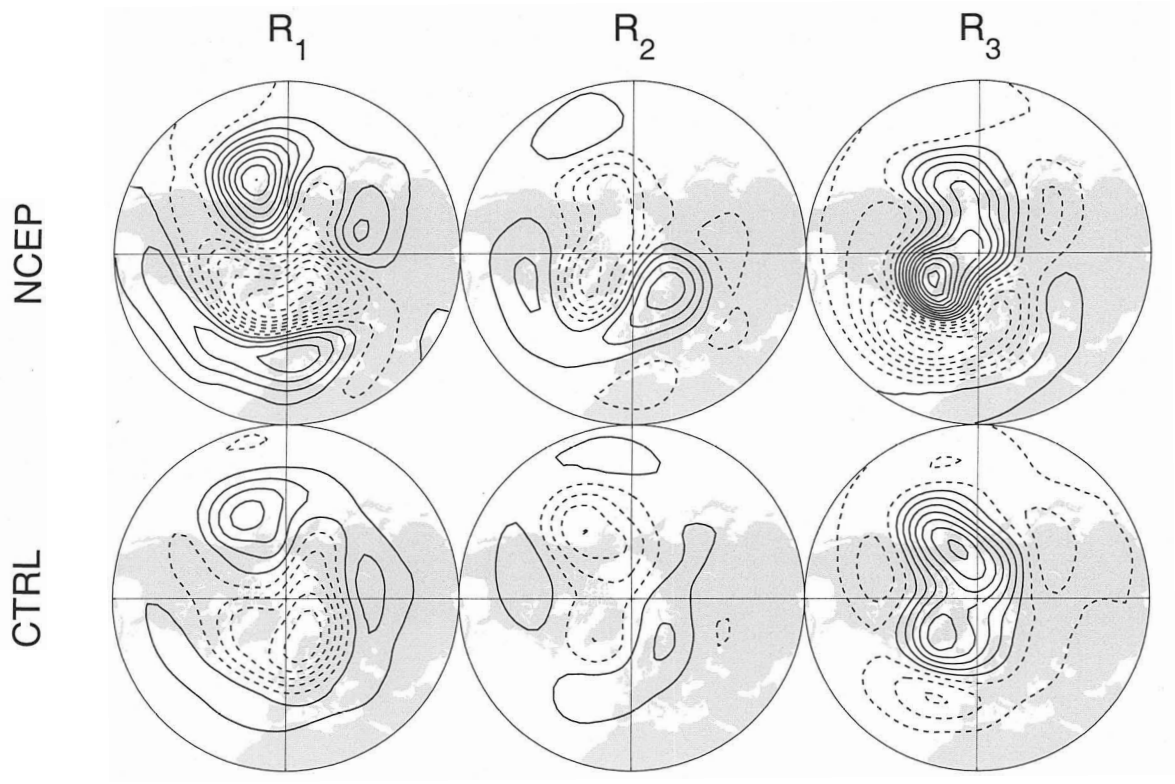

Figure 3.10: Regime maps for Z_{500} with contour interval: 20 m (..., -30, -10, 10, ...). Positive (negative) contours are solid (dashed).

NLPCA-based regime maps are similar to those obtained by other nonlinear studies (see Figure 1.2). We also note how well the observed and simulated Z_{500} regime maps agree with one another. To test the stability of the leading simulated nonlinear mode we have repeated the NLPCA for a different 100-year sample from the 1000-year control simulation. Comparing Figure 3.9 (right) and Figure 3.11 shows that the leading nonlinear modes from the two independent samples are very similar. We have also been able to verify that the removal of all linear temporal trends before NLPCA produces observed regimes structures (not shown) which are indistinguishable from those shown here. We now ask how long a data record is required to obtain robust regime structures? While the observed record is limited we can exploit the long model runs to indirectly address this question. By examining the 10-dlp filtered model output with the length of sample varying from 10 years to 100 years, with a 10-year increment, it is estimated that five or more decades of 10-dlp filtered model output is required to properly resolve these underlying nonlinear structures.

3.2.2 Temporal Evolution

Unlike other nonlinear techniques NLPCA produces a timeseries which allows the temporal evolution of the leading mode to be straightforwardly characterized. We begin by defining the presence in a given regime state as the period during which $\lambda(t)$ lies in a given interval (see the caption in Figure 3.6). On this basis, a "regime event" is defined as an uninterrupted period during which the system remains within a given regime state. Further, we follow Mo and Ghil (1988) and Kimoto and Ghil (1993b) and define long and short regime events as those regime events that are longer and shorter than five days, respectively. A timescale of five days provides a natural separation between synoptic and low-frequency variability. For a given

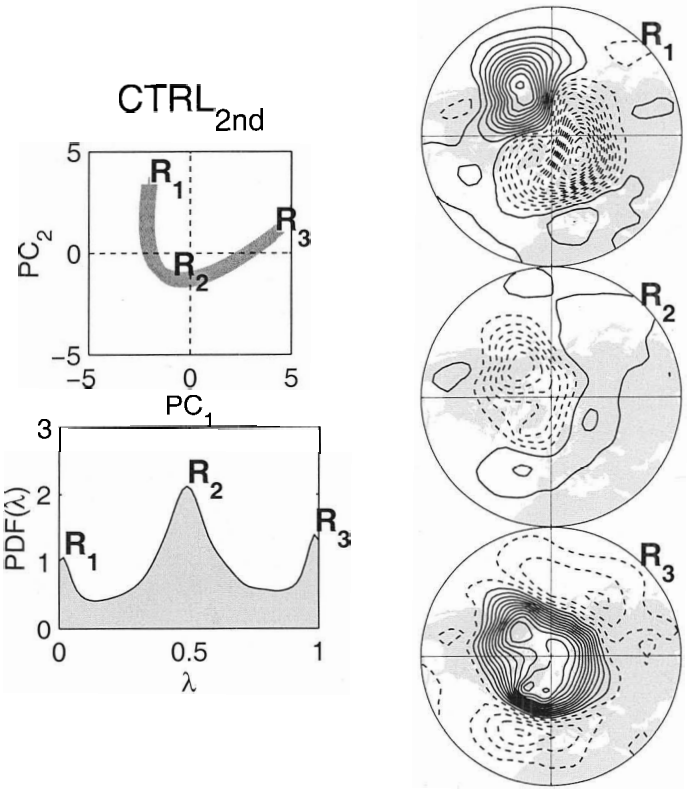

Figure 3.11: Simulated leading nonlinear mode from a different 100-year sample of the 1000-year control simulation.

regime interval, Table 3.1 shows the percent and average time spent in each regime. Whether observed or simulated we note that: 1) just over 60% of the time is spent in a regime state, with long events constituting the vast majority of that time; 2) The average time spent in a regime state is about 7 days taking all events together, and about 10 days taking just the long events. Figure 3.12 shows the observed regime patterns associated with all (top), long (middle) and short (bottom) events. (The corresponding simulated maps are very similar.) It is clear that the long events describe the regimes much more than do the short events. Hence the long events are the focus of the subsequent composite analysis.

Towards characterizing the evolution into- and out-of long regime events we define "day 0 for onset" as the day entering a given long event, and "day 0 for break" as the day leaving the same long event. Our objective here is to produce a composite evolution into- and out-of each of the three regimes. Our first step is to determine how many days before "day 0 for onset" (and after "day 0 for break") statistically significant composites exist. We begin by noting that for each "day 0 for onset" event there is a unique point in the space of the first ten linear PCs . We define the mean "day t for onset" distance in this space as the average distance between each "day t for onset" point and the average "day t for onset" point ($t = \ldots, -1, 0, +1, \ldots$). The mean distance is then averaged over all three regimes and produces the thick solid curves in Figure 3.13. The dashed curves correspond to break. The shading indicates the 95% confidence interval for the climatological mean distance for all points in phase space. From this calculation we conclude that composite spatial maps a few days before "onset day 0" and a few days after "break day 0" are statistically significant (i.e., since the curves fall outside the shading). Furthermore, during onset (break), the mean distance decreases (increases) as points converge (diverge) in state space.

Table 3.1: Regime statistics.

	Regime	Percent time spent	Average time spent (days)
		All (Long)	All (Long)
NCEP	R_1	10.7 (9.3)	7.1 (9.1)
	R_2	36.6 (30.6)	6.4 (10.5)
	R_3	16.2 (13.7)	6.9 (9.6)
CTRL	R_1	12.4 (10.8)	7.3 (9.6)
	R_2	34.5 (29.4)	6.7 (10.2)
	R_3	14.8 (13.1)	7.9 (10.1)

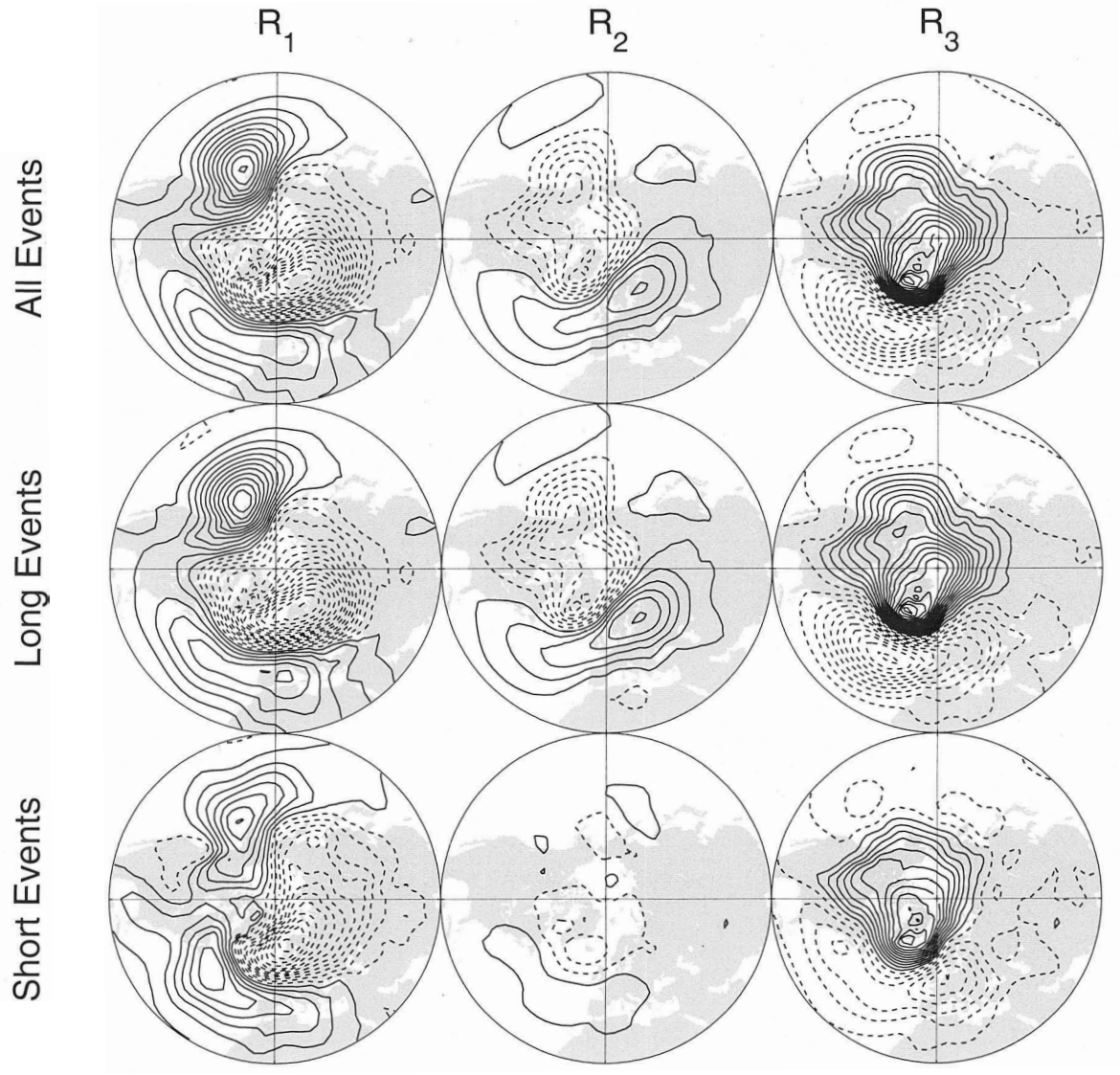

Figure 3.12: Observed regime maps given all (top), long (middle) and short (bottom) events. **Contour interval: 1.0 hPa** (..., **-1.5, -0.5, 0.5,** ...). **Positive (negative)** contours are solid (dashed).

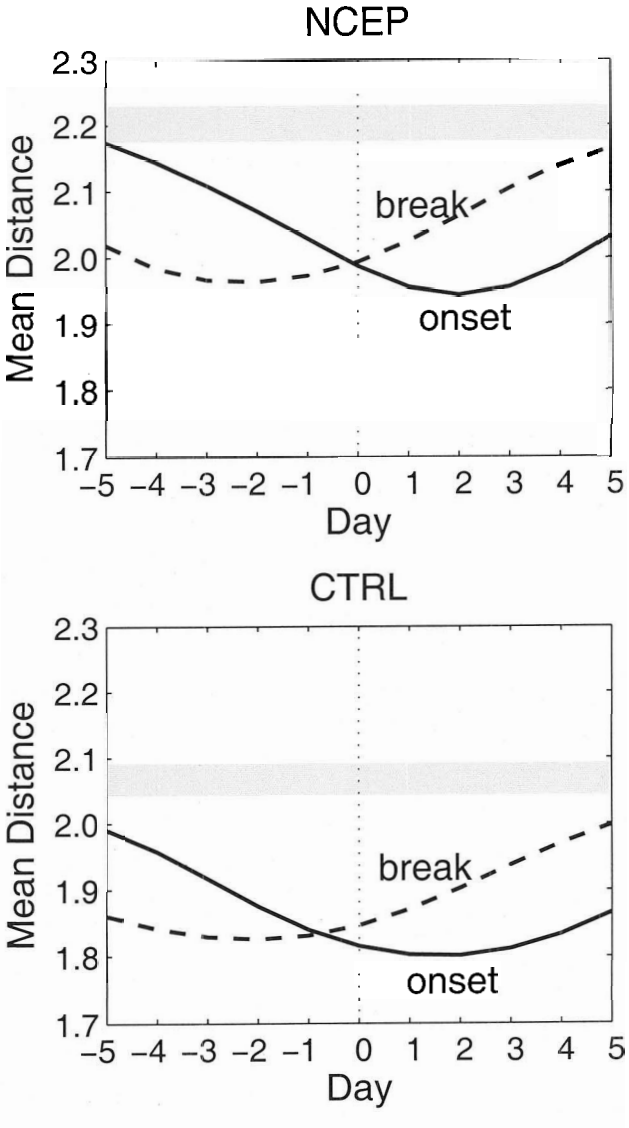

Figure 3.13: Mean distance for a given onset (solid) and break (dashed) day. See the text for details.

Figure 3.14 shows composite onset and break maps for regime R_1. Onset day -4 has negative anomalies over high latitudes and positive anomalies over the Northwest Pacific and Europe. As onset day 0 approaches the positive center over the Northwest Pacific migrates eastward and amplifies, while the positive center over southern Europe tends to shift westward over the North Atlantic. At the same time the negative anomalies at high latitudes amplify and shift their center of action to Northern Scandinavia. In this way regime R_1 is established. This North Pacific onset is reminiscent of the evolution of persistent anomalies found in Dole (1983). During break the positive anomalies in the North Pacific rapidly decay after day 0 and are eventually replaced by negative anomalies. The model does a good job at reproducing onset and break evolution for regime R_1.

Figure 3.15 shows composite onset and break maps for regime R_2. Onset day -4 has negative anomalies over the Central North Pacific and Europe and positive anomalies over North America and the Arctic. As onset proceeds the negative anomalies over the Central North Pacific migrate eastward and amplify and eventually cover all of North America and the Arctic. At the same time, the negative anomalies over Europe are replaced by positive anomalies ranging from the North Atlantic through Northern Eurasia. During break the negative anomalies over North America and the Arctic stretch-out meridionally and split, leaving positive anomalies over the region. The model does a good job at reproducing onset and break evolution for regime R_2.

Figure 3.16 shows the composite onset and break maps for regime R_3. Onset day -4 has positive anomalies over Western Europe and negative anomalies to the south. By onset day -2 the positive center over Scandinavia has retrograded to the southern tip of Greenland. At this time we note the development of positive anomalies over the Northeastern Pacific. By onset day 0 a strong dipole is established over the North

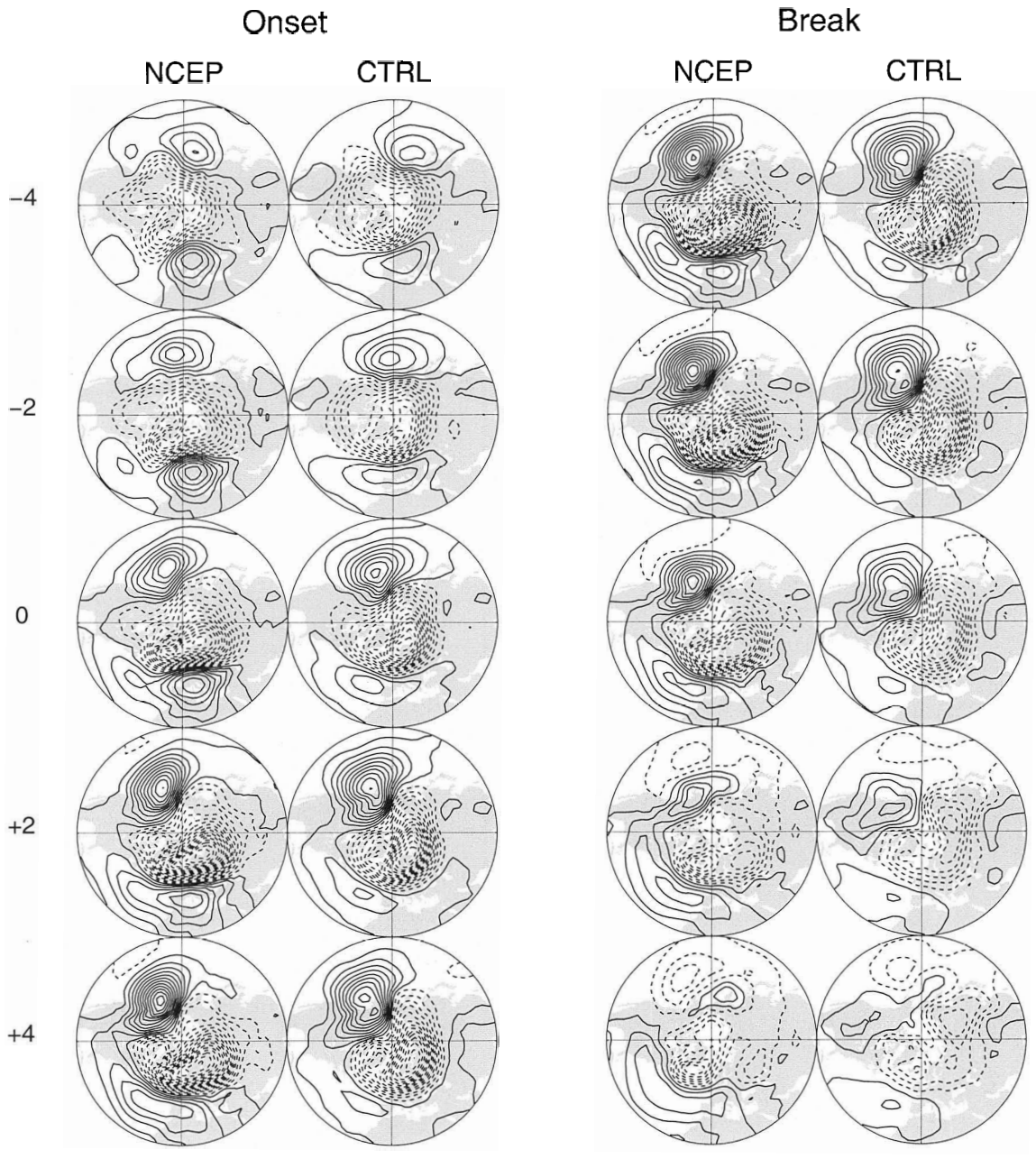

Figure 3.14: Regime R_1 composite evolution. Contour interval: 1.0 hPa (..., -1.5, -0.5, 0.5, ...). Positive (negative) contours are solid (dashed).

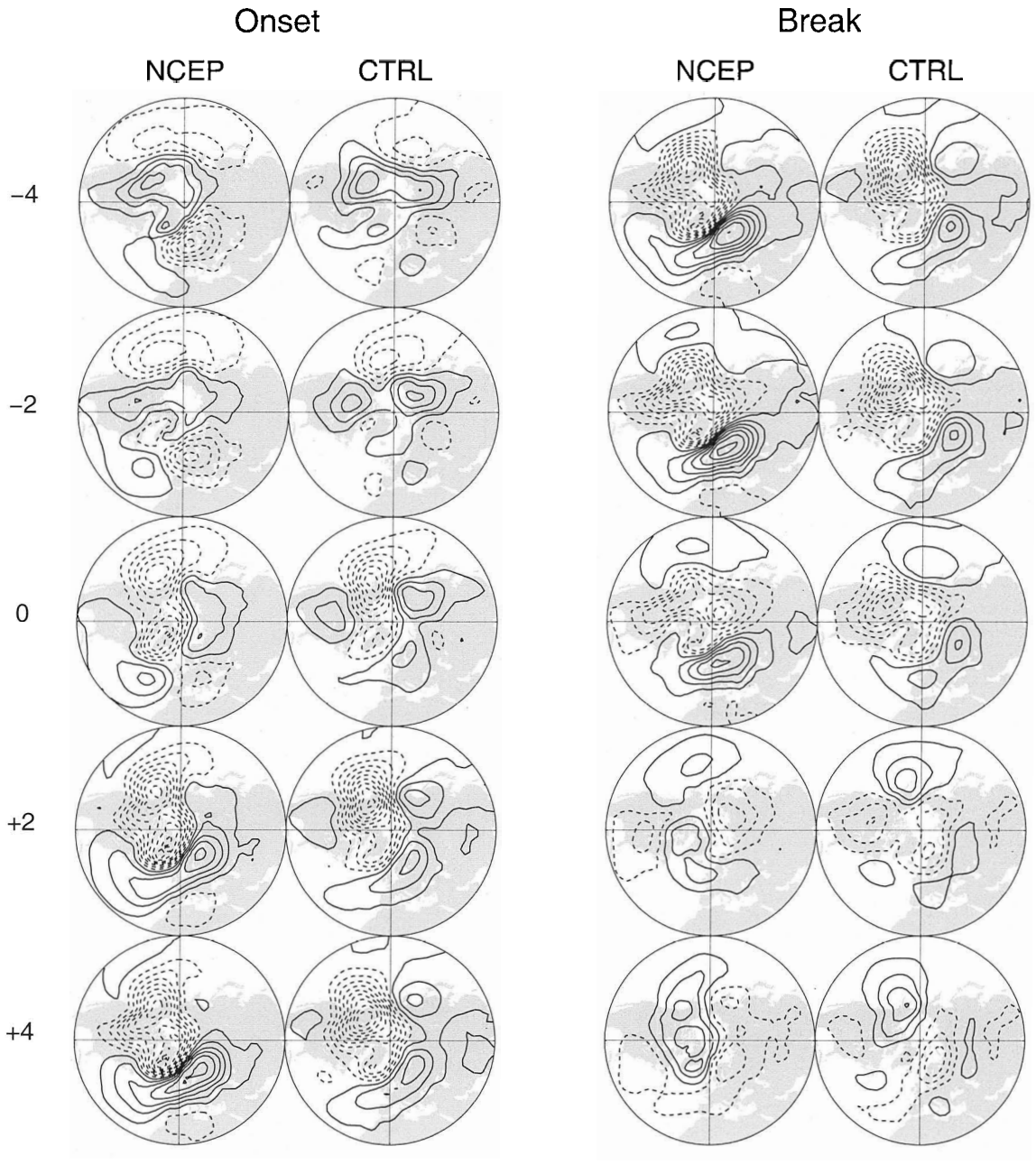

Figure 3.15: As in Figure 3.14, but for regime R_2.

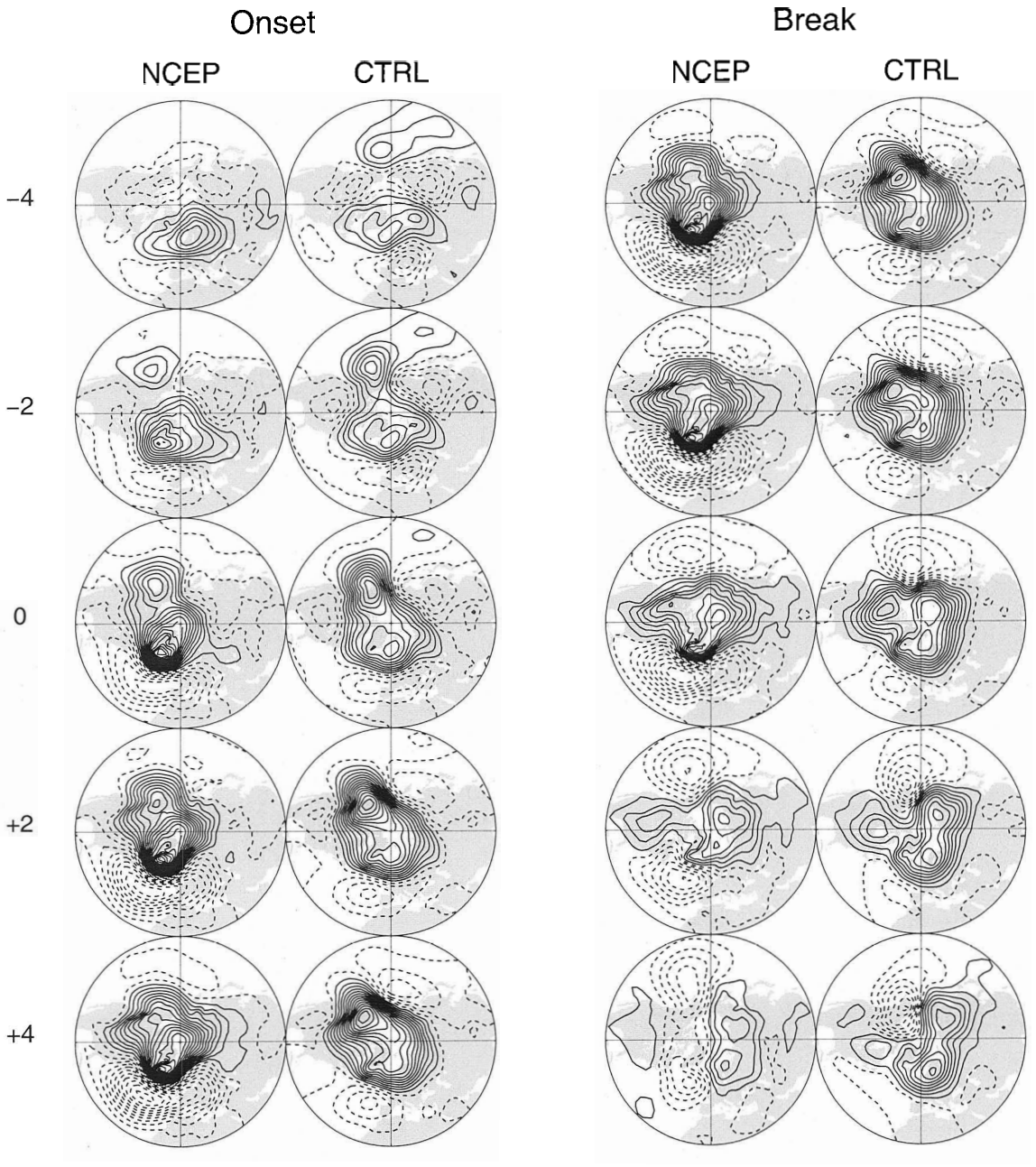

Figure 3.16: As in Figure 3.14, but for regime R_3.

Atlantic region. During break the positive anomalies over North America and the Arctic stretch-out meridionally and split, leaving negative anomalies over the region (in a similar, but oppositely-signed, sense as in regime R_2). The model does a good job at reproducing onset and break evolution for regime R_3. We do note, however, that the simulated center over the west coast of Europe does not retrograde towards Greenland during onset, as is the case in the observations.

It has been noted that some regime transitions may be preferred over others (e.g., Mo and Ghil 1988; Kimoto and Ghil 1993b; Monahan et al. 2001; Crommelin 2003a; 2003b; 2004). The composite onset and break maps shown above have provided some insight into the circulation structures that prevail before regime initiation and after regime termination. Another complementary view of this can be obtained in the space of the leading linear PCs. Figure 3.17 shows the regime R_1 onset and regime R_3 break in the space of the leading linear PCs. For onset, the start and end of an arrow indicates day -4 and day 0, respectively. For break, the start and end of an arrow indicates day 0 and day +4, respectively. Arrows are provided for both the approximation and for the original points that the curve approximates. It would appear that regime R_1 originates from the lower-left quadrant in the vicinity of regime R_2. Similarly, regime R_3 breaks towards regime R_2. So it appears that there are some preferred pathways to and from the regime states. We also note the close agreement between the observations and the model in this regard. These results are broadly consistent with the suggestion by Crommelin (2003a), in which a simple T21 barotropic model is employed to study NH flow, that regime transitions from R_3 to R_1 have a tendency to go via regime R_2. Crommelin (2004) also shows that the reanalyses data exhibit similar preferred transition pathways.

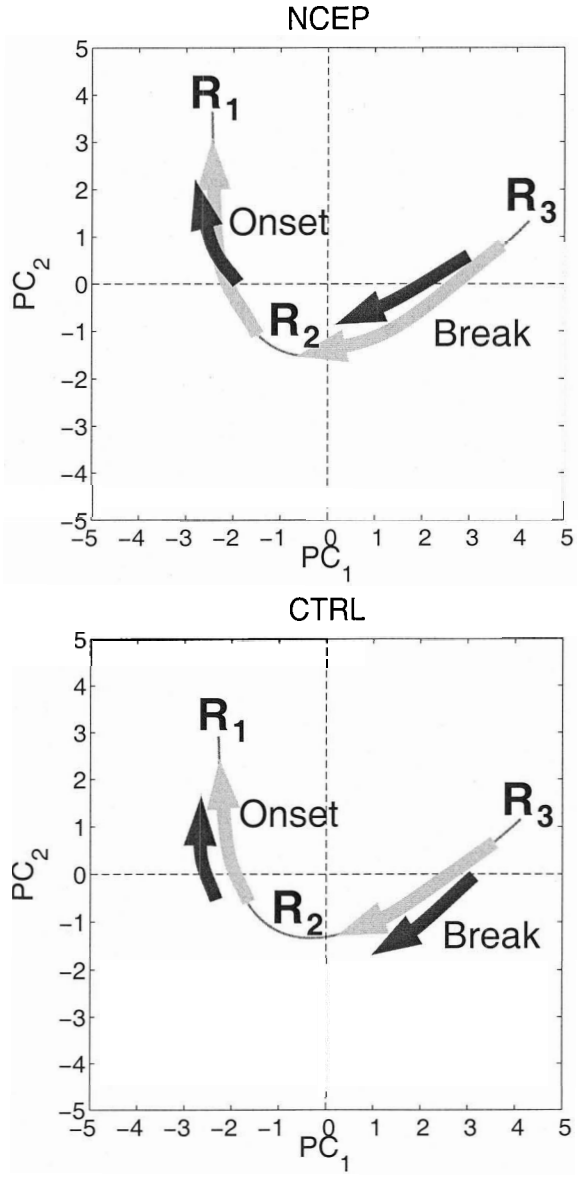

Figure 3.17: Regime evolution for R_1 onset (left) and R_3 break (right). Light arrows are for the approximation. Dark arrows are for the original points that the curve approximates.

3.2.3 Dynamics

Maintenance mechanisms for long-lived atmospheric anomalies, such as those derived here, have been sought extensively in recent decades. Branstator (1992) describes five, more or less distinct, mechanisms. 1) Anomalies are remotely forced by anomalous tropical heating (e.g., Hoskins et al. 1977; Horel and Wallace 1981). 2) Mid-latitude high-frequency transients act to force low-frequency anomalies (e.g., Egger and Schilling 1983; Metz 1989; Lau 1988; Nakamura and Wallace 1990). 3) Low-frequency anomalies are stationary solutions to the governing equations that rely on steady nonlinearities for their self-maintenance (e.g., Verkley 1984; Branstator and Opsteegh 1989). 4) Anomalies are caused by modifications to the propagation characteristics resulting from changes to the zonal-mean flow (e.g., Branstator 1984; Kang 1990; Nigam and Lindzen 1989). 5) Zonal variations in the time-mean state modify low-frequency anomalies induced by other means (e.g., Simmons 1982; Branstator 1983), or serve as internal sources of energy for the perturbations (e.g., Simmons et al. 1983; Branstator 1985).

Based on an analysis of the dominant linear low-frequency patterns found in a GCM, Branstator (1992) concludes that, of the mechanisms described above, two are dominant. To quote, "one mechanism is the dynamical interaction between the anomalies and the time-mean flow and the other is the influence of anomalous transient eddy fluxes". In this subsection we consider both of these mechanisms (to be referred to as low- and high-frequency dynamics) in the context of the leading nonlinear modes of low-frequency variability. To set the stage we show in Figure 3.18 the three-dimensional structure of the leading observed SLP nonlinear modes. The equivalent barotropic centers of action which extend from the surface to the upper troposphere we will refer to as "primary" regime centers (e.g., the North Pacific anomaly

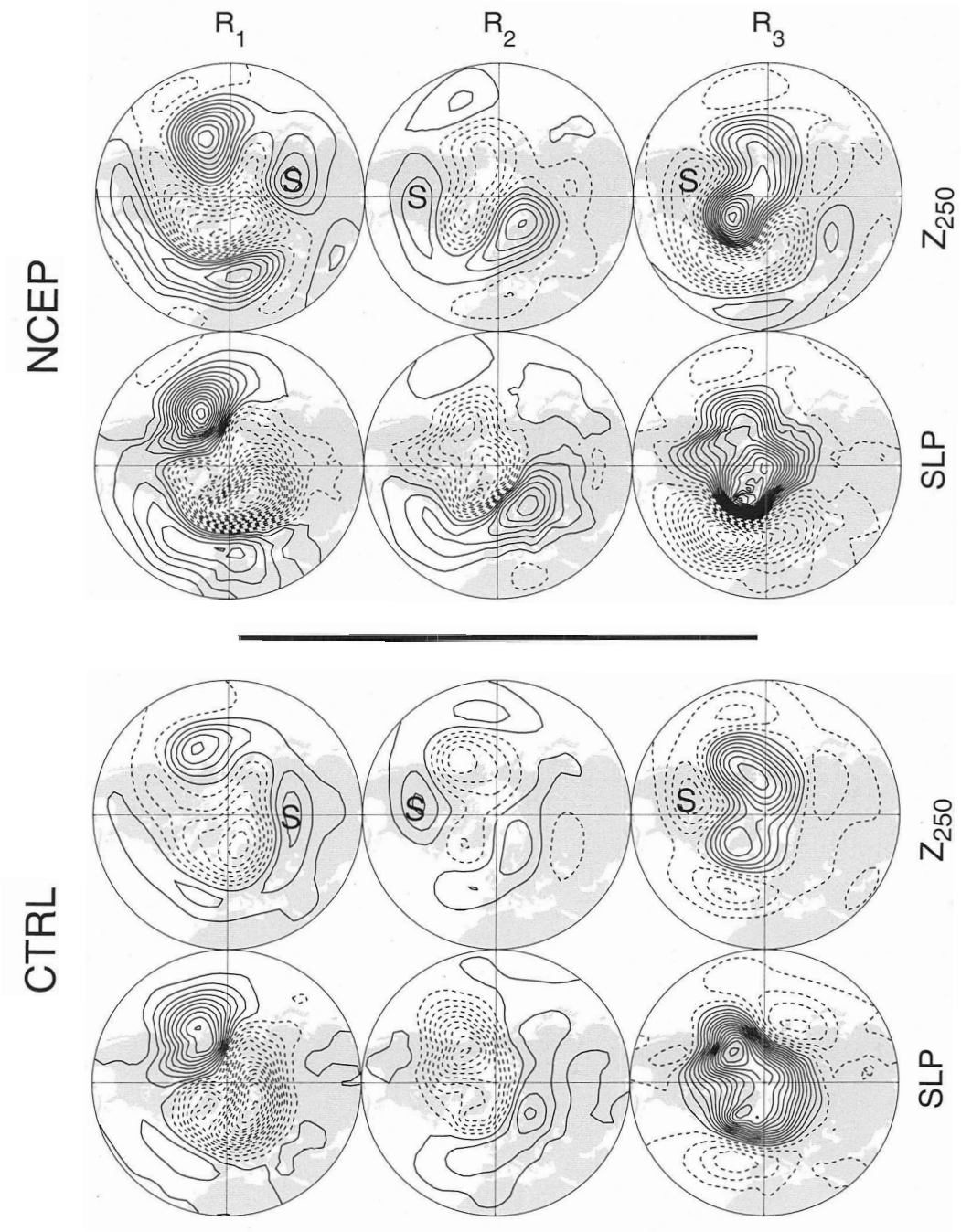

Figure 3.18: Regime maps for anomalous Z_{250} and SLP as indicated. Contour intervals are 20 m (..., -30, -10, 10, ...) for Z_{250} anomalies and 1 hPa (..., -1.5, -0.5, 0.5, ...) for SLP anomalies. Positive (negative) contours are solid (dashed). S denotes a secondary center.

center in regime R_1). On the other hand, the centers which exist only in the middle to the upper troposphere we will refer to as "secondary" regime centers (e.g., the East Asian positive anomaly center in regime R_1). The secondary centers to be discussed here are labeled with a "S" in Figure 3.18. The expectation is that the dynamics underlying the primary and secondary centers will be linked but distinct. Finally, we note that all the calculations in this subsection are based upon 250 hPa data.

Low-Frequency Dynamics

Branstator (1992) notes that the dynamical interaction between low-frequency anomalies and the time-mean flow involve two processes. Namely, the zonal-mean time-mean flow impacts the dispersion of large-scale anomalies (cf. Hoskins and Karoly 1981) and the time-mean eddies modify the dispersion process (cf. Branstator 1983) and act as an internal energy source (cf. Simmons et al. 1983; Branstator 1990). To assess the combined effect of these processes we employ the horizontal component of the pseudo-momentum flux vector **W** recently developed by Takaya and Nakamura (2001), i.e.:

$$\mathbf{W}_h = \frac{1}{2|\mathbf{U}_h|} \begin{pmatrix} U(\psi_x'^2 - \psi'\psi'_{xx}) + V(\psi'_x\psi'_y - \psi'\psi'_{xy}) \\ U(\psi'_x\psi'_y - \psi'\psi'_{xy}) + V(\psi_y'^2 - \psi'\psi'_{yy}) \end{pmatrix}, \tag{3.1}$$

where ψ represents the streamfunction derived from geopotential heights using quasi-geostrophic approximation. This vector applies to small-amplitude, quasi-stationary, quasi-geostrophic disturbances (the primed quantities) superimposed on a zonally-varying basic flow ($\mathbf{U}_h = [U, V]$). It is a generalization of the wave activity flux $\mathbf{F}_s$ of Plumb (1985) defined for a zonally-uniform basic flow. The pseudo-momentum is a conserved quantity. Here it is a linear combination of two quantities which are

proportional to wave enstrophy and wave energy, respectively. Since these two quantities have been shown to represent pseudo-momentum in the zonal mean case (e.g., Andrews and McIntyre 1978; Uryu 1974), Takaya and Nakamura (2001) claim that a linear combination of these two quantities is also related to the pseudo-momentum. They further show that its flux $\mathbf{W}$ is parallel to the local group velocity in the WKB limit and is therefore useful in diagnosing Rossby wave energy propagation and deposition. In this study we use a version of this diagnostic applicable to the sphere and written in such a way as to reduce the amount of successive differentiation (and hence unwanted numerical noise). We take $\mathbf{U}_h$ to be the winter-mean horizontal wind and the primed quantities to be associated with the regime anomalies.

Figures 3.19, 3.20 and 3.21 show composite maps of $\mathbf{W}_h$ (vectors) and Z_{250} anomalies (contours) for regime R_1, R_2 and R_3, respectively. Computed, but not shown, are maps of $\mathbf{W}_h$ divergence. Consider the R_1 maps. An example of a primary center influencing its own evolution through low-frequency Rossby wave dynamics is seen in the North Pacific. Associated with the migration and amplification of the North Pacific anomaly there is eastward-directed $\mathbf{W}_h$ indicative of downstream Rossby wave energy propagation (seen especially after onset day 0 and into break). Immediately upstream we find $\mathbf{W}_h$ divergence (i.e., wave energy emission) and immediately downstream $\mathbf{W}_h$ convergence (i.e., wave absorption), which presumably contributes to the growth of the anomaly center. An example of a primary center affecting a secondary center through low-frequency Rossby wave dynamics is seen over Eastern Eurasia. The secondary center seen over Eastern Eurasia appears associated with Rossby wave energy propagation originating from an upstream primary center (i.e., the negative anomalies centered over Northern Scandinavia). Further examples of this behavior are seen in the other regime maps. For example, consider the positive (negative) anomalies

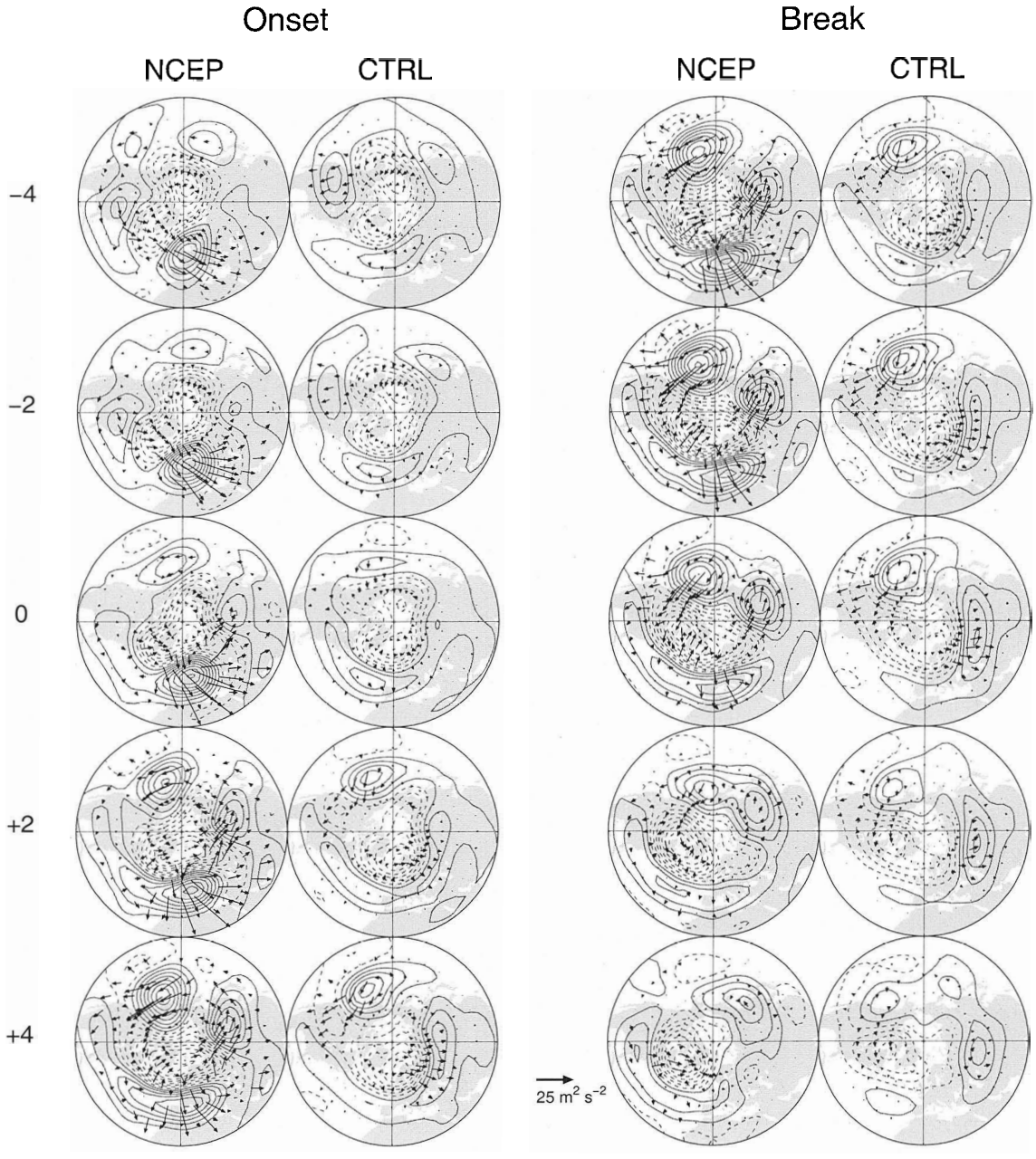

Figure 3.19: Regime R_1 composite evolution of $\mathbf{W}_h$ (arrows) and 10-day low-pass filtered Z_{250} anomalies (contours). Contour interval: 20 m (..., -30, -10, 10, ...). Positive (negative) contours are solid (dashed). Scaling for the arrows is shown below.

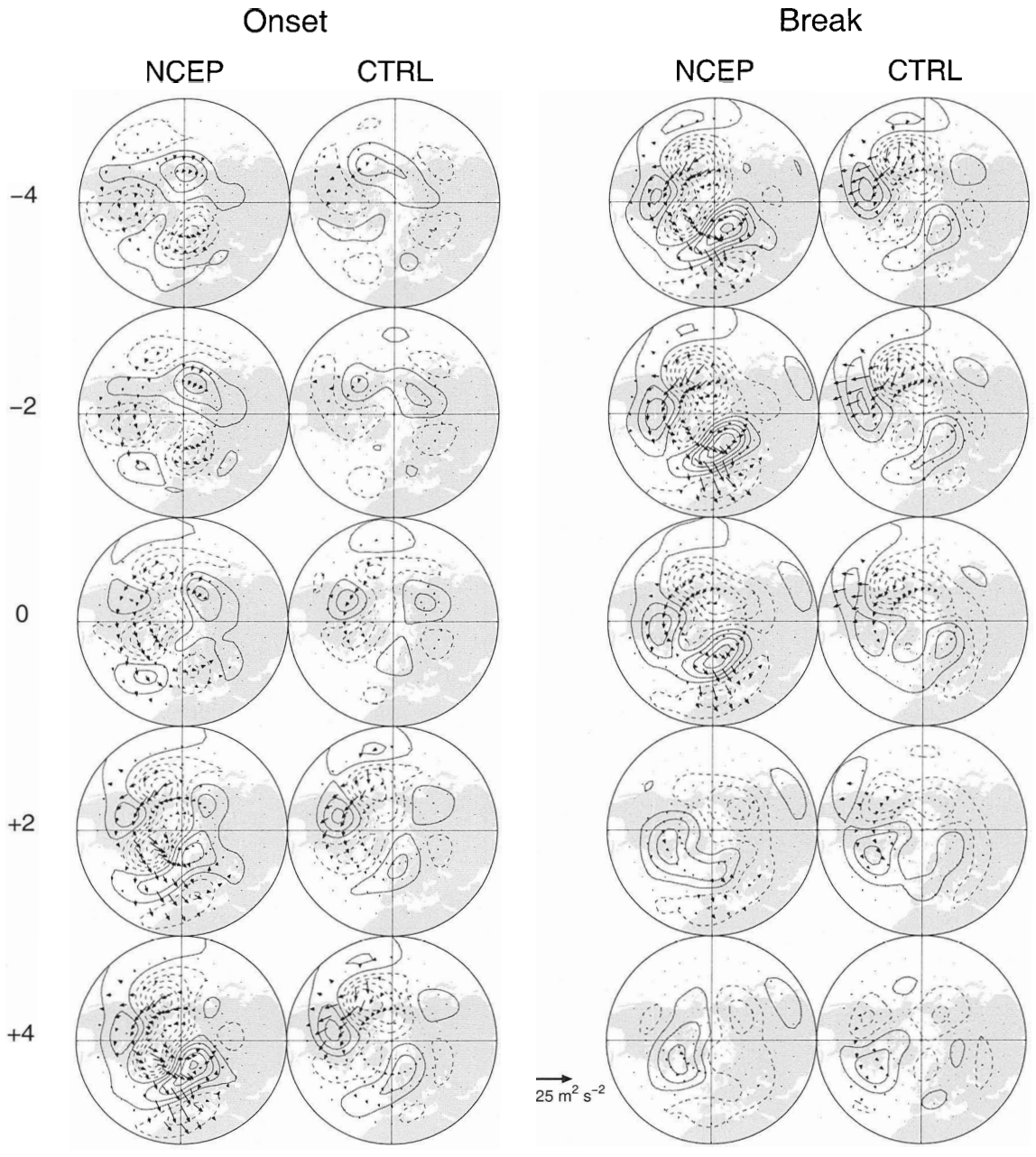

Figure 3.20: As in Figure 3.19, but for regime R_2.

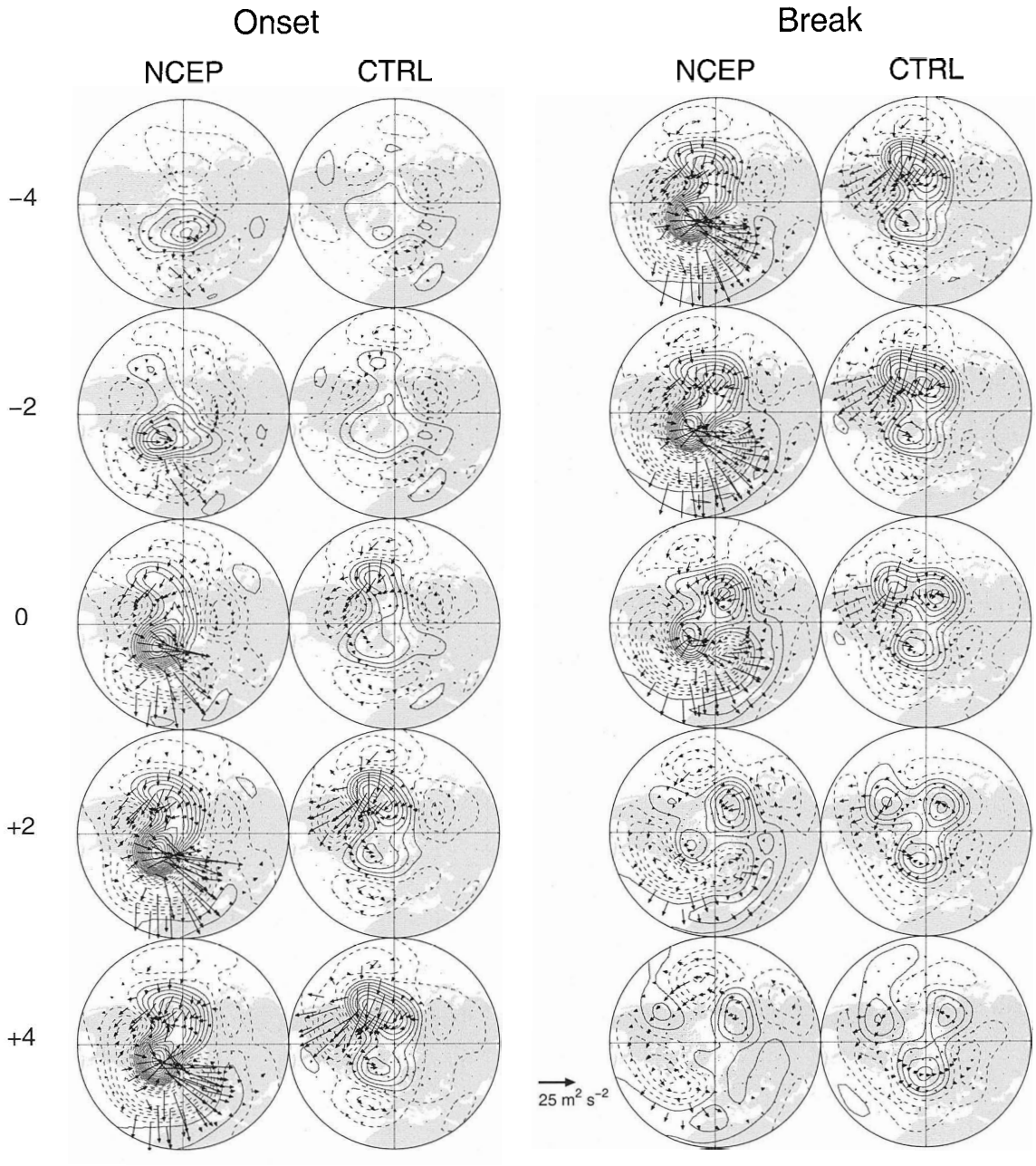

Figure 3.21: As in Figure 3.19, but for regime R_3.

which develop over North America in regime R_2 (R_3). These secondary centers are associated with Rossby wave energy propagation originating from an upstream primary center located in the North Pacific.

So it appears that the regime anomalies (both primary and secondary) involve low-frequency dynamical interactions between themselves and the time-mean flow. We now turn to the role of the high-frequency transient eddies.

High-Frequency Dynamics

Previous studies suggest that anomalous vorticity fluxes by high-frequency transient (i.e., synoptic) eddies are important in maintaining long-lasting tropospheric flow anomalies (e.g., Lau 1988; Tsou and Smith 1990; Nakamura and Wallace 1990; 1993). At the same time there is evidence that these fluxes do not occur randomly but are organized by the low-frequency flow anomalies themselves. As noted in Branstator (1995) the low-frequency flow anomalies can act on the synoptic eddies by at least three mechanisms: 1) by changing the position and strength of the baroclinic zones; 2) by changing the principal routes taken by the storms through the modification of the steering winds or 3) by changing the structure of the individual storms through stretching and straining. In this subsection we consider the organization of the eddies as well as the feedbacks that ensue.

Synoptic eddies can be idealized as migratory disturbances propagating on a background zonally-varying basic flow. In this study we take the background flow to be the 10-day low-pass filtered horizontal 250 hPa winds. Since the high-frequency transient eddies are generally elongated in the direction perpendicular to the local basic flow (Hoskins et al. 1983), the wind fluctuations perpendicular to the instantaneous local basic flow are mainly associated with the high-frequency transient eddies. Hence, a

useful and simple measure of high-frequency transient eddy amplitude is:

$$A^H = (2\overline{v_\perp^2})^{1/2}, \tag{3.2}$$

where the overbar denotes 10-day low-pass filtering and $v_\perp$ represents the instantaneous wind component perpendicular to the local basic flow (Nakamura et al. 1997). Figure 3.22 shows winter-mean A^H. Large values of A^H roughly correspond to the storm tracks in the North Pacific and Atlantic (cf. Figure 3.3 right). Except for slight eastward displacement the model produces a fairly realistic representation of mean storm track positions and amplitudes.

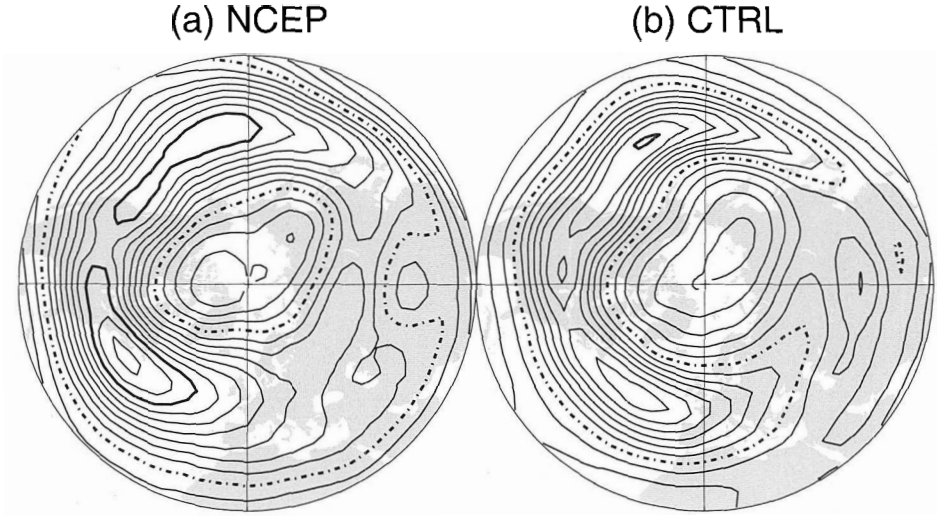

Figure 3.22: Winter-mean A^H. Contour interval: 1 m/s, with the 10 (17) m/s contour in bold dash-dot (bold solid).

Figures 3.23 and 3.24 show the onset of anomalous A^H (black contours) superimposed on 10-day low-pass filtered anomalous height (gray contours) for the observations and model, respectively. (For the sake of brevity we do not show the corresponding break plots.) Consider regime R_1. The positive height anomalies which establish

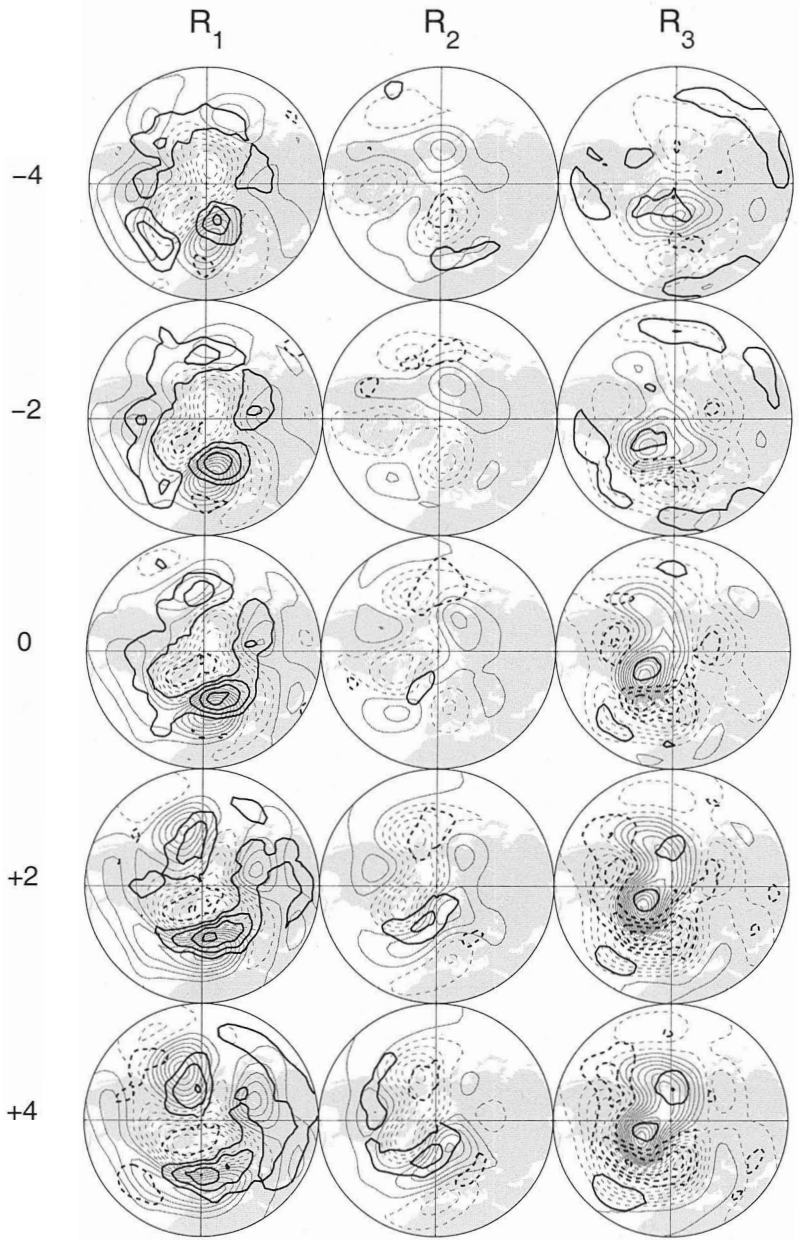

Figure 3.23: Observed composite evolution of anomalous A^H (black contours) and anomalous Z_{250} (gray contours). Contour intervals for Z_{250} anomalies are 20 m (..., -30, -10, 10, ...), for anomalous A^H are 1 m/s (..., -2, -1, 1, ...), with the zero contour omitted. Positive (negative) contours are solid (dashed).

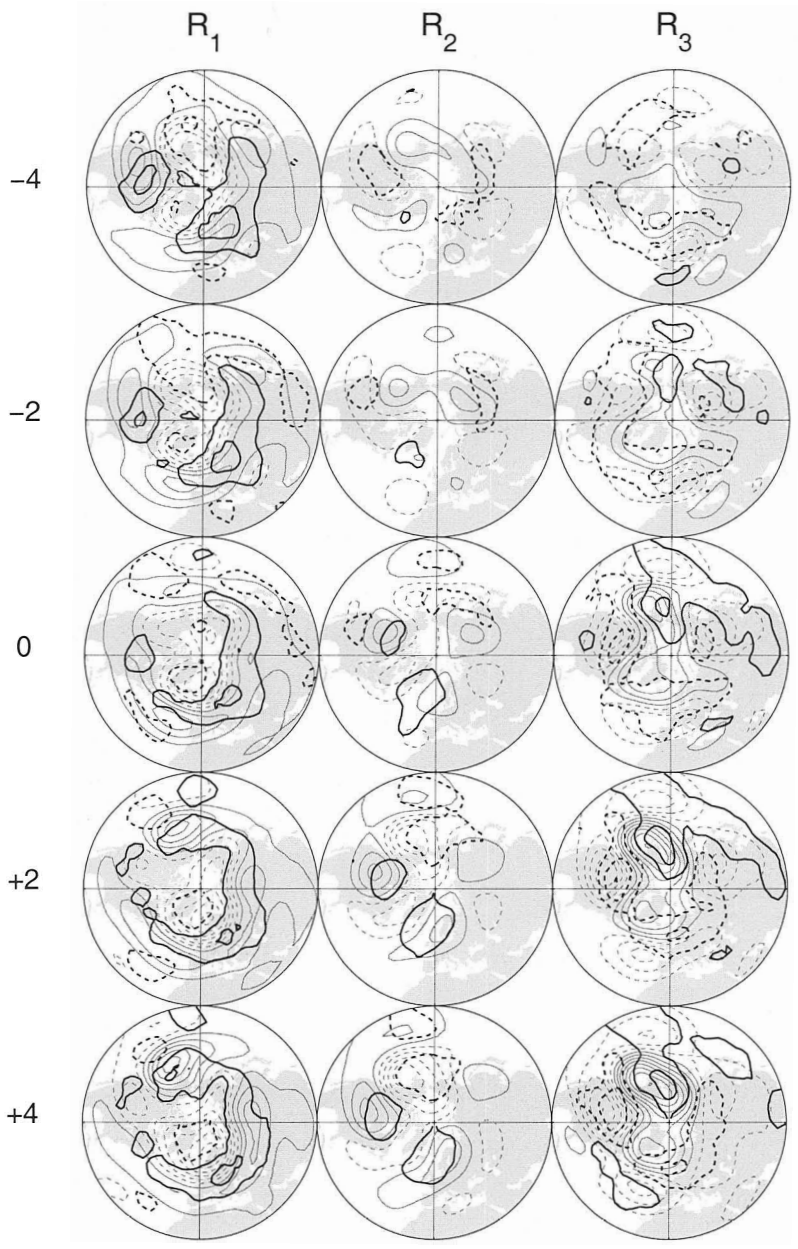

Figure 3.24: As in Figure 3.23, but for the control simulation. Contour interval for anomalous A^H is 1.0 m/s (..., -1.5, -0.5, 0.5, ...).

over the North Pacific are associated with enhanced synoptic eddy activity to the north. This makes sense in terms of the anomalous circulation steering the synoptic eddies in a more northerly path than is usually the case. The dipole-structured height anomalies which establish over Northern Europe induce increased westerlies and are associated with enhanced synoptic eddy activity. A similar feature is seen over the northeast Atlantic in regime R_2. Presumably, the increased westerlies increase the vertical wind shear and hence enhance the eddy activity. Further work is required to draw definitive conclusions. Now consider regime R_3. The dipole structure which develops over the North Atlantic is associated with reduced synoptic eddy activity along the climatological storm track region (cf. Figure 3.22) and enhanced synoptic eddy activity to the north and south. Again, this consistent with the anomalous circulation steering the synoptic eddies off their usual paths. In short, the regime circulations affect changes in the magnitude and position of the synoptic eddies. Next, we attempt to demonstrate that the changed synoptic environment in turn affects the regime circulations.

To assess synoptic eddy feedback we compute the high-frequency vorticity flux appearing in the low-pass filtered height tendency equation,

$$\left(\frac{\partial \overline{Z}}{\partial t}\right)^H \equiv \frac{f_0}{g} \bigtriangledown^{-2} [-\nabla \cdot (\overline{\mathbf{u}''\xi''} + \overline{\overline{\mathbf{u}}\xi''} + \overline{\mathbf{u}''\overline{\xi}})], \tag{3.3}$$

where $\mathbf{u}$ and ξ are horizontal wind and relative vorticity, respectively. In this expression the overbars and double primes signify 10-day low-pass and 10-day high-pass filtered quantities, respectively. In all of our calculations the last two terms on the right-hand-side (which arise due to the imperfect separation between high- and low-frequencies) have been found to be negligible. Figure 3.25 shows winter-

mean $\left(\partial\overline{Z}/\partial t\right)^H$. Positive (negative) tendency contours denote anti-cyclonic (cyclonic) forcing of the low-frequency height tendency by the synoptic eddies. Strong cyclonic forcing is found where the synoptic eddies are known to amplify, i.e., the climatological storm tracks in the Pacific and Atlantic. These positions also coincide with local jet streams which are known to partly owe their existence to the synoptic eddies. The model does a reasonable job at reproducing these features. However, the model does underestimate the cyclonic forcing over the storm tracks, and in the Pacific the forcing is displaced eastward relative to the observations.

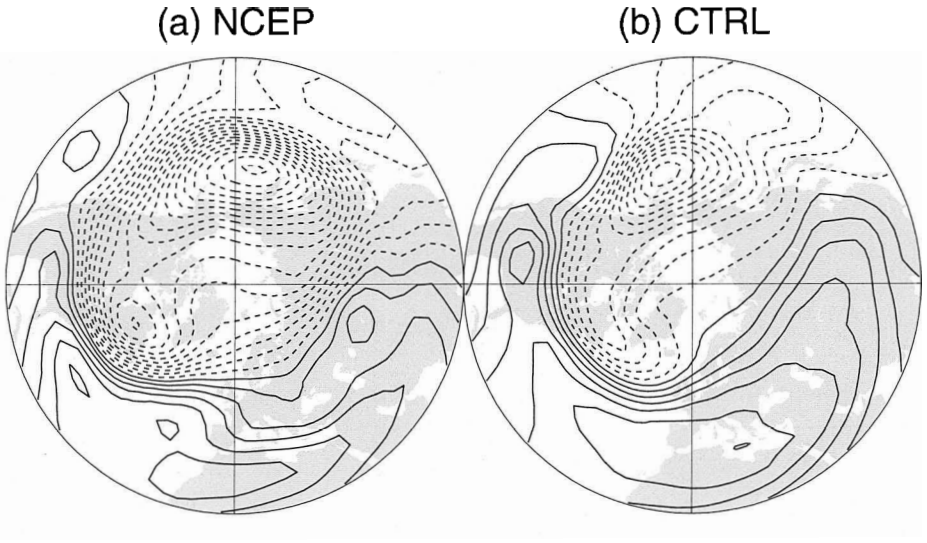

Figure 3.25: Winter-mean $\left(\partial\overline{Z}/\partial t\right)^H$. Contour interval is 5.0 (..., -7.5, -2.5, 2.5, ...) $\times 10^{-5}$ m/s. Positive (negative) contours are solid (dashed).

Figures 3.26, 3.27 and 3.28 show composite maps of $\left(\partial\overline{Z}/\partial t\right)^H$ for regimes R_1, R_2 and R_3, respectively. Consider regime R_1. We remind the reader that the primary centers for this regime are found over the North Pacific and eastern Atlantic. As we can see in Figure 3.26 these centers are associated with synoptic eddy forcing which

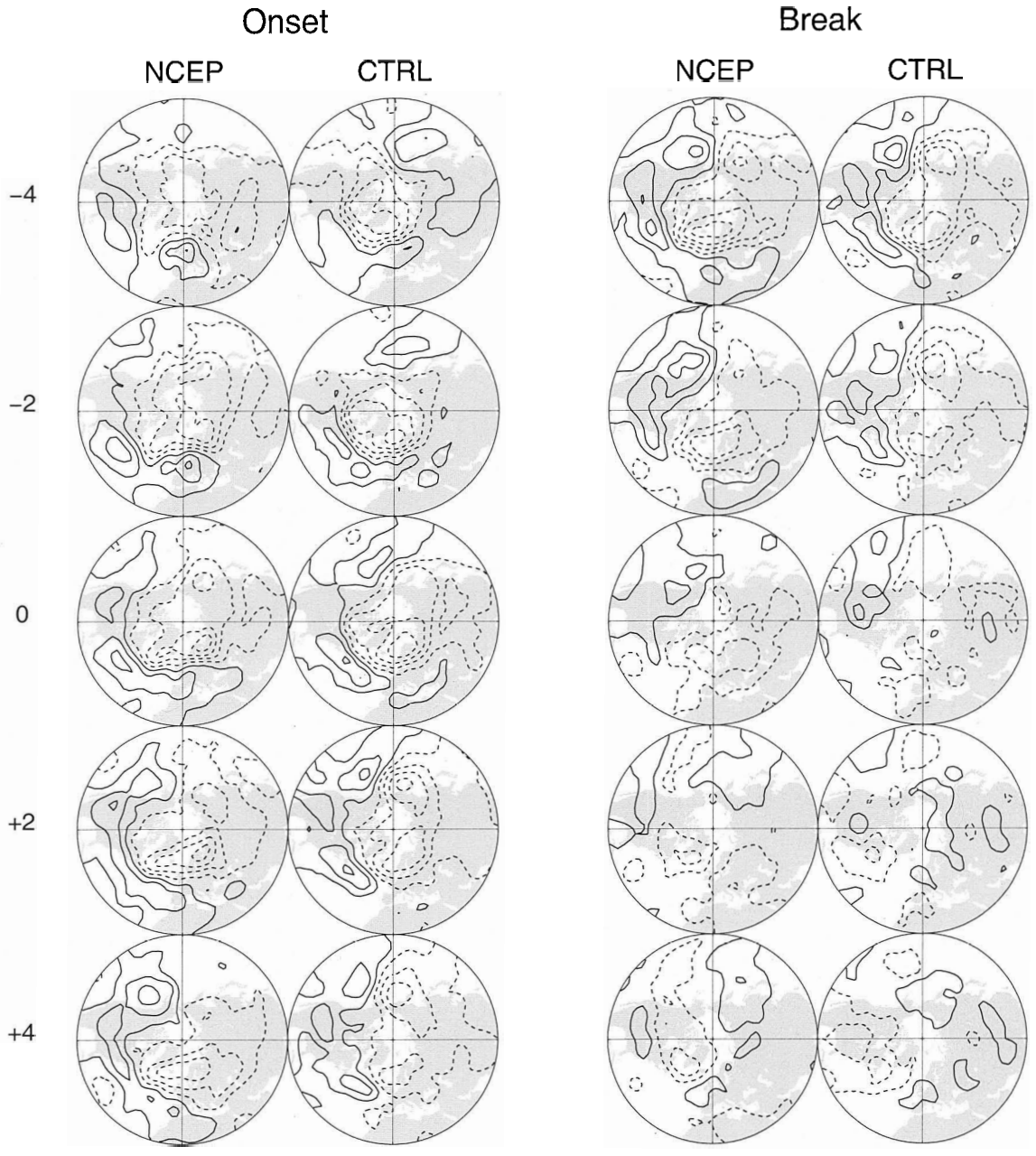

Figure 3.26: Regime R_1 composite evolution of anomalous $\left(\partial\overline{Z}/\partial t\right)^H$. Contour interval is 10.0 m/day (..., -15.0, -5.0, 5.0, ...) for the observations and 5.0 m/day (..., -7.5, -2.5, 2.5, ...) for the simulation. Positive (negative) contours are solid (dashed).

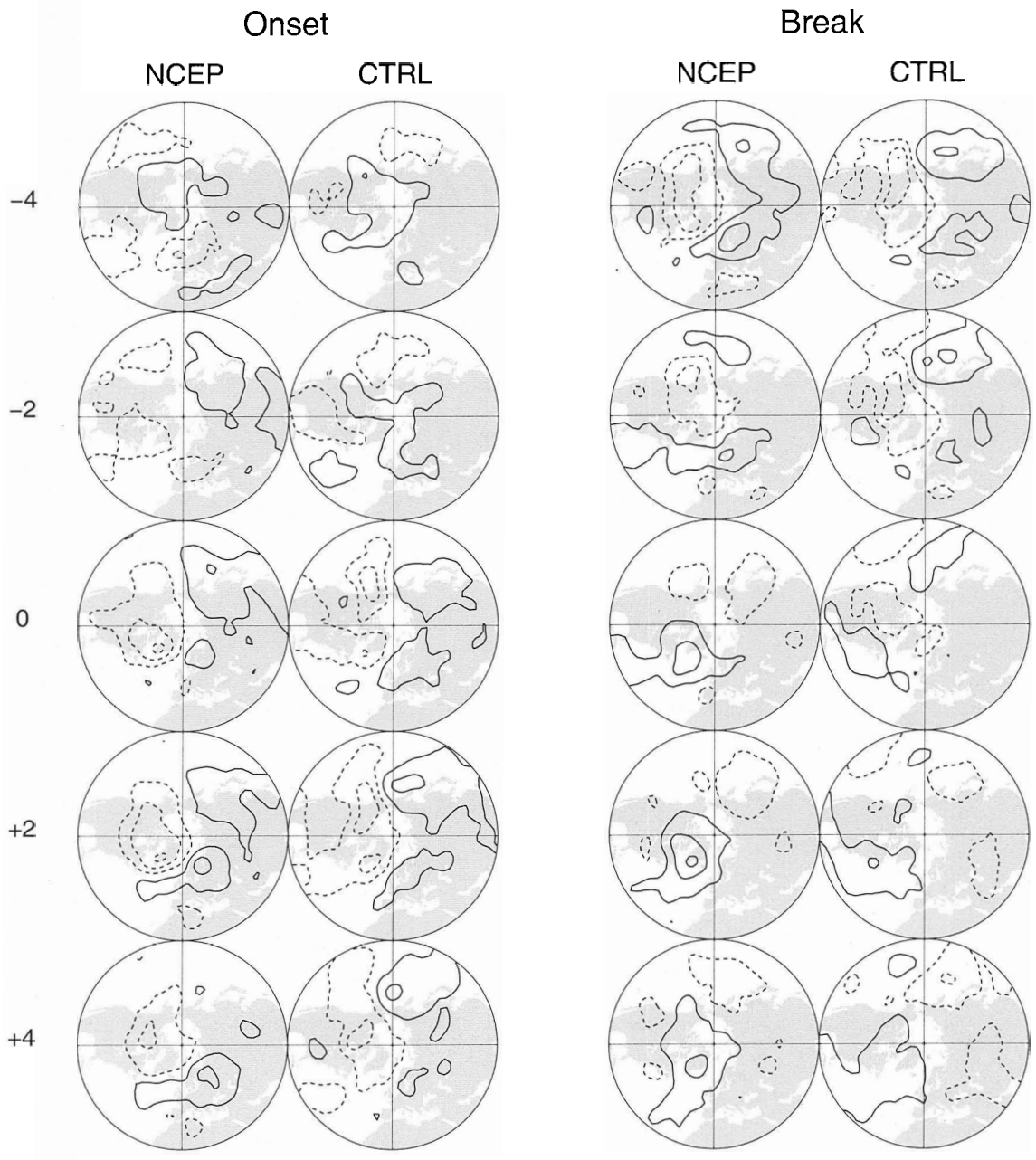

Figure 3.27: As in Figure 3.26, but for regime R_2.

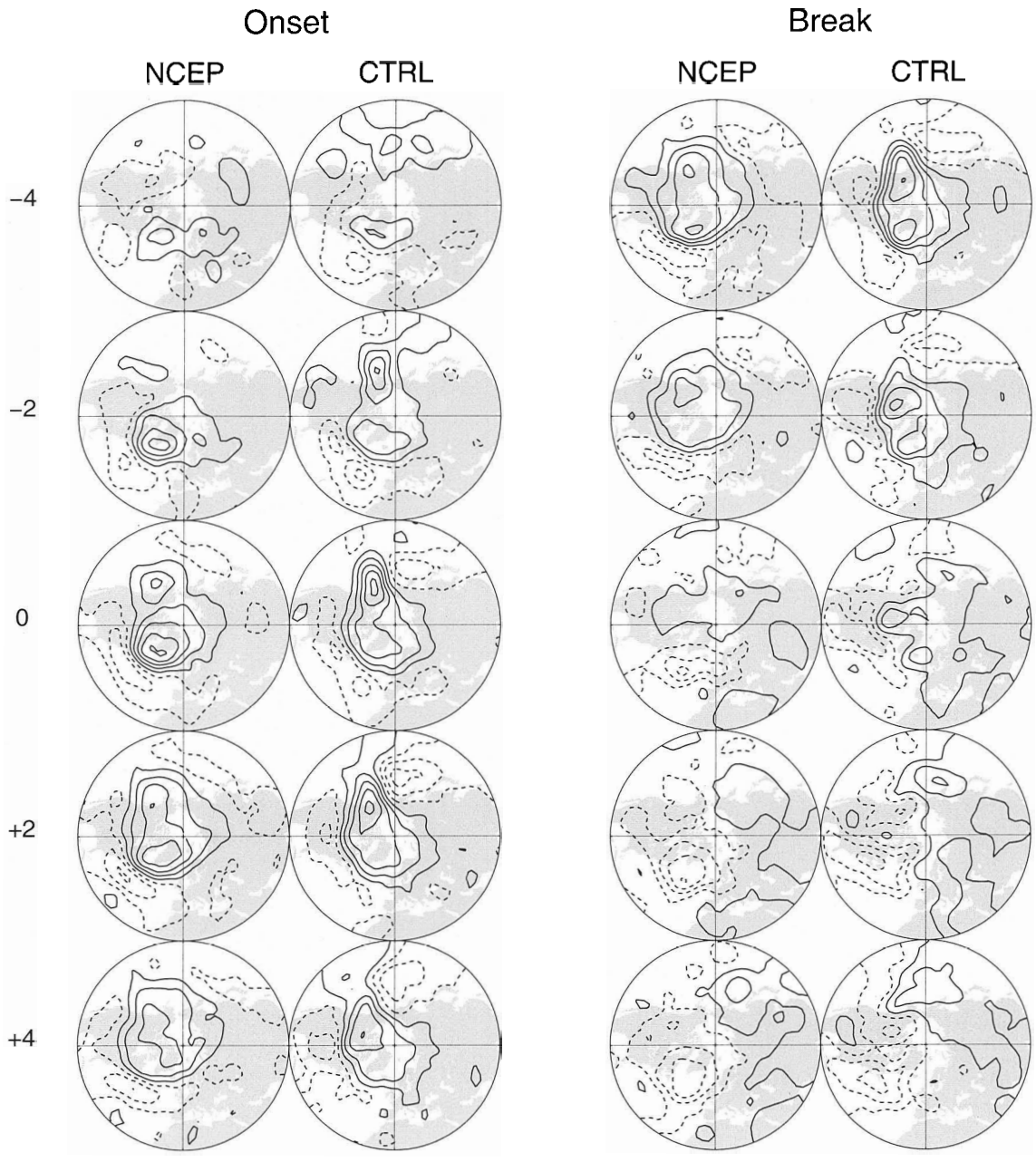

Figure 3.28: As in Figure 3.26, but for regime R_3.

would tend to reinforce the anomalies. In other words, the synoptic eddy forcing exerts a positive feedback on these primary flow anomalies by forcing the anomalies during onset and sustaining them through break. We also remind the reader that this regime has a pronounced secondary center consisting of positive anomalies over eastern Eurasia. Interestingly, these secondary anomalies are associated with negative $\left(\partial\overline{Z}/\partial t\right)^H$ which indicates a negative synoptic eddy feedback. That the synoptic eddies appear to work against the secondary centers and in favor of the primary centers is seen in the other regime maps as well.

A more quantitative assessment of the role of the synoptic eddies on the low-frequency regime anomalies is available by computing the integrated effect of the synoptic eddy forcing to day n as: $\overline{Z}_n^H \equiv \overline{Z}_{-4} + \sum_{i=-3}^{n} \left(\partial\overline{Z}/\partial t\right)_i^H \triangle t$ where $n = -3, -2, \ldots, 4$ and $\triangle t = 1$ day. In words, $\overline{Z}_n^H$ is what the regime anomalies would be if synoptic eddy forcing was acting alone since onset (or break) day -4. Figures 3.29, 3.30 and 3.31 show composite maps of $\overline{Z}_n^H$ for regimes R_1, R_2 and R_3, respectively. Consider regime R_1 onset. This diagnostic shows that the primary centers in the North Pacific and Eastern Atlantic are at least partly explained by a positive feedback from the synoptic eddies. On the other hand, the synoptic eddy forcing cannot produce the secondary center seen in Eastern Siberia. This secondary center would appear to owe its existence to the low-frequency dynamics described in the previous subsection. Once again, this behavior whereby the synoptic eddies work against the secondary centers and in favor of the primary centers is seen in the other regime onsets as well. During break, the synoptic eddy forcing still sustain the primary centers. In other words, the synoptic eddy forcing tends to oppose the break (comparing the break evolution in Figures 3.29 to 3.31 with contours in Figures 3.19 to 3.21). Therefore, the regime break should be attributed to the low-frequency dynamics. This kind of

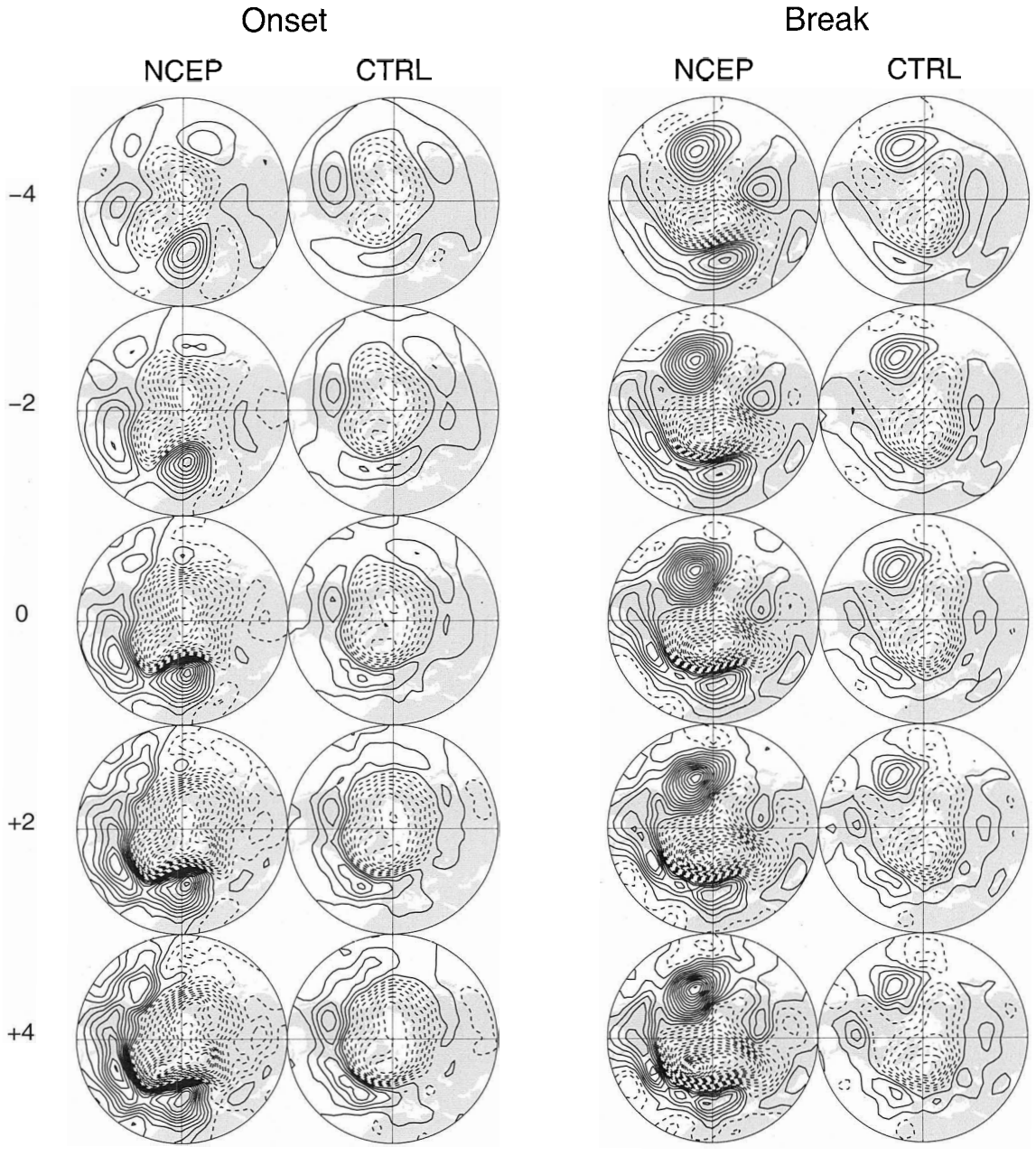

Figure 3.29: Regime R_1 composite evolution of Z_{250} anomalies assuming synoptic eddy forcing is acting alone. Contour interval: 20 m (..., -30, -10, 10, ...). Positive (negative) contours are solid (dashed).

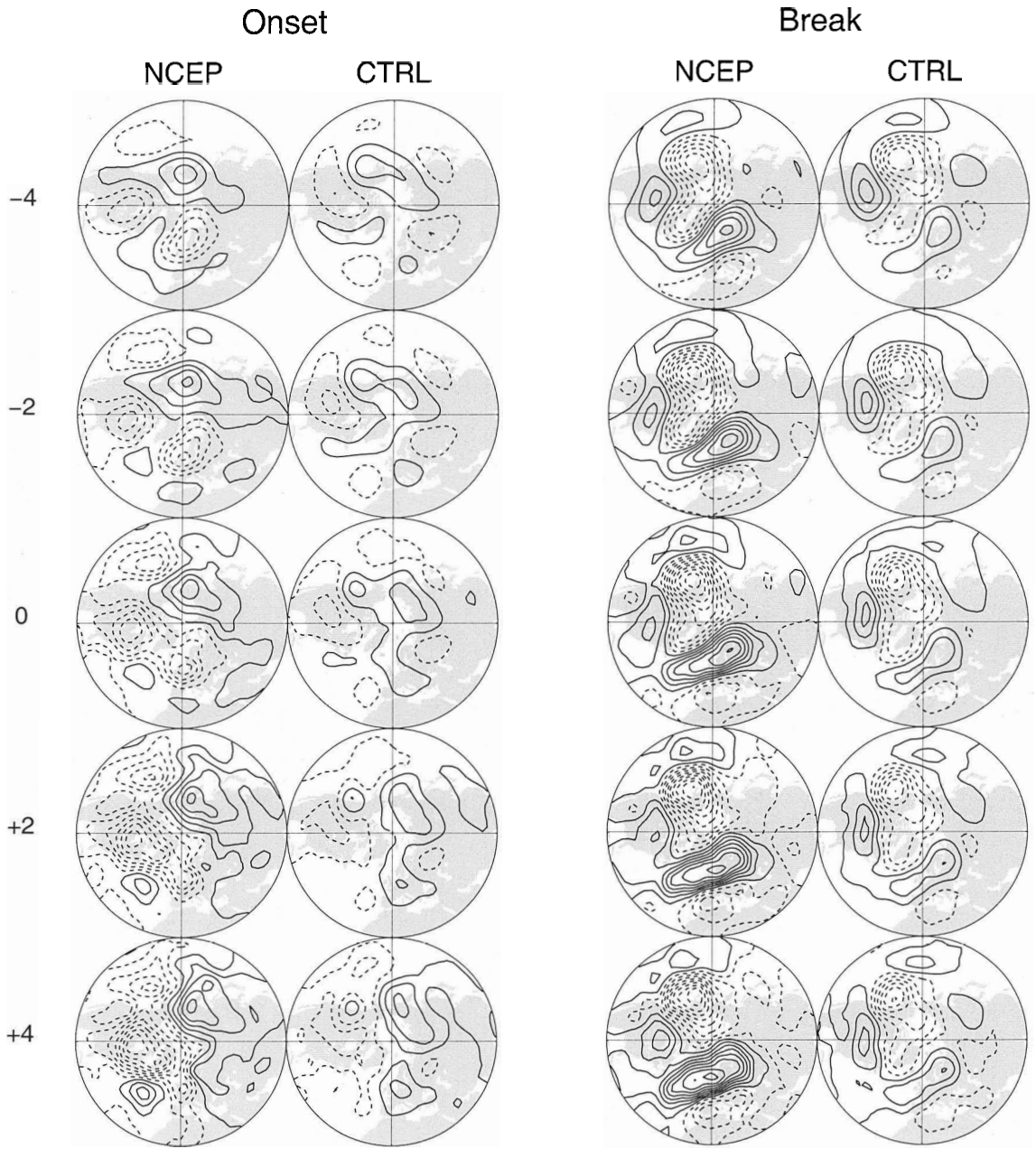

Figure 3.30: As in Figure 3.29, but for regime R_2.

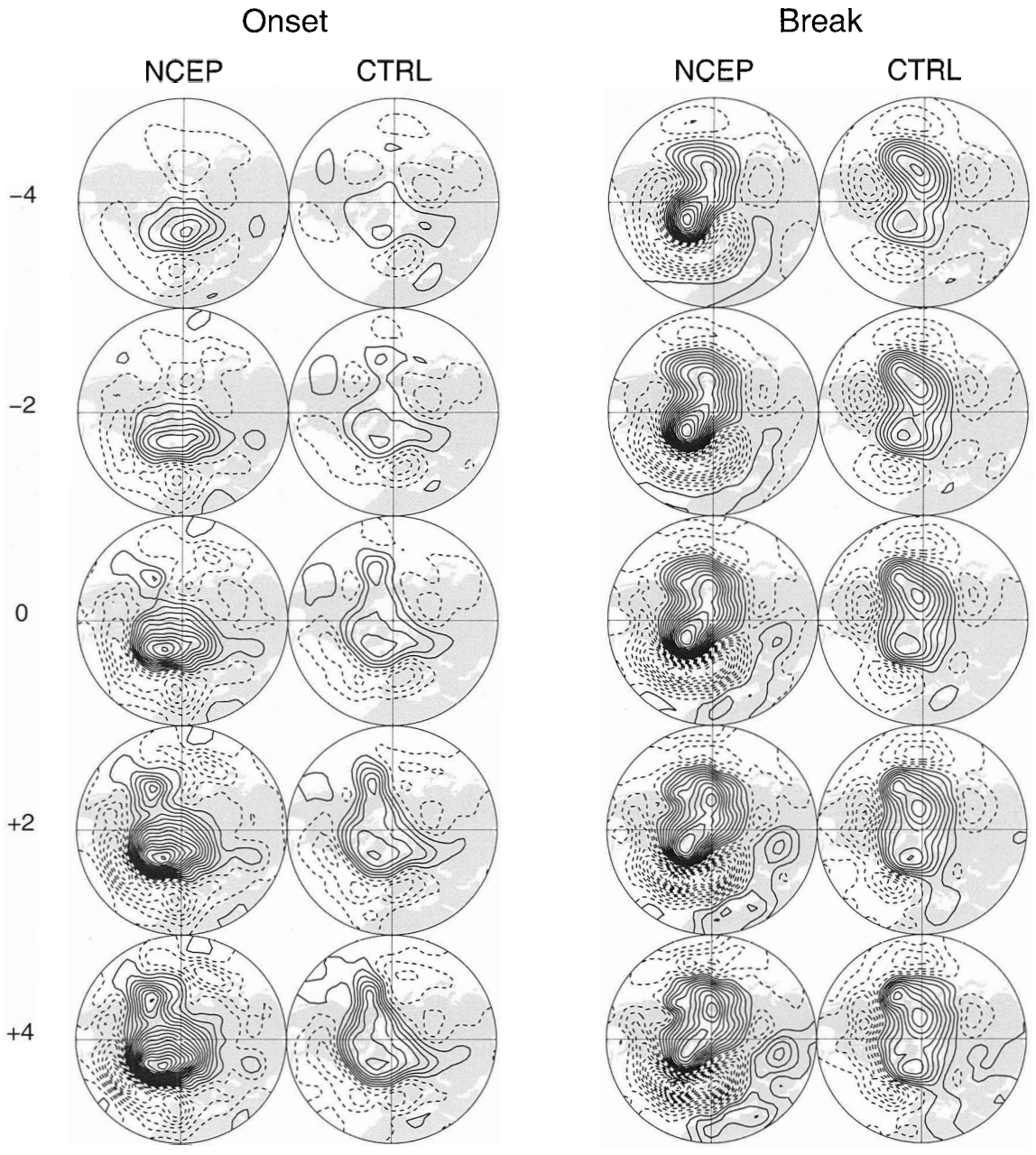

Figure 3.31: As in Figure 3.29, but for regime R_3.

behavior has been seen with atmospheric blocks in previous studies by Nakamura et al. (1997), Dole (1983; 1986; 1989) and Black (1997).

Figure 3.32 schematically summarizes the low- and high-frequency dynamics which appear involved in the onset evolution of the regime anomalies. The primary centers (i.e., barotropic centers extending from the surface to the upper troposphere) emit Rossby wave energy in the downstream direction which force secondary centers (i.e., baroclinic centers existing only from the middle to the upper troposphere). At the same time the low-frequency flow anomalies organize the synoptic eddies (presumably through steering and/or changing the strength of the baroclinic zones) in such a way that the synoptic eddies feedback positively on the primary centers, and negatively on the secondary centers. Why the synoptic eddies act differently with respect to the primary and secondary centers is unknown at this time. This may be related to the fact that the primary centers are found in the storm track regions while the secondary centers are not. Another possibility is that the synoptic eddies, having been steered away by the primary regime anomalies, are not available in the downstream direction where they would otherwise exert a positive feedback on downstream perturbations.

3.3 Summary

Low-frequency northern hemispheric SLP exhibits three regime states, which are reasonably well simulated by a control simulation of the CGCM1. Regime R_1 is characterized by a positive anomaly center over the Aleutians, a negative center over the Arctic and a positive center over the northeast Atlantic. Regime R_2 is characterized by a negative anomaly center extending from the northeast Pacific to Greenland and a positive anomaly center over northern Europe. Regime R_3 consists of a strong merid-

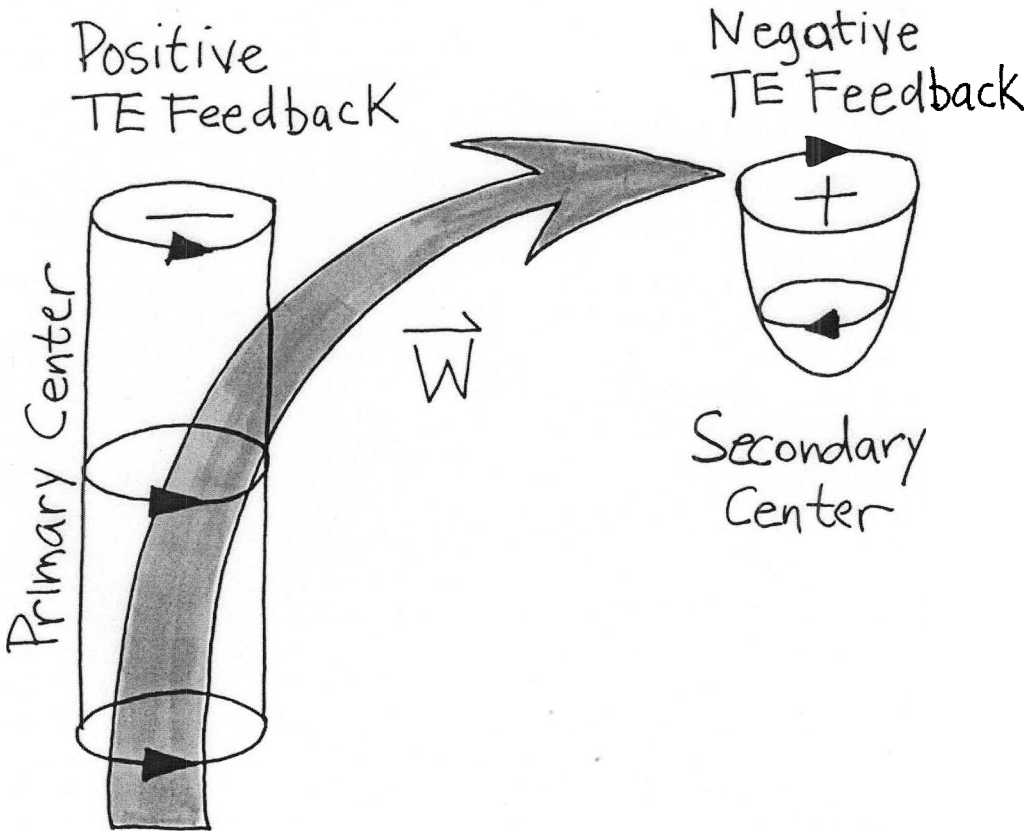

Figure 3.32: Schematic representation of the role of low- and high-frequency dynamics involved in regime onset evolution. TE denotes high-frequency transient eddy.

ional dipole over the North Atlantic region and resembles the negative phase of the AO/NAO. The average time spent in a given regime is about 7 days, with longer events dominating short events. Low- and high-frequency dynamics are both crucially involved in both the onset and break stages of regime evolution. Low-frequency Rossby wave energy propagation associated with the primary regime anomalies appears to account for secondary features seen only in the upper troposphere. Additionally, the primary flow anomalies organize the synoptic eddies in such a way that the synoptic eddies feedback positively upon the primary centers and negatively on the secondary centers.

Chapter 4

Nonlinear Variability in the Near Future

In this chapter we compare the leading nonlinear modes from the control and stabilization simulations. A particular point of interest is Palmer's hypothesis that global warming affects regime residence frequency significantly but not spatial structure. We remind the reader that the stabilization simulations have their CO_2 and sulphate aerosol values fixed at values representative of year 2050 and 2100. In terms of CO_2 this corresponds roughly to a tripling and quadrupling of concentration relative to the control simulation, respectively. Hereafter, we refer to the stabilization simulations as the S2050 and S2100 simulations. In Sections 4.1 and 4.2 we describe the basic statistical and nonlinear mode changes, respectively. We summarize in Section 4.3.

4.1 Basic Statistics

Figure 4.1 (left) shows the winter-mean SLP and its change under global warming. Under global warming the Aleutian low deepens and expands, while the Icelandic low shifts north-eastward towards the Norwegian sea. Figure 4.1 also shows the winter-mean 500 hPa (middle) and 250 hPa (right) geopotential height fields and their change under global warming. In this display the zonal mean height has been removed so as to accentuate the zonally-asymmetric response and its change under global warming. Under global warming there are generally decreased heights over the mid-latitude oceans especially on their eastern boundaries. There are generally increased heights over the mid-latitude land masses as a "direct" thermal response to greater warming over land than over the oceans. Other GCMs have shown similar results (e.g. Joseph et al. 2003).

Figure 4.2 shows the winter-mean zonal-mean profiles of 250 hPa (top) and 500 hPa (bottom) geopotential height. At both levels, and all displayed latitudes, the zonal-mean geopotential height increases under global warming. Of particular interest is the slope of the difference curve (triangles). By geostrophy a positive slope to the difference curve implies decreased zonal-mean westerlies, while a negative slope implies increased zonal-mean westerlies. It follows that under global warming that the high-latitude westerlies decrease, and that the mid-latitude westerlies increase (excepting for the 35°to 43° latitude band at 500 hPa).

Figure 4.3 (left) shows the winter-mean zonal wind at 250 hPa and its change under global warming. Consistent with the high-latitude change noted in Figure 4.2 we see reduced westerlies north of 70°, particularly in the vicinity of the Greenland sea. Under global warming we also note that the Pacific jet is shifted southward, especially in its exit region off the Pacific Northwest. The Atlantic jet is also southward shifted

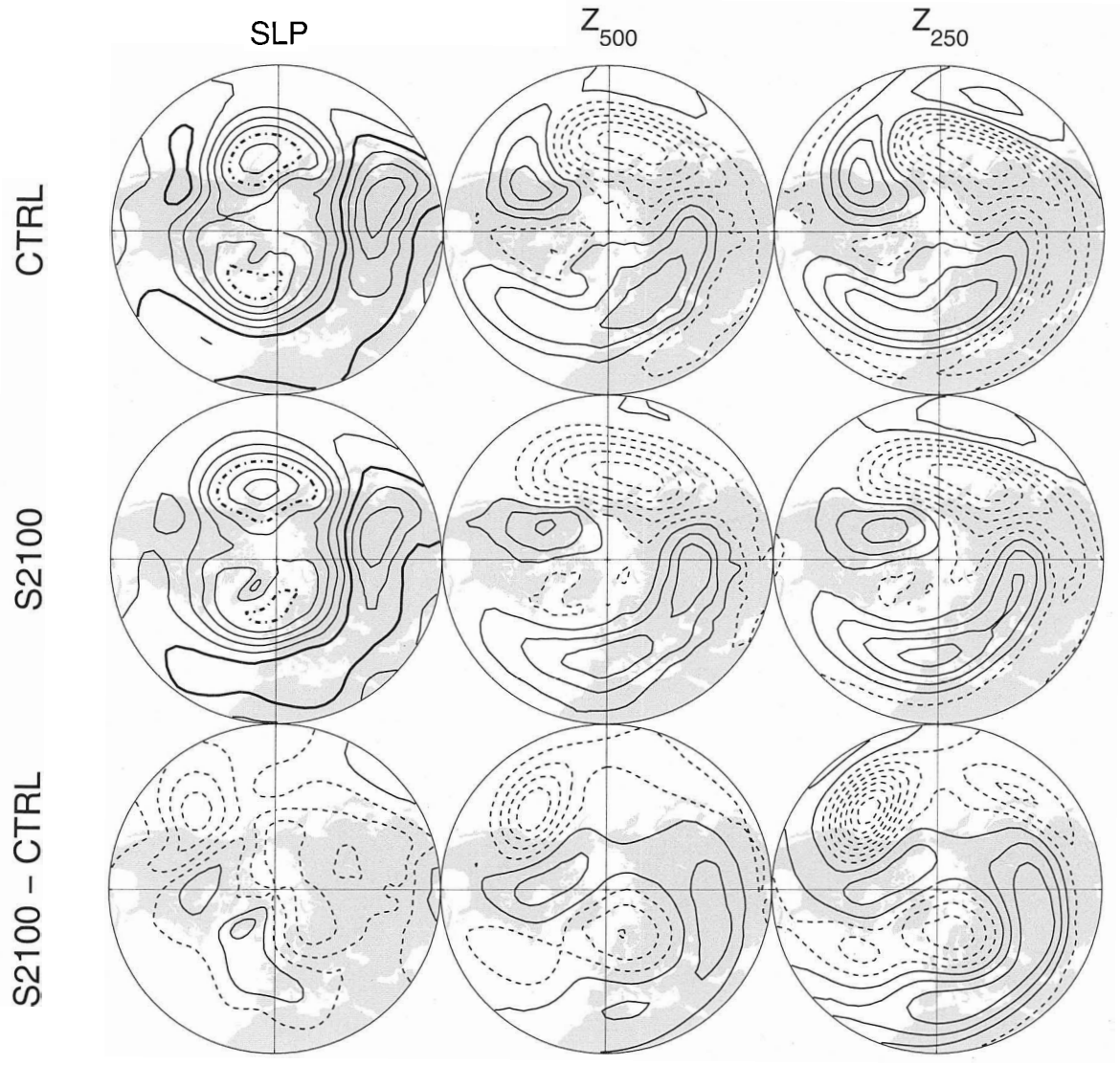

Figure 4.1: Winter-mean SLP (left), Z_{500} (middle) and Z_{250} (right). The upper level fields have had their zonal means removed. Difference fields are shown in the bottom row. The contour interval for SLP is 4 hPa, with 1000 (1020) hPa in bold dash-dot (bold solid). The contour intervals for Z_{500} and Z_{250} are 40 m (..., -60, -20, 20, ...). Contour intervals for the difference maps are 2 hPa (for SLP), 30 m (..., -45, -15, 15, ...) (for Z_{500} and Z_{250}). Positive (negative) values are solid (dashed).

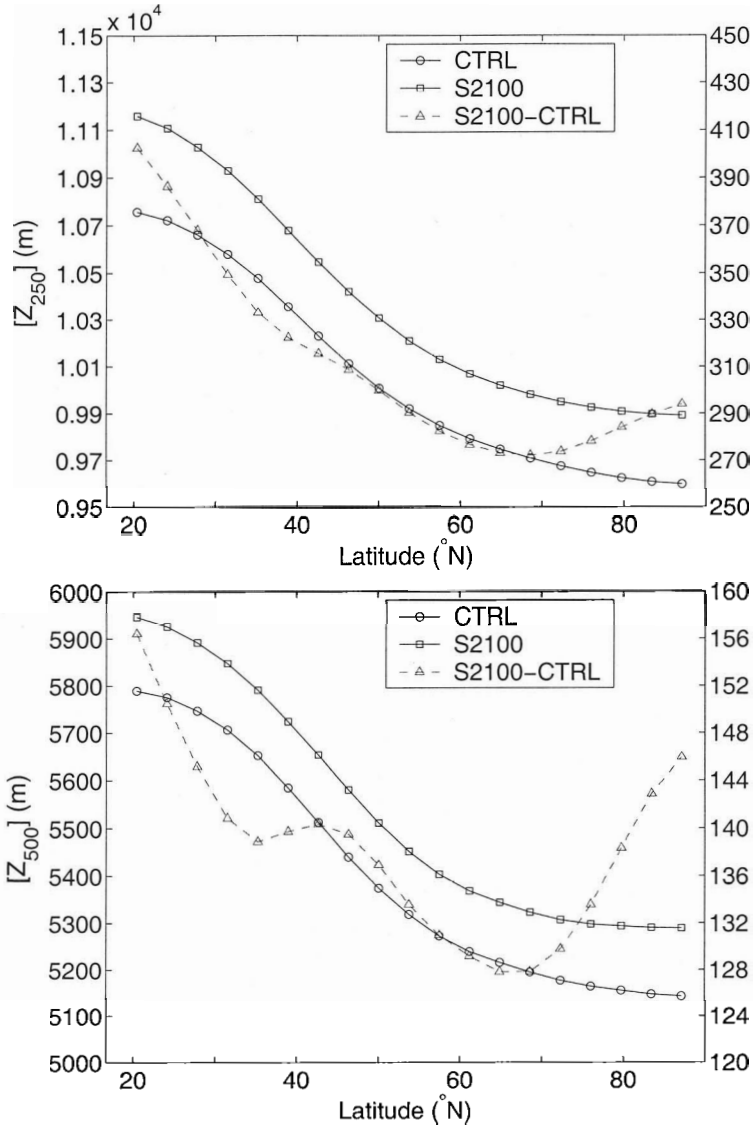

Figure 4.2: Winter-mean zonal-mean Z_{250} (top) and Z_{500} (bottom). The right axis corresponds to the difference curve (triangles).

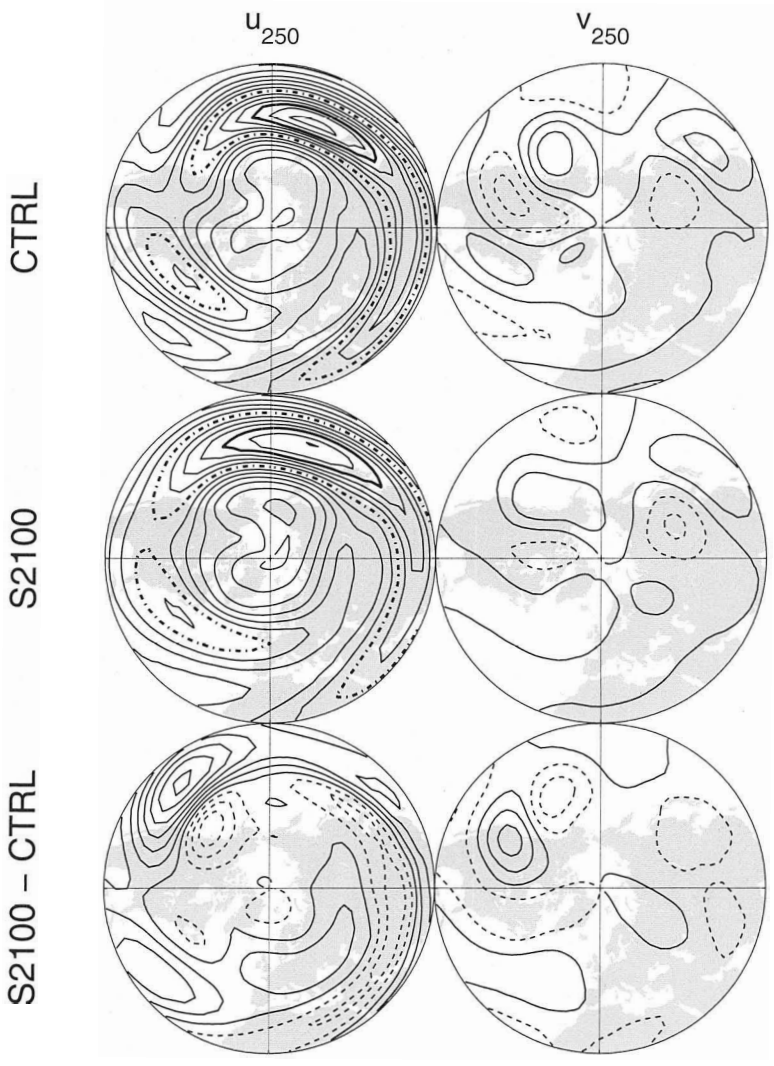

Figure 4.3: Winter-mean u_{250} (left) and v_{250} (right). Contour intervals are 5 m/s (5, 10, 15, ..., for u_{250} with 30 and 50 m/s in bold dashdot and bold solid) and (..., -5, 0, 5, ..., for v_{250}). Contour intervals for the difference maps are 4 m/s (..., -6, -2, 2, ...). Positive (negative) values are solid (dashed).

and there is an elongation over Europe. Figure 4.3 (right) shows the winter-mean meridional wind at 250 hPa and its change under global warming. The meridional wind change is seen as an east-west dipole in the Pacific Northeast (bottom right). This dipole is consistent with the geopotential height changes shown in Figure 4.1.

We turn now to fields of daily variance and their change under global warming. Figure 4.4 shows the winter daily variance for unfiltered (left), 10-day low-pass (middle) and 10-day high-pass (right) SLP data. Under global warming there is reduced daily variability over the North Pacific and Northern North America. This reduction is primarily seen in the high-frequency component. Over Northern Europe and Siberia the daily variance increases under global warming are mainly seen in the low-frequency component. A reduction in low-frequency SLP variability is seen over the west coast of Europe. Figure 4.5 shows that a similar situation prevails for the 500 hPa geopotential height data, with the notable exception that reduced daily variability over the North Pacific and Northern North America is due to low-frequency, rather than high-frequency, change.

Figure 4.6 displays the first three EOFs from the control and stabilization simulations. Under global warming the first EOF (i.e., the AO) becomes less zonal in appearance, primarily owing to the positive anomalies being shifted off the pole and towards the the Siberian Arctic. This is in agreement with Ulbrich and Christoph (1999) who report on a similar response in the ECHAM4+OPYC3 coupled model. The other EOFs are also changed under global warming. Rather than detail these changes to the linear modes any further we now turn to the changes obtained in the leading nonlinear mode. As argued earlier the leading nonlinear mode provides a more fundamental basis for describing the low-frequency variability. By similar reasoning, it is argued that the SLP response to global warming would be better reflected by

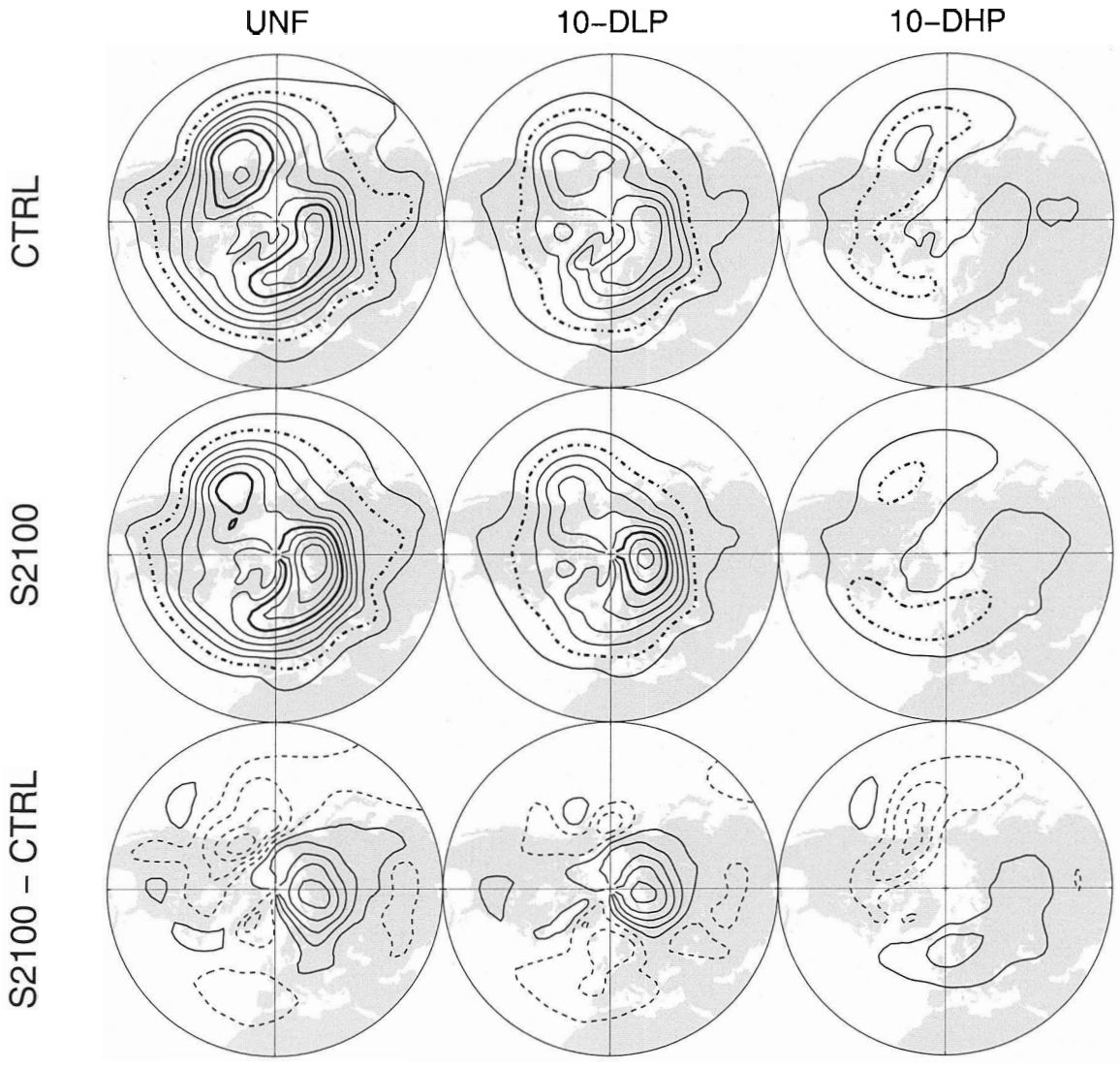

Figure 4.4: Winter daily SLP variance. Differences are shown in the bottom row. Contour interval for the top two panels are 20 hPa^2, with 40 (140) hPa^2 in bold dash-dot (bold solid). Contour interval for the difference is 10 hPa^2 (..., -15, -5, 5, ...), with positive (negative) contours in solid (dashed).

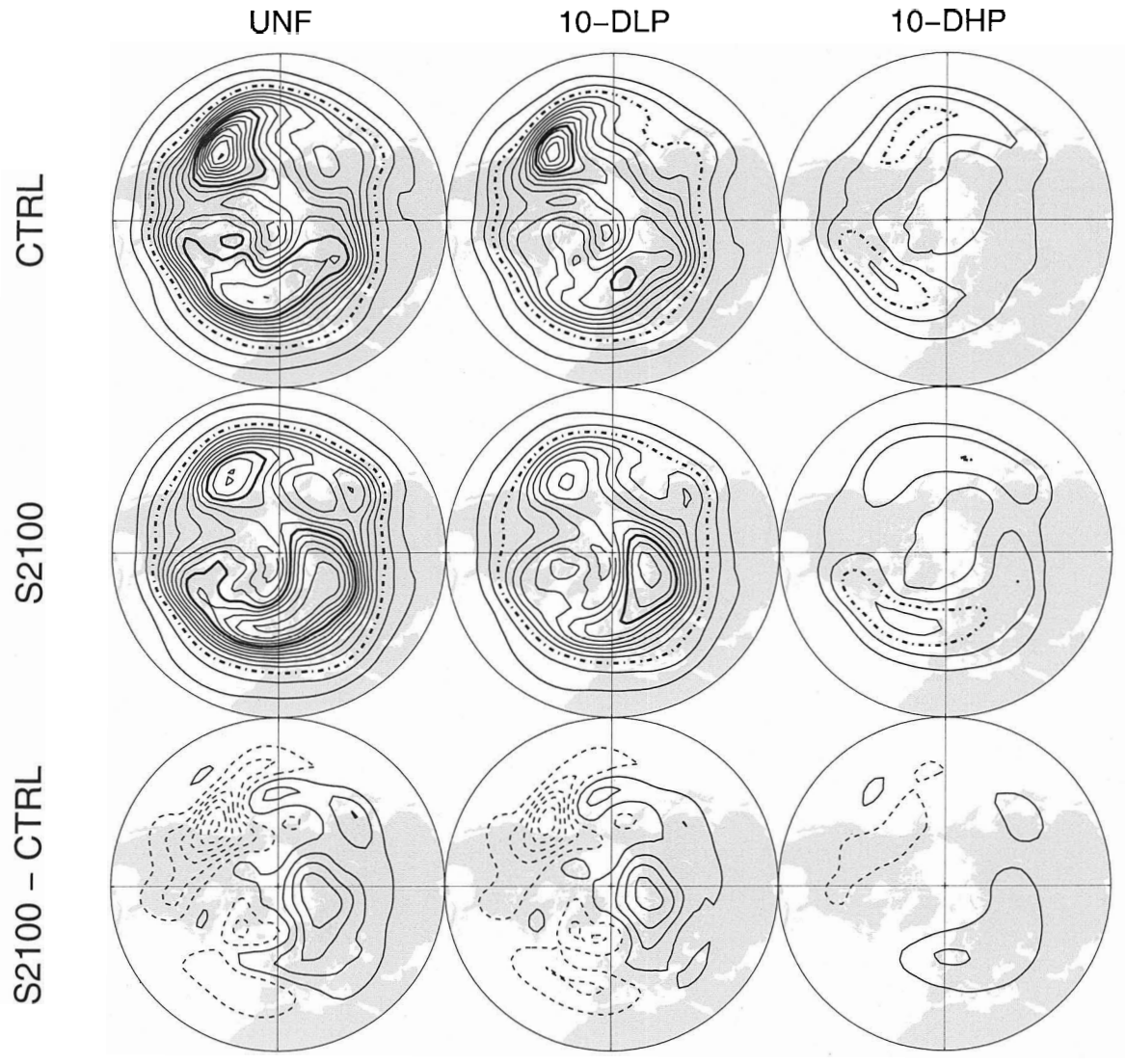

Figure 4.5: As in Figure 4.4 but for Z_{500}. Contour intervals for the top two panels are 1000 m^2, with 3000 (10000) m^2 in bold dash-dot (bold solid). Contour interval for the difference is 2000 m^2 (..., -3000, -1000, 1000, ...), with positive (negative) contours in solid (dashed).

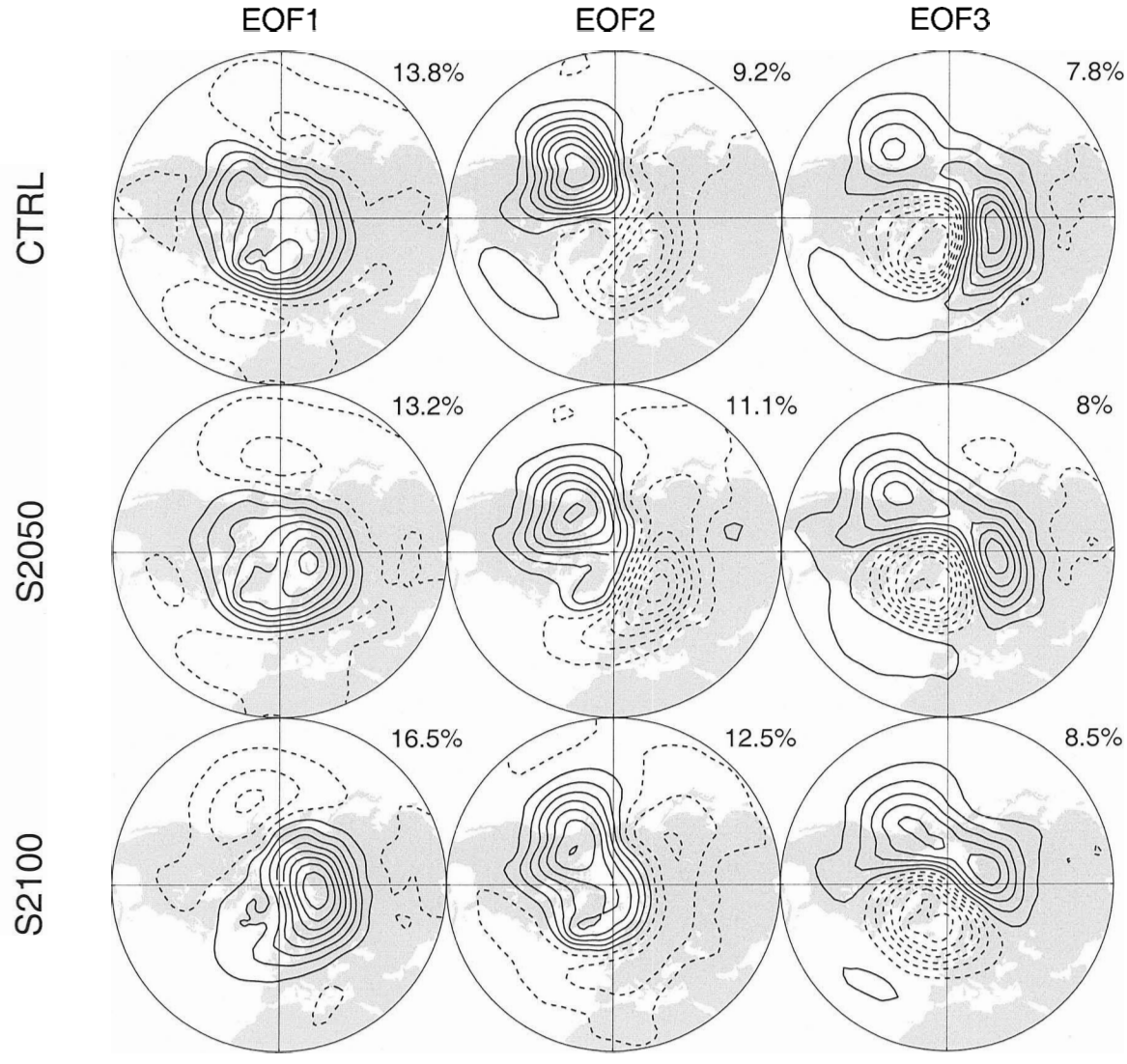

Figure 4.6: Leading linear EOFs. Contour interval is 0.5 (..., -0.75, -0.25, 0.25, ...), with positive (negative) contours in solid (dashed). The number in the upper right corner of each panel indicates the percentage of the total variance explained by each linear PC.

the leading nonlinear mode than by the leading linear mode.

4.2 Leading Nonlinear Modes

Here we consider the effects of global warming on the spatial structure, temporal structure and dynamics of the leading nonlinear modes. Before proceeding we note that all the results reported here have been reproduced using different 100-year samples from the 1000-year control and stabilization simulations so we are confident that they are robust.

4.2.1 Spatial Structure

Figure 4.7 shows the leading nonlinear mode from the control and stabilization simulations. Under global warming we still see a U-shaped approximation and three regimes. However, the spatial structures of the regimes have undergone changes. In particular: 1) For regime R_1 the positive North Pacific center expands eastward towards Greenland. 2) For regime R_2, the negative anomalies expand into northern Europe. 3) For regime R_3, the positive center over Greenland shifts eastward to the central Siberian Arctic. To what extent do these changes express the overall variance change detailed in the previous section? To answer this question we have obtained a variance difference map (not shown due to the strong similarity discussed below) analogous to that in Figure 4.4 (bottom middle) but based on the leading nonlinear approximation. The pattern correlation between this regime-based variance difference map and the total variance difference map exceeds 0.9. Also, the magnitude of the regime-based variance difference map is very close to the magnitude of the total variance change difference map. Put another way, changes in the leading nonlinear

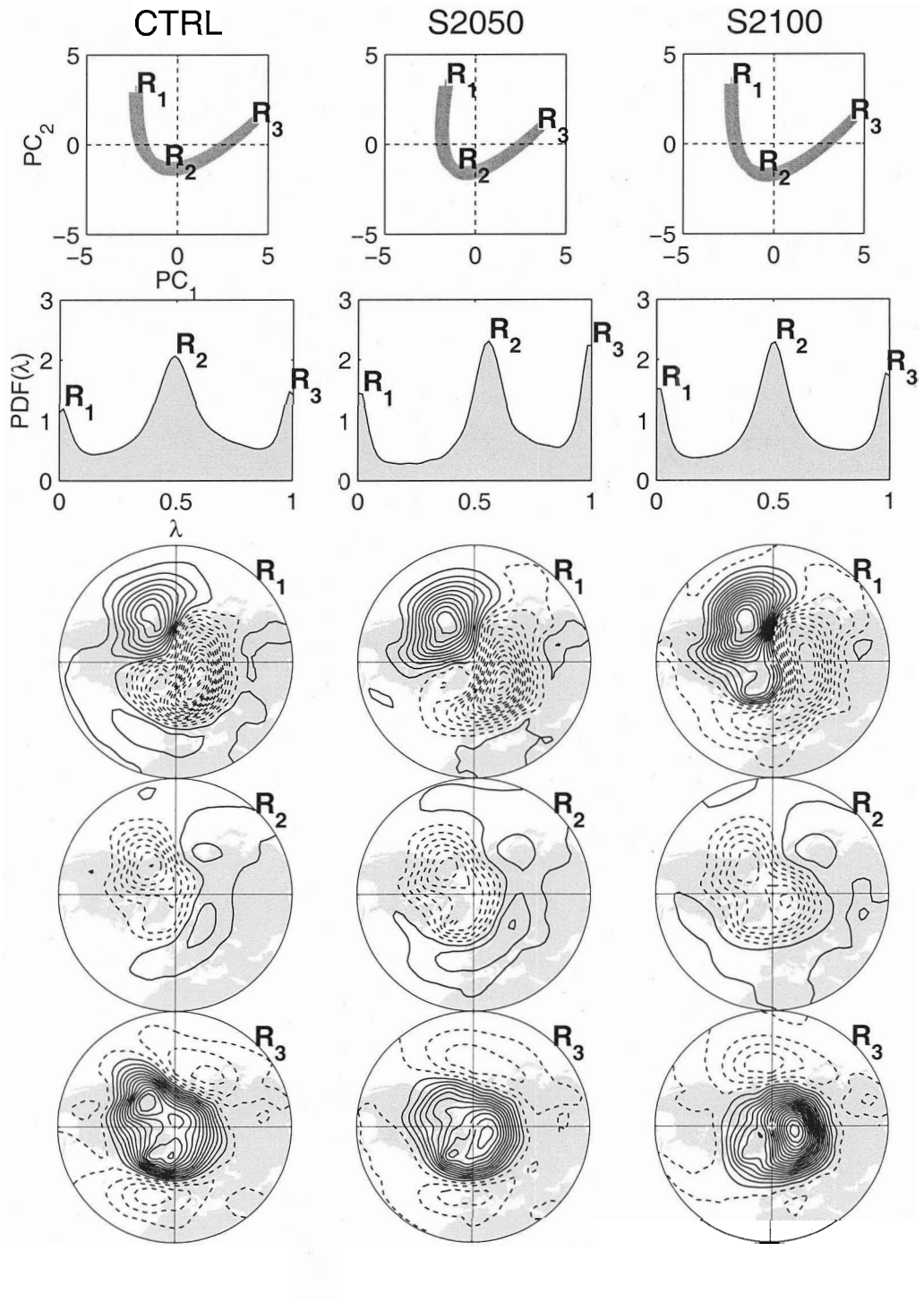

Figure 4.7: Leading nonlinear modes. Note that the axes in the top panels correspond to the PCs from CTRL, S2050 and S2100 runs, respectively. These curves are not significantly changed if projecting into PCs from the control simulation one used instead. Contours as in Figure 3.9.

mode explain more than 80% of the low-frequency variability change. This is in contrast to the leading linear mode which explains only about 49% of the low-frequency variability change. We also note that by rank the R_3, R_2 and R_1 regimes carry most of the low-frequency variability change signal.

4.2.2 Temporal Evolution

Table 4.1 shows the change in percentage and average time spent in each regime. The bracketed quantities are for regime events greater than or equal to 5 days (i.e., long events), and bold typeface indicates significance at the 95% confidence level. For those differences that are significant at the 95% level, the percent time spent increases under global warming given all and just long regime events. The same is true for the average time spent in a given regime as well. In other words, the NH becomes more regime-like under global warming. We note that regime R_3 is especially sensitive to global warming in this sense.

Figures 4.8, 4.9 and 4.10 show the composite onset evolution for regimes R_1, R_2 and R_3, respectively. For the sake of brevity we will not discuss regime break in this Chapter. As discussed in Chapter 3, regime R_1 onset in the control simulation begins with negative anomalies over high latitudes, and generally positive anomalies over mid-latitudes. During onset a positive center over the central North Pacific displaces eastward and amplifies. The stabilization simulations are distinguished by greater amplification of this center. We also see the emergence of positive anomalies extending from the North Pacific center across northern North America to Greenland. Regime R_2 onset in the control simulation involves the development of negative anomalies over high latitudes, which in the stabilization simulations extend further into the Siberian Arctic. Regime R_3 onset in the control simulation involves the development

Table 4.1: Basic statistical differences.

Exp.	Regime	Change in percent time spent	Change in average time spent (days)
		All (Long)	All (Long)
S2050-CTRL	R_1	**+1.5 (+1.2)**	-0.3 (-0.3)
	R_2	+0.1 (+0.7)	+0.1 (-0.1)
	R_3	**+7.2 (+6.7)**	**+0.9 (+1.5)**
S2100-CTRL	R_1	**+2.4 (+2.3)**	+0.5 (**+0.8**)
	R_2	+0.4 (**+1.3**)	**+0.6 (+0.8)**
	R_3	**+3.0 (+3.1)**	**+1.9 (+2.5)**

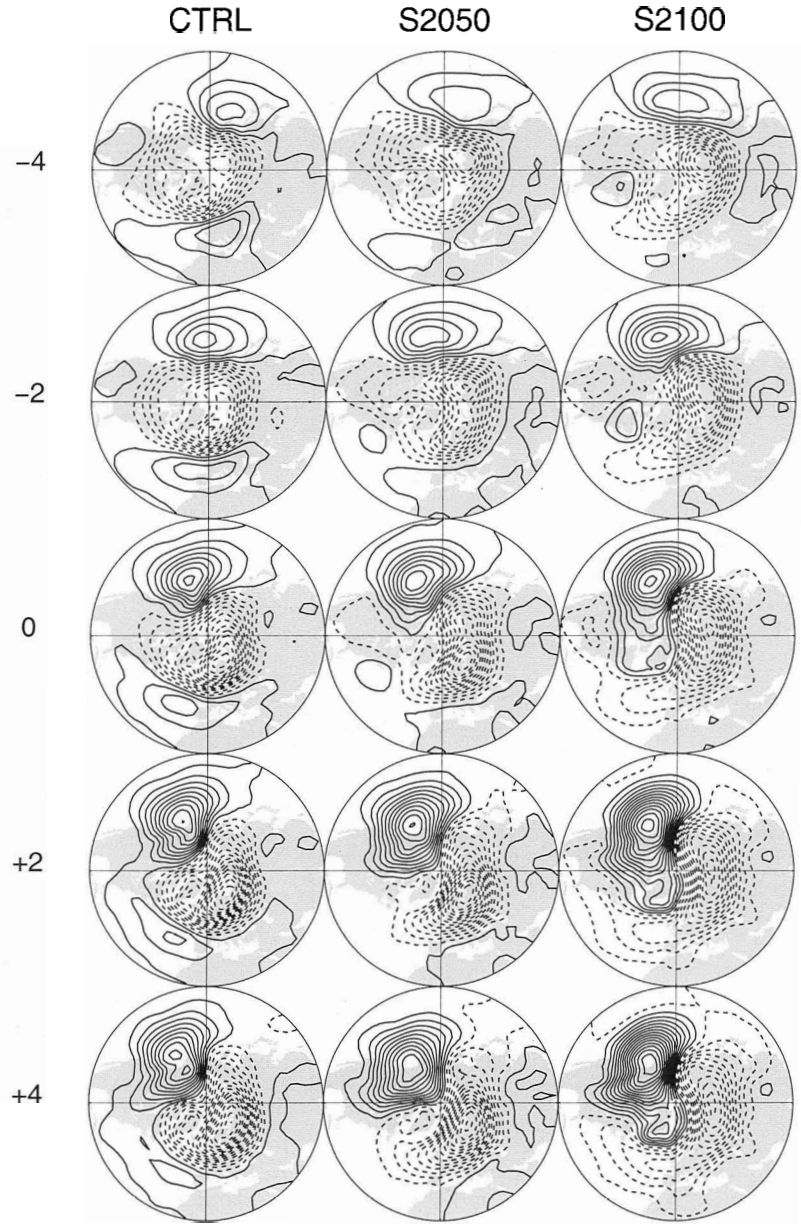

Figure 4.8: Regime R_1 composite onset. Contour interval: 1.0 hPa (..., -1.5, -0.5, 0.5, ...). Positive (negative) values are solid (dashed).

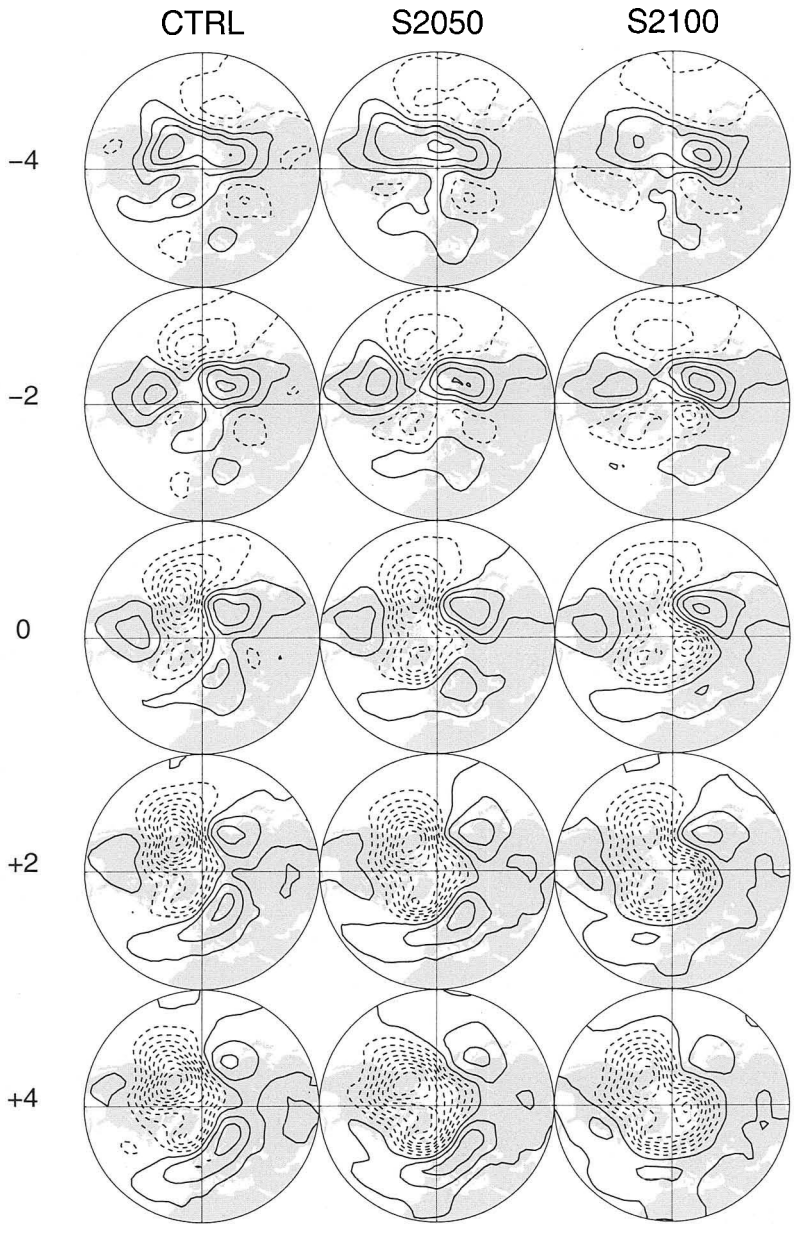

Figure 4.9: As in Figure 4.8, but for regime R_2

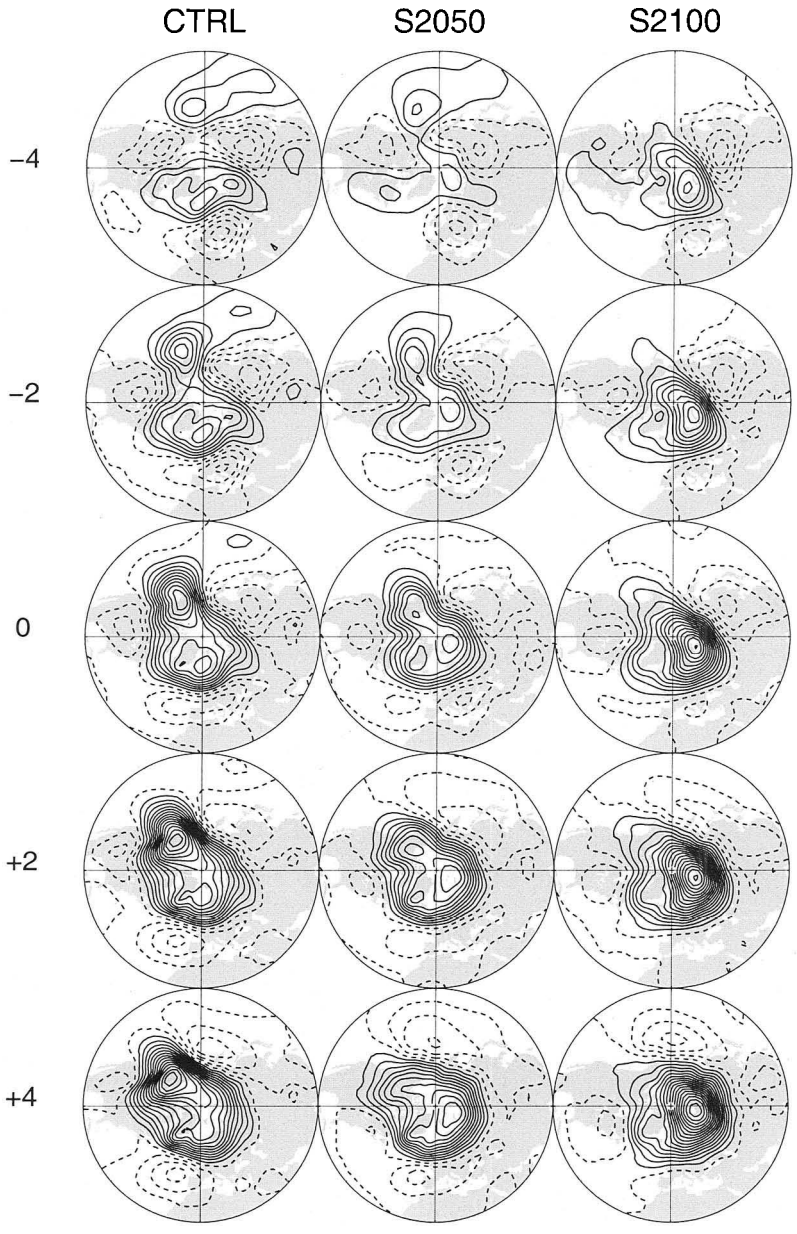

Figure 4.10: As in Figure 4.8, but for regime R_3.

of positive anomalies over high latitudes, which in the stabilization simulations show an eastward shift to Northern Siberia.

It is clear that global warming affects regime evolution. In particular we note changes in the regime residence times and spatial structures although the regime structures remain recognizable. It appears then that these results support a qualified version of the hypothesis of Palmer (1999), who proposed that the residence frequencies rather than the spatial structures of atmospheric regimes may change significantly under global warming. The qualification lies in two aspects: 1) changes in residence times; and 2) changes in spatial structures. In our results, although the peaks of PDF(λ) in Figure 4.7 tend to increase under enhanced GHGA forcing, they don't change drastically as in Palmer (1999, his Figure 5a), in which observed SST forcing corresponding to El Niño and La Niña is used. It appears that in our case the number of regime events decreases while the regime residence time increases under global warming. As to the changes in spatial structures, it appears that they change in their detailed structures, while retaining their basic identities.

4.2.3 Dynamics

As in Chapter 3 we explore the low- and high-frequency dynamics. For the sake of brevity we consider only regime R_1 and R_3 onset.

Low-Frequency Dynamics

Figures 4.11 and 4.12 display $\mathbf{W}_h$ (arrows) and Z_{250} anomalies (contours) for regimes R_1 and R_3, respectively. Consider regime R_1. In the control simulation the North Pacific center migrates, amplifies and emanates Rossby wave energy in the downstream direction. Under global warming the North Pacific center shows even

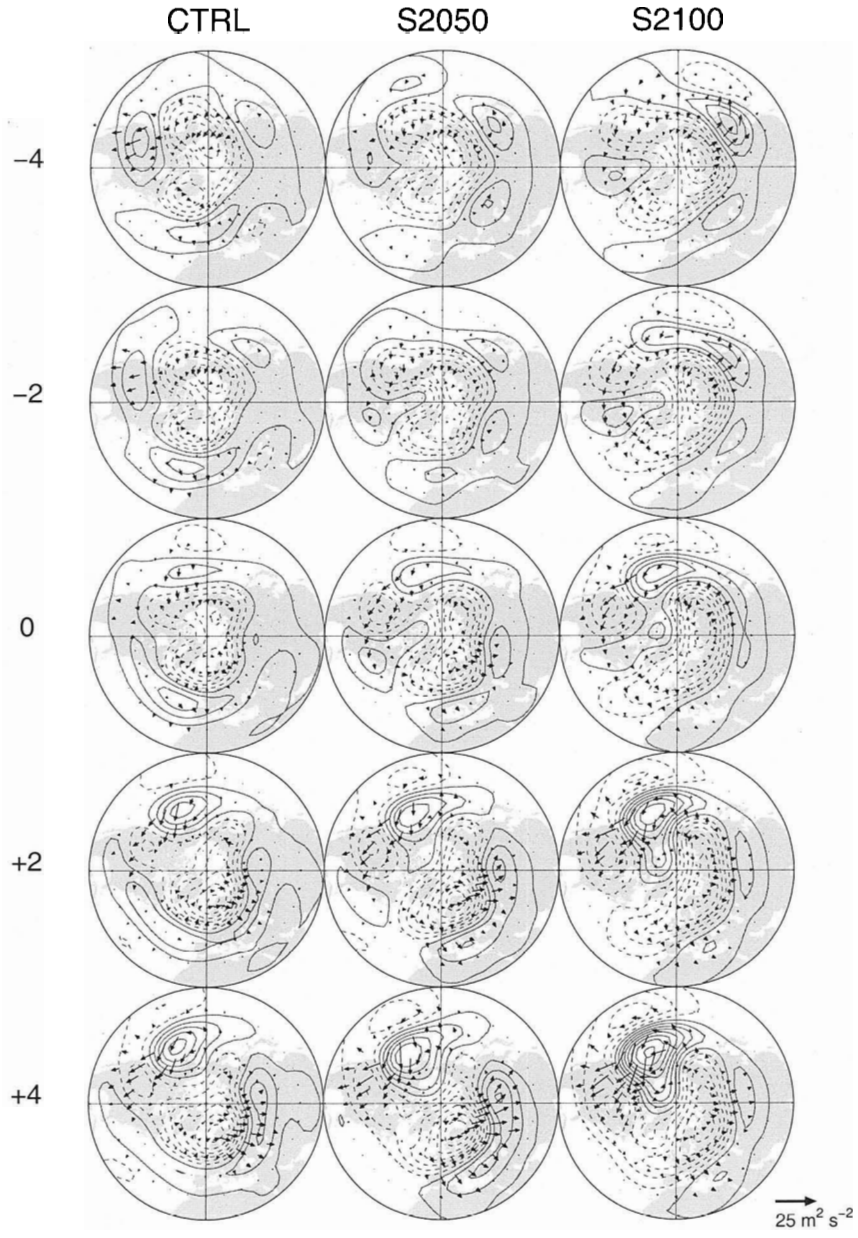

Figure 4.11: Regime R_1 composite onset evolution of $\mathbf{W}_h$ (arrows) and Z_{250} anomalies (contours). Contour interval: 20 m (..., -30, -10, 10, ...). Positive (negative) contours are solid (dashed). Other details as in Figure 3.19.

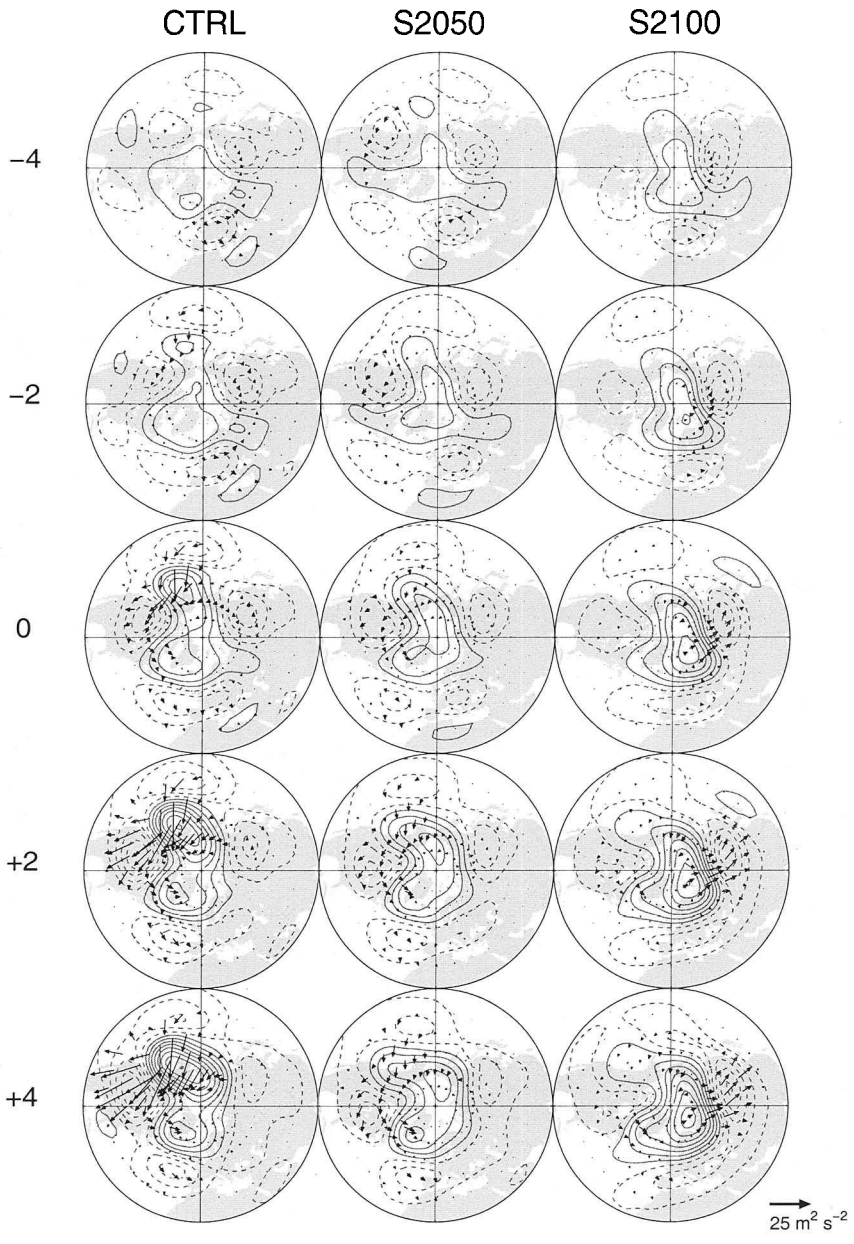

Figure 4.12: As in Figure 4.11, but for regime R_3.

more amplification and downstream wave energy propagation. In particular, in the S2100 simulation we see enhanced negative height anomalies over North America, which is likely due to enhanced wave energy absorption there (not shown).

Now consider regime R_3. Particularly dramatic changes under global warming are seen here. In the control simulation the main primary center of action is over Alaska where downstream energy propagation and absorption appears responsible for a secondary center of negative anomalies over North America. By contrast, in the S2100 simulation the main primary center of action is found over Northern Eurasia where south-eastward energy propagation and absorption (not shown) is associated with the development of negative anomalies over Mongolia.

To conclude this subsection we note that the low-frequency dynamical response to global warming ranges from a simple amplification or attenuation of the control pattern of Rossby wave energy dispersion (as in regime R_1) to a complete spatial reorganization (as in regime R_3).

High-Frequency Dynamics

Figure 4.13 shows the winter-mean A^H (i.e., mean synoptic eddy amplitude). Under global warming the North Atlantic storm track shifts north-eastward to the west coast of Europe, while the Pacific storm track weakens and shifts equatorward. These changes are consistent with the high-frequency plots shown in Figures 4.4 and 4.5. We also note that these changes in the high-frequency eddies approximately mirror the changes in the 250 hPa zonal wind (cf. Figure 4.3). That is, the amplitude of the high-frequency eddies increase (decrease) where the climatological zonal winds increase (decrease) with global warming.

Figures 4.14 and 4.15 show the composite anomalous A^H (black contours) and

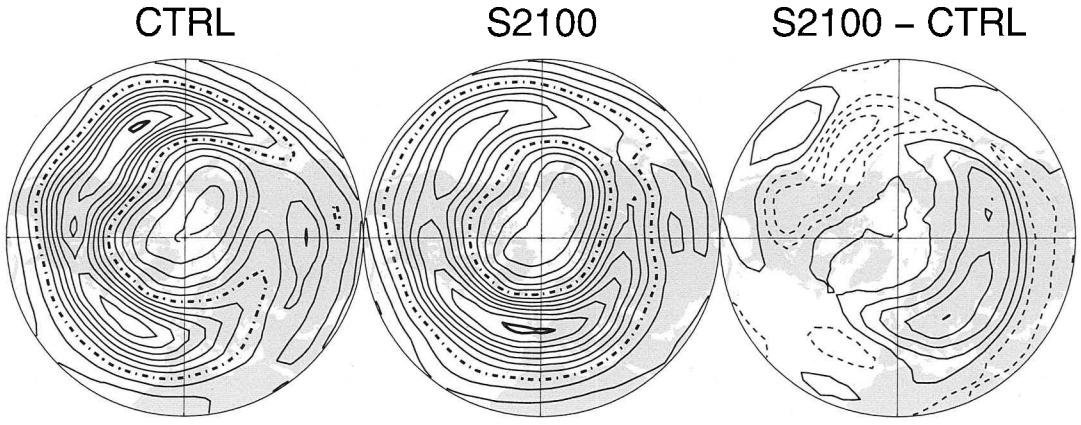

Figure 4.13: Winter-mean A^H. Contour intervals are 1 m/s for mean A^H, with 10 (17) m/s contour in bold dashdot (bold solid), and 1 m/s (..., -1.5, -0.5, 0.5, ...) for the difference, with positive (negative) values in solid (dashed).

Z_{250} (gray contours) for regimes R_1 and R_3, respectively. Regime R_1 in the control simulation is characterized by the development of positive height anomalies in the Pacific Northwest. As discussed in Chapter 3 these anomalies steer the synoptic eddies northward, causing enhanced eddy activity to the north. Under global warming an even more developed North Pacific center carries synoptic disturbances even further northward (i.e., well into the Arctic). In the stabilization simulations we note, in particular, reduced synoptic eddy activity ranging from the west coast of North America clear across the Atlantic corresponding to the reduced westerly region. In the case of regime R_3 we recall that global warming shifts the center of positive anomalies over Greenland eastward to Northern Siberia. In this case the reduced westerlies over Eurasia produce suppressed synoptic eddy activity from the west coast of Europe through to the east coast of Asia.

It is clear that CO_2-induced change in regime circulation can affect a change in the synoptic environment. We now assess the corresponding change in the high-frequency

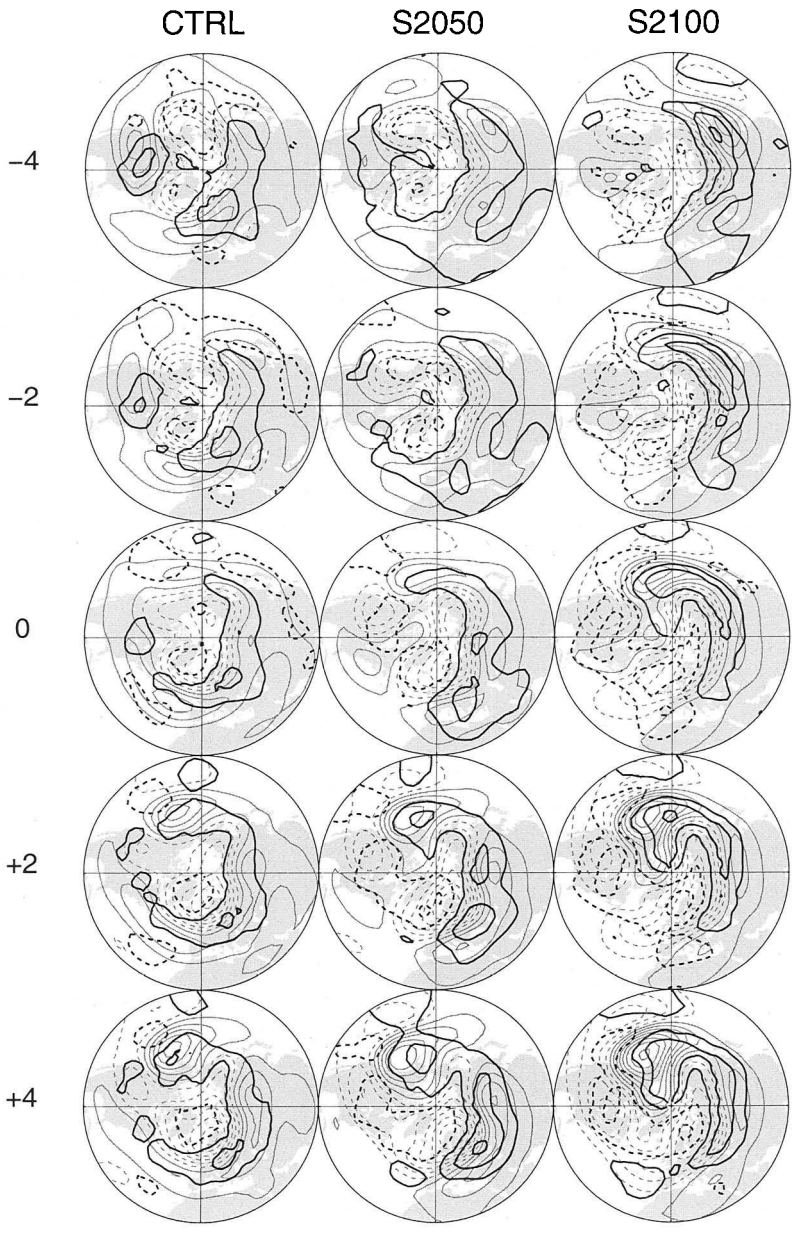

Figure 4.14: R_1 composite onset evolution of anomalous A^H (black contours) and anomalous Z_{250} (gray contours). Contour intervals for Z_{250} anomalies are 20 m (..., -30, -10, 10, ...), for anomalous A^H are 1.0 m/s (..., -1.5, -0.5, 0.5, ...). Positive (negative) contours are solid (dashed).

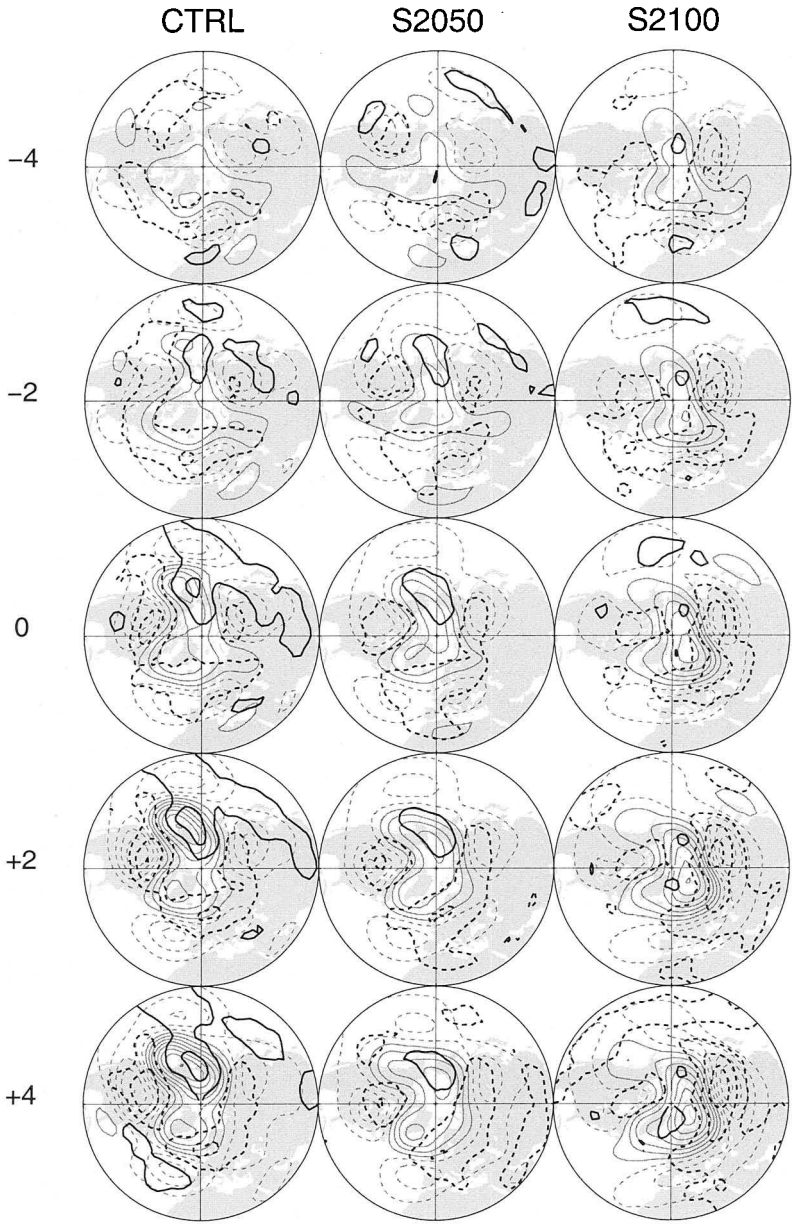

Figure 4.15: As in Figure 4.14, but for regime R_3.

transient eddy feedback. As in Chapter 3 we compute the contribution of the high-frequency transient eddies to the low-pass filtered Z_{250} time-tendency, i.e., $\left(\partial\overline{Z}/\partial t\right)^H$. Figure 4.16 displays winter-mean $\left(\partial\overline{Z}/\partial t\right)^H$. Generally speaking the synoptic eddies in the control simulation produce negative height tendencies (i.e., cyclonic forcing) at high latitudes, and positive height tendencies (i.e., anti-cyclonic forcing) at lower latitudes. Under global warming the North Pacific cyclonic forcing weakens (i.e., becoming less cyclonic) and the North Atlantic cyclonic forcing strengthens (i.e., becoming more cyclonic) and extends eastward.

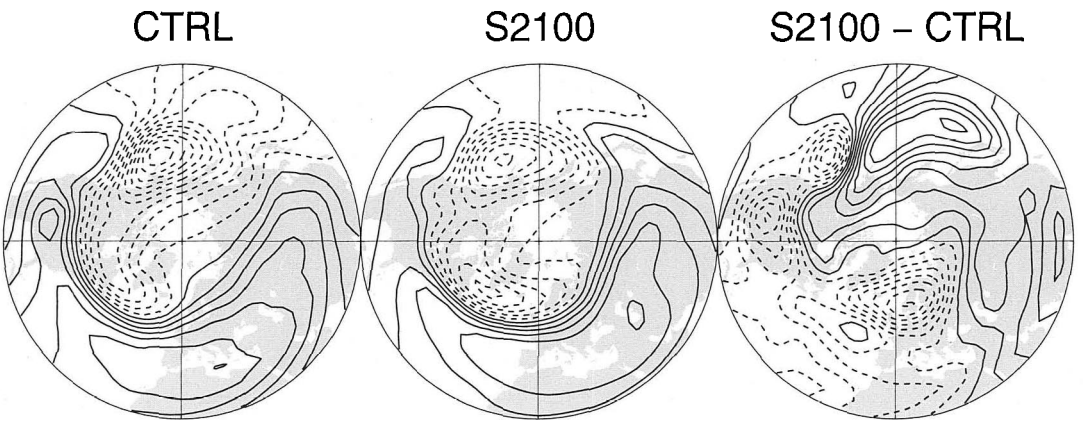

Figure 4.16: Winter-mean $\left(\partial\overline{Z}/\partial t\right)^H$ at 250 hPa. (a): control and (b): S2100 simulations. Contour interval: 5.0 (..., -7.5, -2.5, 2.5, ...) $\times 10^{-5}$ m/s. Positive (negative) contours are solid (dashed).

Figures 4.17 and 4.18 show the composite onset evolution of anomalous $\left(\partial\overline{Z}/\partial t\right)^H$ for regimes R_1 and R_3, respectively. Consider regime R_1. The particular feature that stands out in the S2100 simulation is the region of positive $\left(\partial\overline{Z}/\partial t\right)^H$ extending from the North Pacific across northern North America. So it appears that the syn-

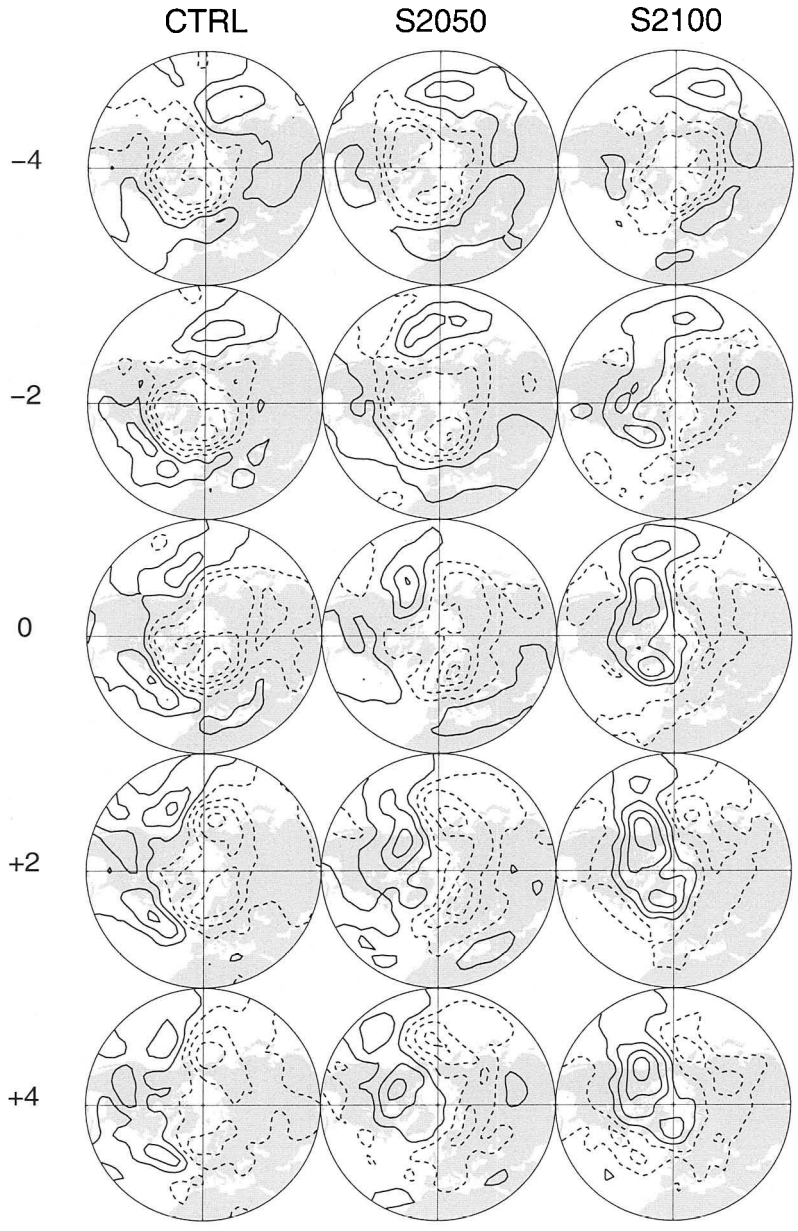

Figure 4.17: Composite onset evolution of anomalous $\left(\partial\overline{Z}/\partial t\right)^{H}$ for regime R_1 from control, S2050 and S2100 simulations. Contour interval is 5.0 m/day (..., -7.5, -2.5, 2.5, ...). Positive (negative) contours are solid (dashed).

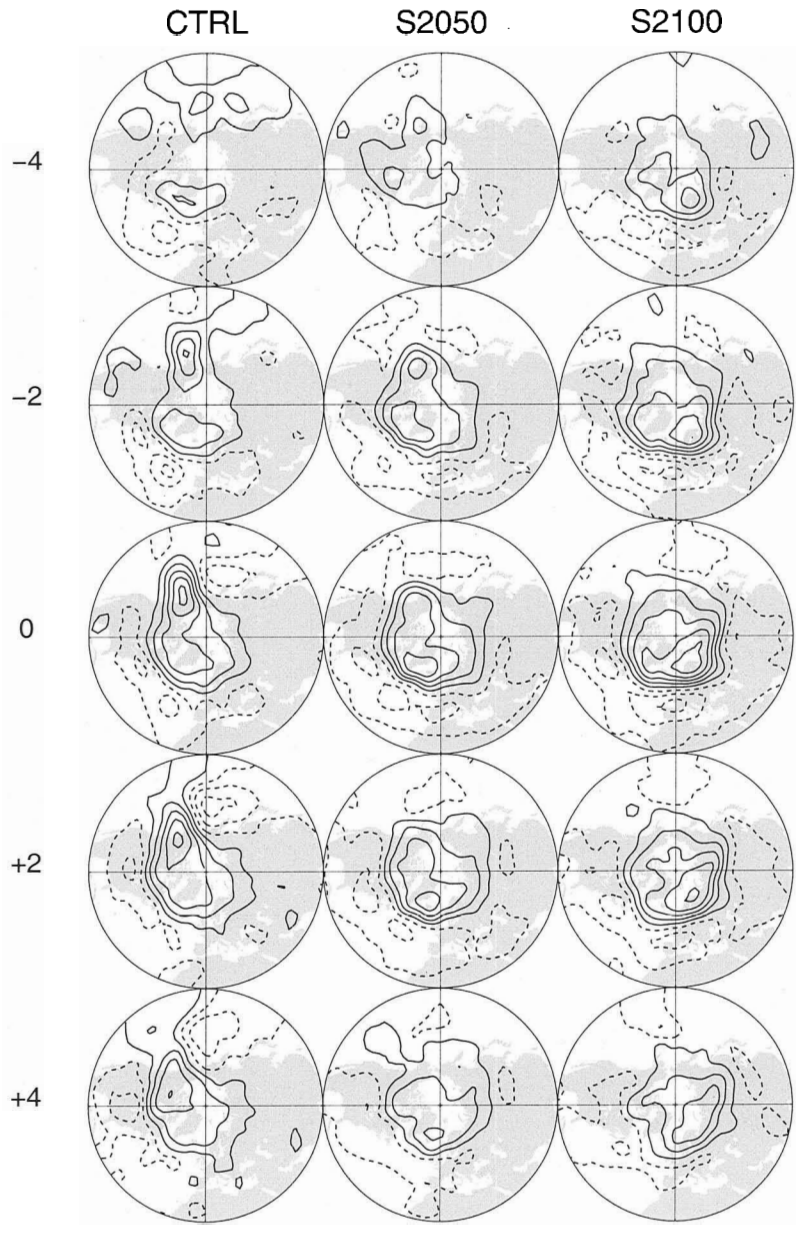

Figure 4.18: As in Figure 4.17, but for regime R_3.

optic eddies tend to reinforce the positive height anomalies seen there. Now consider regime R_3. In the control simulation we see that regions of positive tendency are generally associated with positive height anomalies, and negative with negative. This is indicative of a positive feedback from the synoptic eddies to the primary regime circulation structures. This situation prevails under global warming but with the centers of action shifted eastward. Figures 4.19 and 4.20 show the integrated effect of the synoptic eddy forcing on regimes R_1 and R_3, respectively. Overall, we conclude that despite changes in the magnitude and position of the regime anomalies under global warming the basic dynamical picture is as in the control simulation.

4.3 Summary

Under global warming the winter-mean circulation and day-to-day variance of SLP change appreciably. The leading nonlinear mode under global warming still describes three regime states, however the percent of time, and the amount of time, spent in the regimes increases. Simply put, the atmosphere becomes more regime-like under global warming. Aside from these changes in regime residence time there are also changes in the spatial and dynamical signals of the regimes, although they remain recognizable. These results are consistent with a qualified version of Palmer's hypothesis in which the regime structures change along with residence times under global warming although not so much that their identities are lost. It is also shown that the leading nonlinear mode carries a much larger fraction of the overall climate change signal than is the case with the leading linear mode. Finally, it is noted that most of the change in the leading nonlinear mode is associated with regime R_3 which dominates variability in the North Atlantic and European regions. The change in spatial structure of regime R_3 may be related to the retreat of the sea ice extent under global

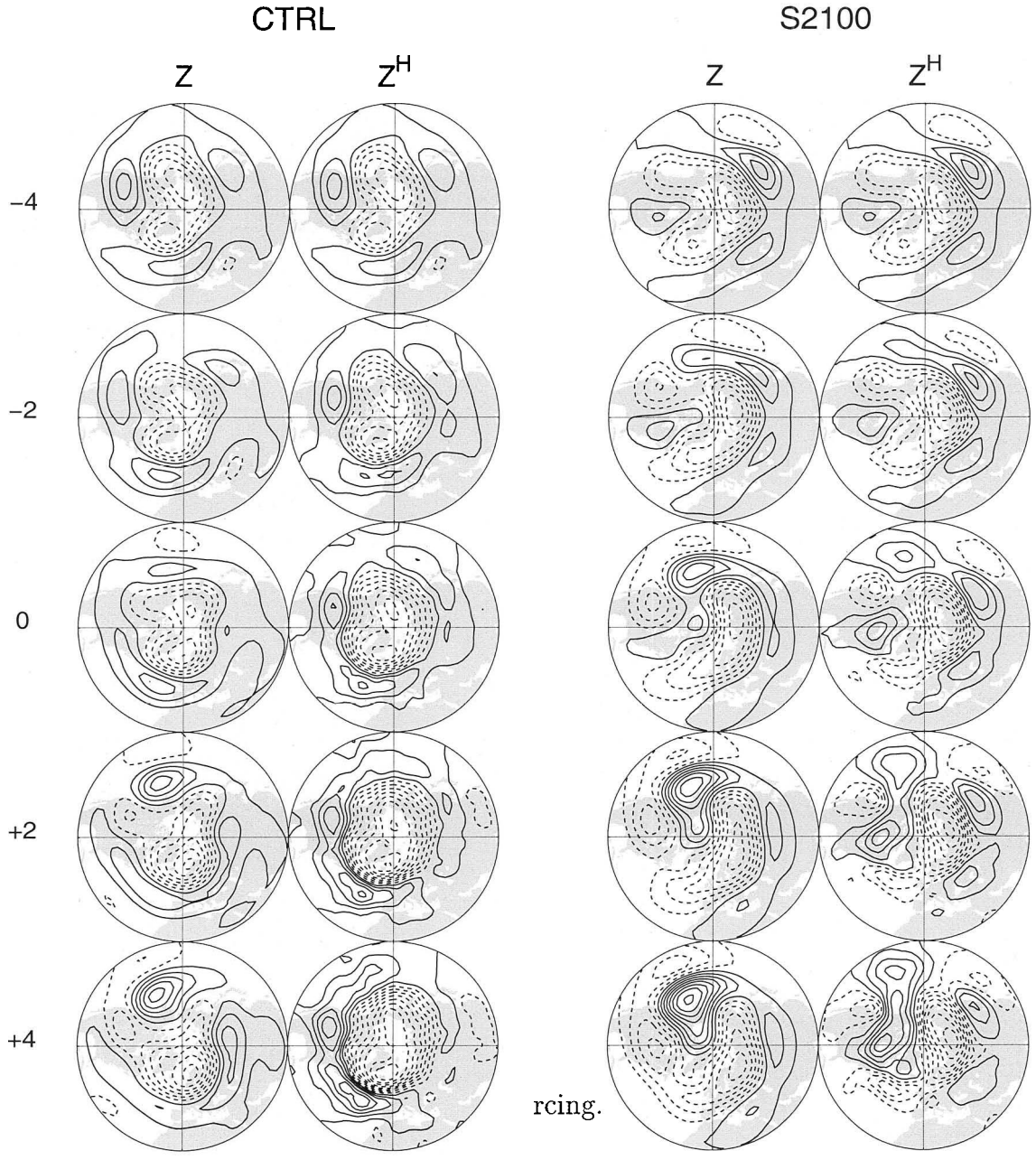

rcing.

Figure 4.19: Regime R_1 composite onset evolution of Z_{250} anomalies (the first and third columns) and hypothetical evolution of Z_{250} anomalies assuming synoptic eddy forcing is acting alone (the second and fourth columns). Contour interval: 20 m (..., -30, -10, 10, ...). Positive (negative) contours are solid (dashed).

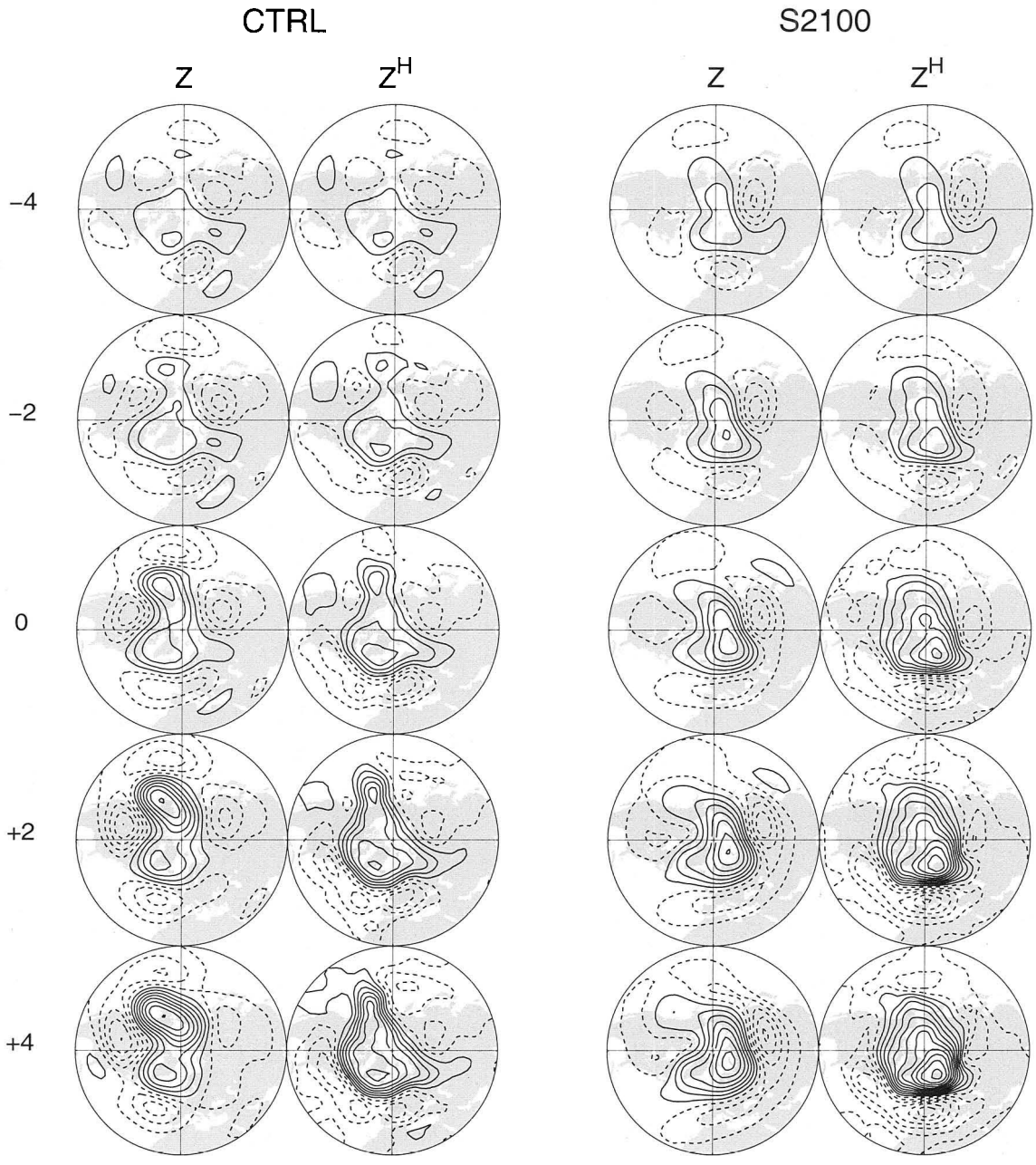

Figure 4.20: As in Figure 4.19, but for regime R_3.

warming (e.g., Lu and Greatbatch 2002; Jung et al. 2003)

Chapter 5

Nonlinear Variability and Time Filtering

In this chapter we attempt to reconcile the results from two earlier studies on nonlinear atmospheric variability. Monahan et al. (2000c) applied NLPCA to monthly mean SLP from a 1000-year control simulation of CGCM1. Two regimes were found in that study. More recently, Monahan et al. (2001; 2003) applied NLPCA to 10-day low-pass filtered Z_{500} from 41-years of NCEP reanalyses. Three regimes were found in those studies. Why do these studies differ in the number of regimes? The possibilities are at least three-fold: 1) simulated versus observed data; 2) SLP versus Z_{500} data and/or 3) monthly-averaged versus 10-day low-pass filtered data. In Chapter 3 we applied NLPCA to simulated and observed 10-day low-pass filtered SLP and found three very similar regimes in each case. The same is true for simulated and observed 10-day low-pass filtered Z_{500} (not shown). These results allow us to discount the first two of the above possibilities, and focus on the third.

Figure 5.1 (top) displays the leading observed NLPCA approximations given 10-,

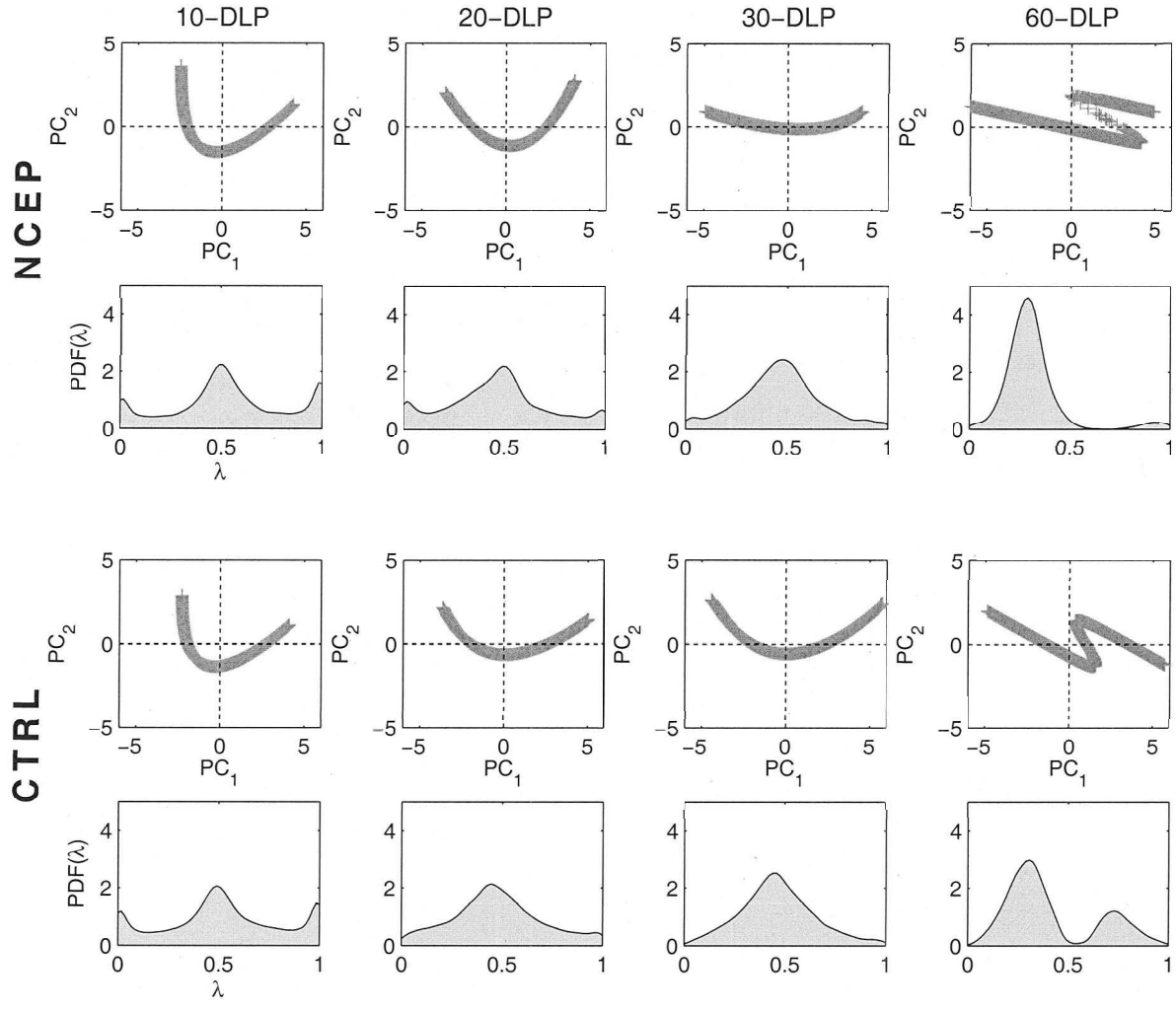

Figure 5.1: Leading nonlinear modes for various low-pass cut-offs (in days).

20-, 30- and 60-day low-pass filtered SLP data. As discussed extensively in Chapter 3, 10-day low-pass filtered SLP exhibits a U-shaped approximation with a tri-modal λ distribution. As the cut-off period of the time filter increases the U-shaped approximation flattens out and then eventually overturns to form a Z-shaped approximation with a bi-modal λ distribution. The Z-shaped approximation reflects both: 1) a large population of points with its major axis tilted slightly downward with respect to the PC_1 axis and 2) a small, but distinguished, population of points in the upper-right quadrant of the PC_1 and PC_2 space. Figure 5.1 (bottom) shows that this sensitivity to time-filtering is reproduced in the CTRL simulation. This behavior is seen also when using observed and simulated Z_{500} rather than SLP (not shown). So it is that Monahan et al. (2001; 2003) found three regimes using 10-day low-pass filtered data and Monahan et al. (2000c) found two regimes using monthly mean (corresponding roughly to 60-day low-pass filtered) data. In short, the characterization of nonlinear atmospheric variability is strongly dependent upon the time-filtering applied to the data.

To help understand the time-filtering sensitivity Figure 5.2 shows estimates of the regime residence time distribution for observed (left) and simulated (right) 10-day low-pass filtered SLP. These distributions are approximately exponential (thick curves) with characteristic e-folding times of about 8 days, i.e., $p(T) \approx \tau^{-1} \exp(-T/\tau)$ where $\tau \approx 8$ days. Similar histograms (not shown) are found for each regime considered individually. Table 5.1 shows the e-folding times on a regime-by-regime basis. It may be that smoothing over time-scales substantially longer than this intrinsic time-scale gives a distorted view of the low-frequency variability. We will explore this possibility further using a simple stochastic model.

The trajectory $\mathbf{s}(t) = (x(t), y(t))$ of a massless or overdamped particle moving

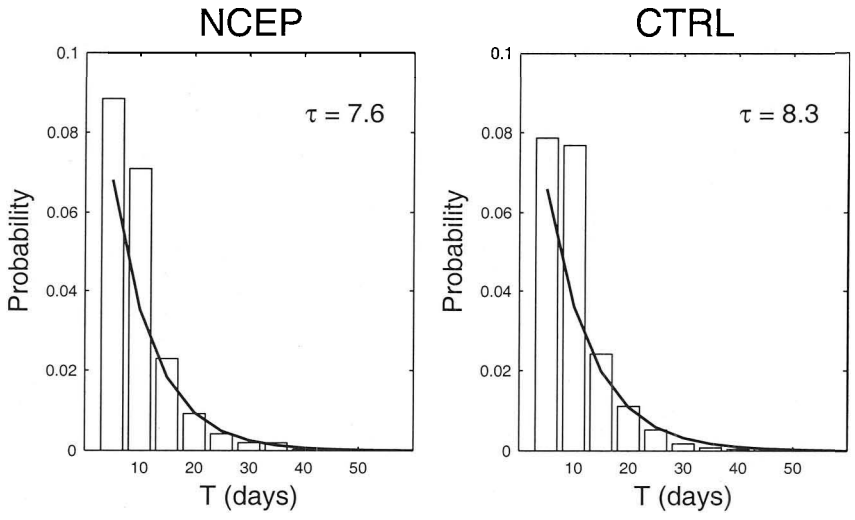

Figure 5.2: Histogram estimates of regime residence times for 10-day low-pass filtered SLP. The thick curve is the best fit to an exponential distribution with an e-folding time, τ, given in the upper right.

Table 5.1: Estimated e-folding time (in days) for each regime.

	R_1	R_2	R_3
NCEP	9.3	6.9	8.2
CTRL	9.2	7.6	9.7

randomly in a potential flow $U(x, y)$ can be given by:

$$\dot{\mathbf{s}} = -\nabla U + \boldsymbol{\varepsilon}. \tag{5.1}$$

To emulate three regimes we consider a three well potential given by

$$U(x,y) = \frac{a}{2}(x^2 + y^2) - \frac{1}{2}\sum_{i=1}^{3} b_i \; exp\Big(- \frac{(x - x_{0i})^2 + (y - y_{0i})^2}{c_i}\Big), \tag{5.2}$$

where b_i, (x_{0i}, y_{0i}) and c_i are parameters representing the depth, position and width of the wells in the potential, respectively. Figure 5.3 shows $U - a(x^2 + y^2)/2$ given the parameters: $a = 1$, $\mathbf{b} = (10, 10, 10)$, $\mathbf{c} = (2.5, 2.5, 2.5)$, $\mathbf{x}_0 = (-2, 0, 1.5)$ and $\mathbf{y}_0 = (1, -1.25, 1)$. Note that the wells in the potential are slightly asymmetric. Randomness is represented by a red-noise function $\boldsymbol{\varepsilon}$ obtained by solving

$$\dot{\boldsymbol{\varepsilon}} = -\frac{1}{\tau}\boldsymbol{\varepsilon} + \frac{\sigma}{\tau}\dot{\mathbf{W}}, \tag{5.3}$$

where τ and σ are the auto-correlation e-folding time and strength of the noise and $\dot{\mathbf{W}} = (\dot{W}_1, \dot{W}_2)$ is a white noise forcing function. In what follows we set: τ=0.4, and σ=2.5. Finally, equations (5.1) and (5.3) are integrated numerically using a forward-Euler scheme (Kloeden and Platen 1992) for 800 time steps, with one time step equivalent to 10 days.

Figure 5.4 (top left) displays the leading NLPCA approximation superimposed on the joint PDF distribution (black contours) of the two time series, $x(t)$ and $y(t)$, for unsmoothed (left), 10-day low-pass (middle) and 60-day low-pass (right) time series. Figure 5.4 (bottom left) shows estimates of the PDF of λ. In the unsmoothed case we see a U-shaped approximation passing through the center of the three wells. We note that the well locations coincide with the peaks of the λ distribution, which is shown in Figure 5.5 for the whole integration period. From Figure 5.5, the unfiltered λ shows longer timescales in the three shaded regions associated with the three

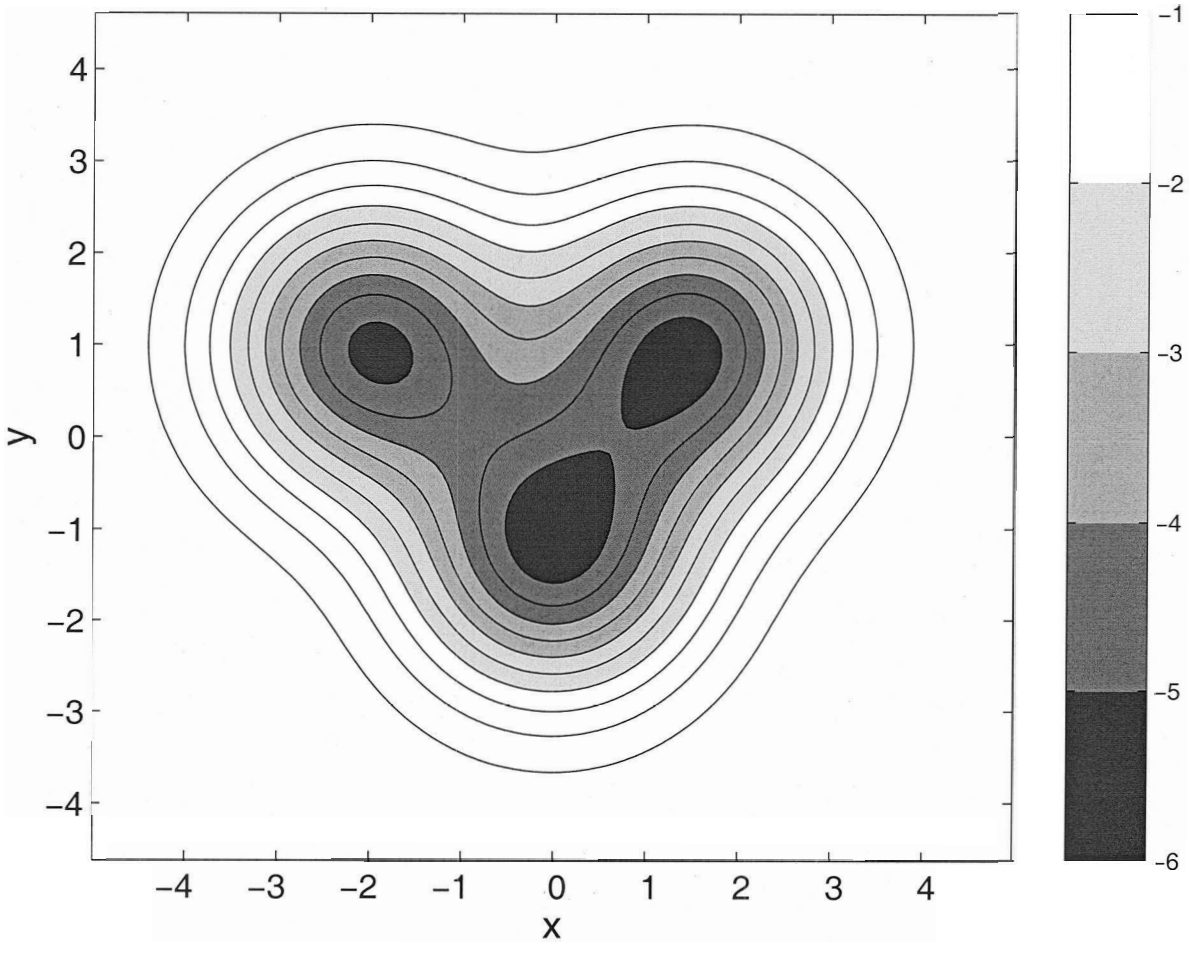

Figure 5.3: Distribution of potential $U - a(x^2 + y^2)/2$. Contour interval: 0.5.

wells. It also shows shorter timescales corresponding to fast transitions between the wells. The λ distribution from this simple model well characterizes the recurrent and persistent features presented in the atmospheric regimes shown in Figure 3.7. By fitting to an exponential distribution we also estimate the average residence time in the unsmoothed case to be approximately 7 days.

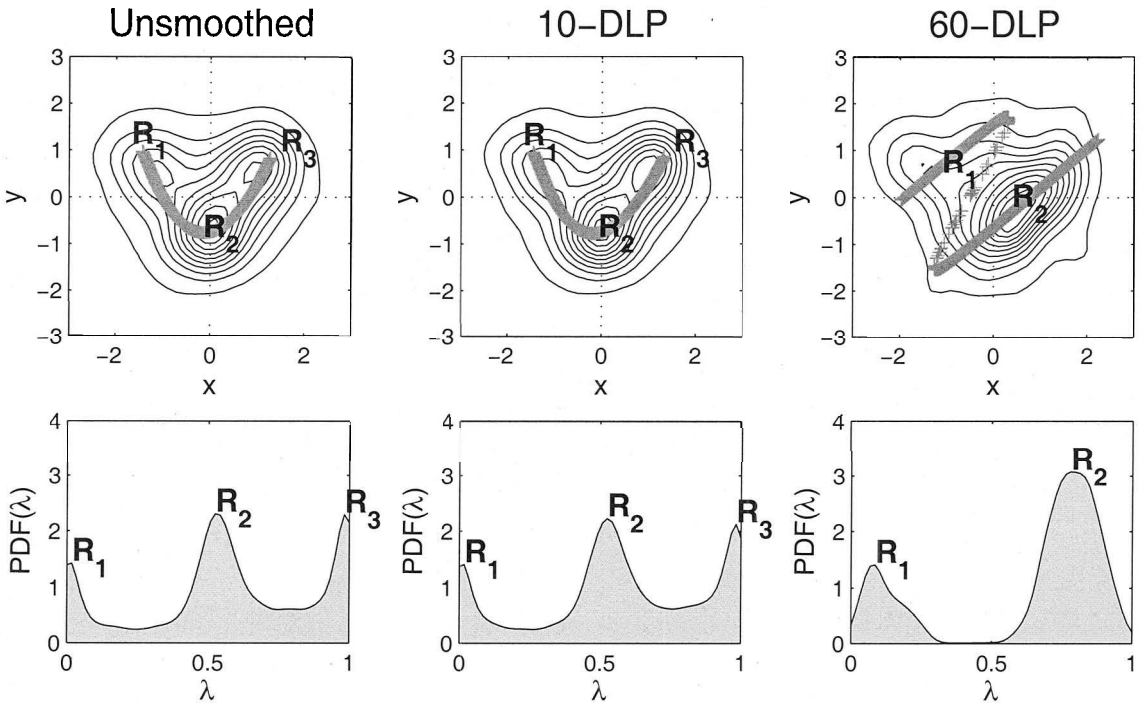

Figure 5.4: Leading nonlinear modes from the simple model given various low-pass cut-offs.

What happens then when the data is smoothed? Figure 5.4 (middle) shows that for a cut-off period near the intrinsic residence time of 7 days the approximation and λ distribution are essentially as in the unsmoothed case. On the other hand, Figure 5.4 (right) shows that when the cut-off period is much greater than the intrinsic residence

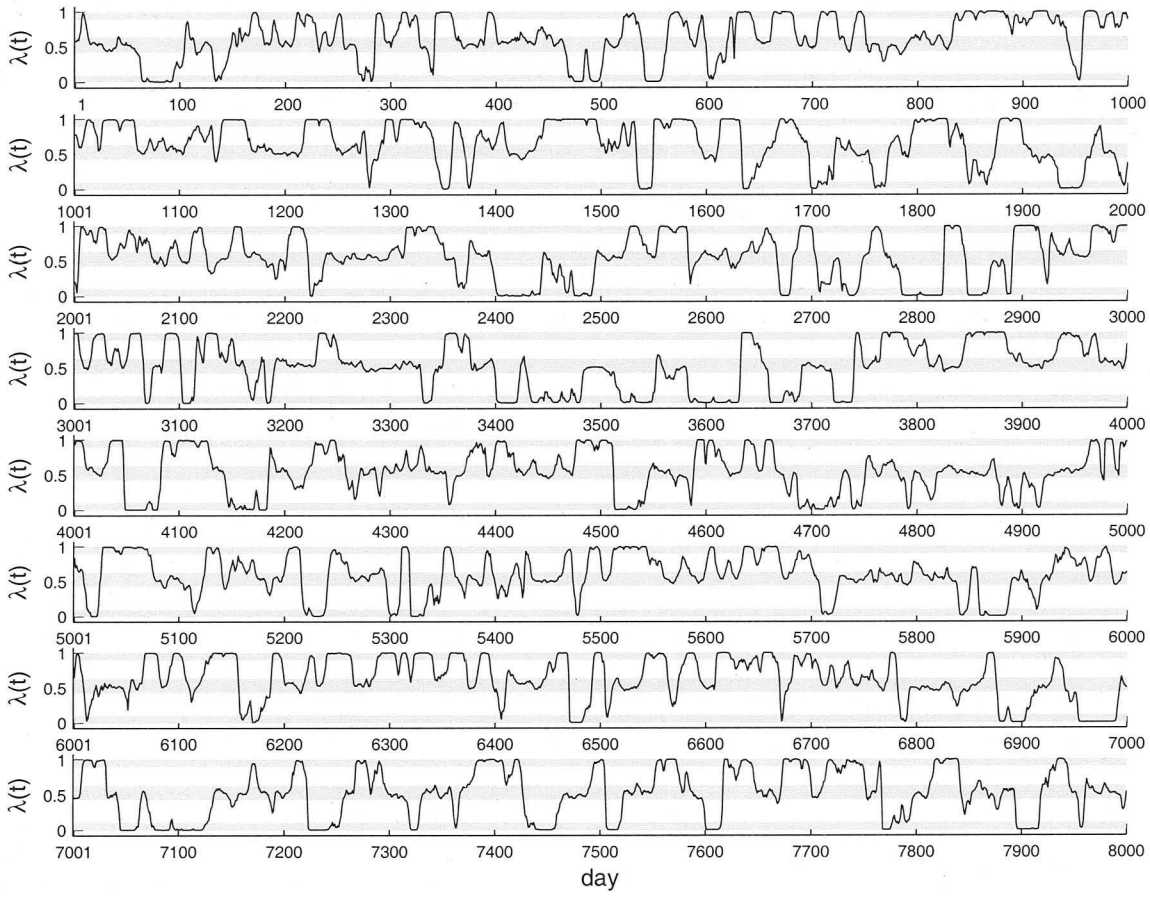

Figure 5.5: Distribution of the unfiltered NLPCA time series $\lambda(t)$ from the simple model. The shaded regions represent the $\lambda(t)$ intervals associated with the three designed regimes (or wells).

time the approximation becomes Z-shaped and the λ distribution bi-modal. In this case the smoothing mixes times spent in regime R_2 with times spent in regime R_3. This leads to the appearance of a "super-regime" which is seen in the λ distribution as the large peak to the right.

It is also interesting to note that in studies of the stratospheric circulation, Christiansen (2003) found two regimes in wintertime-averaged data while Monahan et al. (2003) found three regimes in 10-day low-pass filtered data. The results of this section suggest that the differences between these studies may arise from the considerably different averaging periods used.

Chapter 6

Conclusions

This study concerns atmospheric regimes as they have been observed in the recent past and simulated for the near future. Most previous studies of low-frequency atmospheric variability have been focused on the leading linear modes of variability as derived, for example, by linear PCA. With relatively recent diagnostic advances it is now possible to begin to explore in considerable detail the nonlinear structure inherent in atmospheric variability. In particular, in this study we employ the recently introduced nonlinear technique referred to as NLPCA. Previous studies employing NLPCA have determined that the atmosphere is fundamentally regime-like in the sense that there are a small number of regions of state space that are preferred over others. Characterizing and understanding these states, and the transitions between them, is an important step towards understanding low-frequency atmospheric variability in general.

The objectives of this study were to: 1) characterize the three dimensional spatial, temporal and dynamical signature of atmospheric regimes; 2) assess the ability of a state-of-the-art GCM to reproduce the observed atmospheric regimes and 3) deter-

mine the sensitivity of atmospheric regimes to increased CO_2 and sulphate aerosol radiative forcing. We also determined to reconcile the results of two previous studies using NLPCA. Monahan et al. (2000c) applied NLPCA to monthly mean SLP from a 1000-year control simulation of the CCCma CGCM1 and found two regimes. More recently, Monahan et al. (2001; 2003) applied NLPCA to observed 10-day low-pass filtered mid-tropospheric geopotential height and found three regimes. It was our aim to reconcile these studies.

The main results of this study are based on a NLPCA of 10-day low-pass filtered winter SLP. The observations are 42-years of NCEP/NCAR reanalyses for the period of Jan. 1, 1958 to Dec. 31, 1999. The model simulations are from the CCCma first generation coupled GCM and involve 100-year samples from long control and stabilization simulations. The control simulation has the equivalent CO_2 concentration fixed at 330 ppm. The stabilization simulations have the equivalent CO_2 and sulphate aerosol forcing fixed at values representative of years 2050 and 2100. The main results of the study are:

Observed regimes: There are three observed regimes, which we denote R_1, R_2 and R_3. Regime R_1 is characterized by a positive anomaly center over the Aleutians, a negative center over the Scandinavia and another positive center over the northeast Atlantic. Regime R_2 is characterized by negative anomalies extending from the northeast Pacific to Greenland together with positive anomalies over the northern Europe. Regime R_3 consists of a strong meridional dipole over the North Atlantic, which is reminiscent of the negative phase of the AO. The average time spent in each regime is about 7 days. Low- and high-frequency dynamics are both crucially involved in both the onset and break stages of regime evolution. Generally speaking, during onset, low-frequency dynamics are implicated in downstream development through

Rossby wave energy emission, propagation and absorption. High-frequency dynamics generally reinforce the primary regime centers through eddy-vorticity flux feedbacks during both onset and break. Therefore, the breakdown of the regimes can be largely attributed to low-frequency dynamics.

Simulated regimes: The control simulation similarly shows the existence of three regimes. The spatial, temporal and dynamical signatures of the simulated regimes are very similar to those in the observations. Analysis of separate 100-year samples from the long 1000-year control simulation reveals that 100-years of data adequately samples these regime states. It was also determined using the control simulation that the difference between Monahan et al. (2000c) and Monahan et al. (2001; 2003) lies in the different smoothing applied to the data. This was illustrated with a simple stochastic model, which revealed that the regime states are strongly affected when the smoothing time scale greatly exceeds the intrinsic residence time of the regimes.

Future regimes: The stabilization simulations similarly show the existence of three regimes; however, their spatial, temporal and dynamical signatures are altered. The atmosphere in the near future is predicted to become more regime-like and spatial structures of regimes undergo changes. While the changes in regime structures are noticeable, they are not altered unrecognizably. This result supports a qualified version of the hypothesis of Palmer (1999), who proposed that the residence frequencies rather than the spatial structures of atmospheric regimes may change significantly under global warming. In fact, it appears that the spatial structures change in their detailed structure, while retaining their essential features.

We conclude with a few remarks on the limitations of this study, and indicate some avenues for further investigation:

- The observed regimes characterized in this dissertation are based on the widely-used NCEP/NCAR reanalyses dataset. It would be useful to repeat these calculations with the European Centre for Medium-Range Weather Forecasts (ECMWF) reanalyses dataset which has recently become available.

- The simulated regimes characterized in this dissertation are based on a single coupled GCM. Given the various biases involved in any particular coupled GCM it would be useful to compare these simulated results against those obtained from other coupled GCMs.

- The main diagnostic technique used in this dissertation is NLPCA. It would be useful to directly compare these results against those obtained with other nonlinear diagnostic techniques. It should also be mentioned that NLPCA as implemented here stands to be refined and improved. For example, we have no guarantee that the results presented here reflect optimal solutions in terms of the method having obtained a global minimum.

- A number of the results described in this dissertation need further investigation to go beyond basic description and towards physical explanation. For example, it would be useful to know exactly why the regime residence times increase under global warming. Similarly, there are various aspects of the regime dynamics requiring more research. For example, why do the secondary regime structures involve negative synoptic eddy feedbacks, while the primary structures involve positive synoptic eddy feedbacks? The role of baroclinic processes, not just barotropic processes, also needs further investigation.

- Our results show that there may be preferred pathways for regime transition, as in Crommelin (2003a; 2004) using a highly simplified model and observa-

tions. Future work should be directed towards understanding these preferred pathways.

Bibliography

Ambaum, M. H. P., B. J. Hoskins, and D. B. Stephenson, 2001: Arctic oscillation or North Atlantic oscillation? *J. Clim.*, **14**, 3495-3507.

Andrews, D. G., and M. E. McIntyre, 1978: On wave-action and its relatives. *J. Fluid Mech.*, **89**, 647-664.

Bauer, F., 1951: Extended range weather forecasting. *Compendium of Meteorology*, American Meteorological Society, 814-833.

Black, R. X., 1997: Deducing anomalous wave source regions during the life cycles of persistent flow anomalies. *J. Atmos. Sci.*, **54**, 895-907.

Boer, G. J., G. Flato, M. C. Reader. and D. Ramsden, 2000a: A transient climate simulation with greenhouse gas and aerosol forcing: Experimental design and comparison with the instrumental record for the 20th century. *Clim. Dyn.*, **16**, 405-425.

Boer, G. J., G. Flato, and D. Ramsden, 2000b: A transient climate change simulation with greenhouse gas and aerosol forcing: Projected climate for the 21st century. *Clim. Dyn.*, **16**, 427-450.

Branstator, G., 1983: Horizontal energy propagation in a barotropic atmosphere with meridional and zonal structure. *J. Atmos. Sci.*, **40**, 1689-1708.

Branstator, G., 1984: The relationship between zonal mean flow and quasi-stationary waves in the midtroposphere. *J. Atmos. Sci.*, **41**, 2163-2178.

Branstator, G., 1985: Analysis of general circulation model sea-surface temperature anomaly simulations using a linear model. Part II: Eigenanalysis. *J. Atmos. Sci.*, **42**, 2242-2254.

Branstator, G., 1990: Low-frequency patterns induced by stationary waves. *J. Atmos. Sci.*, **47**, 629-648.

Branstator, G., 1992: The maintenance of low-frequency atmospheric anomalies. *J. Atmos. Sci.*, **49**, 1924-1945.

Branstator, G., 1995: Organization of storm track anomalies by recurring low-frequency circulation anomalies. *J. Atmos. Sci.*, **52**, 207-226.

Branstator, G., and J. D., Opsteegh, 1989: Free solutions of the barotropic vorticity equation. *J. Atmos. Sci.*, **46**, 1799-1814.

Charney, J. D. and J. G. DeVore, 1979: Multiple flow equilibria in the atmosphere and blocking. *J. Atmos. Sci.*, **36**, 1205-1216.

Cheng, X., and J. M. Wallace, 1993: Cluster analysis of the Northern Hemisphere wintertime 500-hPa height field: Spatial patterns. *J. Atmos. Sci.*, **50**, 2674-2696.

Christiansen, B., 2003: Evidence for nonlinear climate change: Two stratospheric regimes and a regime shift. *J. Clim.*, in press.

Corti, S., F. Molteni, and T. N. Palmer, 1999: Signature of recent climate change in frequencies of natural atmospheric circulation regimes. *Nature*, **398**, 799-802.

Crommelin, D. T., 2003a: Regime transitions and heteroclinic connections in a barotropic atmosphere. *J. Atmos. Sci.*, **60**, 229-246.

Crommelin, D. T., J. D. Opsteegh, and F. Verhulst, 2003b: A mechanism for atmospheric regime behavior. *J. Atmos. Sci.*, in press.

Crommelin, D. T., 2004: Observed non-diffusive dynamics in large-scale atmospheric flow. Submitted to *J. Atmos. Sci.*

Deser, C, 2000: On the teleconnectivity of the "Arctic Oscillation". *Geophys. Res. Lett.*, **27**, 779-782.

Dole, R. M., 1983: Persistent anomalies of the extratropical Northern Hemisphere wintertime circulation. *Large-Scale Dynamical Processes in the atmosphere*, B. J. Hoskins and R. P. Pearce, Eds., Academic Press, 95-109.

Dole, R. M., 1986: The life cycles of persistent anomalies and blocking over the North Pacific. *Advances in Geophysics*, **29**, Academic Press, 31-69.

Dole, R. M., 1989: Life cycles of persistent anomalies. Part I: Evolution of 500 mb height fields. *Mon. Wea. Rev.*, **117**, 177-221.

Dommenget D., and M. Latif, 2002: A cautionary note on the interpretation of EOFs. *J. Clim.*, **15**, 216-225.

Egger, J., and H.-D. Schilling, 1983: On the theory of the long-term variability of the atmosphere. *J. Atmos. Sci.*, **40**, 1073-1085.

Finnoff, W., F. Hergert, and H. G. Zimmermann, 1993: Improving model selection by nonconvergent methods. *Neural Networks*, **6**, 771-783.

Flato, G. M., G. J. Boer, W. G. Lee, N. A. McFarlane, D. Ramsden, M. C. Reader, and A. J. Weaver, 2000: The Canadian Centre for Climate Modelling and Analysis global coupled model and its climate. *Clim. Dyn.*, **16**, 451-467.

Fyfe, J.C., G. J. Boer, and G. M. Flato, 1999: The Arctic and Antarctic Oscillations and their projected changes under global warming. *Geophys. Res. Lett.*, **26**, 1601-1604.

Ghil, M. and A. W. Robertson, 2002: "Waves" vs. "particles" in the atmosphere's phase space: A pathway to long-range forecasting. *Proc. Natl. Acad. Sci.*, **99** (Suppl. 1), 2493-2500.

Hansen, A. R., and A. Sutera, 1986: On the probability density distribution of large-scale atmospheric wave amplitude. *J. Atmos. Sci.*, **43**, 3250-3265.

Horel, J. D., and J. M. Wallace, 1981: Planetary-scale atmospheric phenomena associated with the Southern Oscillation. *Mon. Wea. Rev.*, **109**, 813-829.

Hoskins, B. J., I. N. James, and G. H. White, 1983: The shape, propagation and mean-flow interaction of large-scale weather systems. *J. Atmos. Sci.*, **40**, 1595-1612.

Hoskins, B. J., D. J. Karoly 1981: The steady linear response of a spherical atmosphere to thermal and orographic forcing. *J. Atmos. Sci.*, **38**, 1179-1196.

Hoskins, B. J., A. J. Simmon, and D. C. Andrews, 1977: Energy dispersion in a barotropic atmosphere. *Quart. J. Roy. Meteor. Soc.*, **103**, 553-567.

Hsieh, W. W., and B. Tang, 1998: Applying neural network models to prediction and data analysis in meteorology and oceanography. *Bull. Amer. Meteor. Soc.*, **79**, 1855-1870.

Joseph, R., M. Ting, and P. Kushner 2003: The global stationary wave response to climate change in a coupled GCM. Submitted to *J. Clim.*.

Jung, T., M. Hilmer, E. Ruprecht, S. Kleppek, S. K. Gulev, and O. Zolina, 2003: Characteristics of the recent eastward shift of interannual NAO variability. *J. Clim.*, **16**, 3371-3382.

Kalnay, E. M., and co-authors, 1996: The NCEP/NCAR reanalysis project. *Bull. Amer. Meteor. Soc.*, **77**, 437-471.

Kang, I.-S., 1990: Influence of zonal mean flow change on stationary wave fluctuations. *J. Atmos. Sci.*, **47**, 141-147.

Kimoto, M., and M. Ghil, 1993a: Multiple flow regimes in the Northern Hemisphere winter. Part I: Methodology and hemispheric regimes. *J. Atmos. Sci.*, **50**, 2625-2643.

Kimoto, M., and M. Ghil, 1993b: Multiple flow regimes in the Northern Hemisphere winter. Part II: Sectorial regimes and preferred transitions. *J. Atmos. Sci.*, **50**, 2645-2673.

Kloeden, P. E., and E. Platen, 1992: Numerical solution of stochastic differential equations. Springer-Verlag, Berlin, 632pp.

Koopmans, L. H., 1974: The spectral analysis of time series. Academic Press. 366pp.

Kramer, M. A., 1991: Nonlinear principal component analysis using autoassociative neural networks. *AIChE J*, **37**, 233-243.

Lau, N. C., 1988: Variability of the observed midlatitude stormtracks in relation to low-frequency changes in the circulation pattern. *J. Atmos. Sci.*, **45**, 2718-2743.

Lu, J., and R. J. Greatbatch, 2002: The changing relationship between the NAO and northern hemisphere climate variability. *Geophys. Res. Lett.*, **29**, 1148, doi:10.1029/2001GL014052.

McFarlane, N. A., G. J. Boer, J. -P. Blanchet, and M. Lazare, 1992: The Canadian Climate Centre second-generation general circulation model and its equilibrium climate. *J. Clim.*, **5**, 1013-1044.

Metz, W., 1989: Low-frequency anomalies of atmospheric flow and the effects of cyclone-scale eddies: A canonical correlation analysis. *J. Atmos. Sci.*, **46**, 1026-1041.

Michelangeli, P. A., R. Vautard, and B. Legras, 1995: Weather regimes: Recurrence and quasi-stationarity. *J. Atmos. Sci.*, **52**, 1237-1256.

Mitchell, J. F. B., T. C. Johns, J. M. Gregory, and S. F. B. Tett, 1995: Climate response to increasing levels of greenhouse gases and sulphate aerosols. *Nature*, **376**, 501-504.

Mo, K. C., and M. Ghil, 1988: Cluster analysis of multiple planetary flow regimes. *J. Geophys. Res.*, **93**, 10927-10951.

Molteni, F., S. Tibaldi, and T. N. Palmer, 1990: Regimes in the wintertime circulation over northern extratropics. I: Observational evidence. *Quart. J. Roy. Meteor. Soc.*, **116**, 31-67.

Monahan, A. H., 2000a: Nonlinear principal component analysis by neural networks: theory and application to the Lorenz system. *J. Clim.*, **13**, 821-835.

Monahan, A. H., 2000b: Nonlinear principal component analysis of climate data. Ph.D. dissertation, Department of earth and ocean sciences, University of British Columbia, Vancouver, 159pp.

Monahan, A. H., J. C. Fyfe, and G. M. Flato, 2000c: A regime view of Northern Hemisphere atmospheric variability and change under global warming. *Geophys. Res. Lett.*, **27**, 1139-1142.

Monahan, A. H., L. Pandolfo, and J. C. Fyfe, 2001: The preferred structure of variability of the northern hemisphere atmospheric circulation. *Geophys. Res. Lett.*, **28**, 1019-1022.

Monahan, A. H., J. C. Fyfe, and L. Pandolfo, 2003: The vertical structure of wintertime climate regimes of the Northern Hemisphere extratropical atmosphere. *J. Clim.*, **16**, 2005-2021.

Nakamura, H., and J. M. Wallace 1990: Observed changes in the baroclinic wave activity during the life cycles of low-frequency circulation anomalies. *J. Atmos. Sci.*, **47**, 1100-1116.

Nakamura, H., and J. M. Wallace 1993: Synoptic behavior of baroclinic eddies during the blocking onset. *Mon. Wea. Rev.*, **121**, 1892-1903.

Nakamura, H., 1994, Rotational evolution of potential vorticity associated with a strong blocking flow configuration over Europe. *Geophys. Res. Lett.*, **21**, 2003-2006.

Nakamura, H., M. Nakamura, and J. L. Anderson, 1997: The role of high- and low frequency dynamics in the blocking formation. *Mon. Wea. Rev.*, **125**, 2074-2093.

Namias, J., 1950: The index cycle and its role in the general circulation. *J. Meteor.*, **7**, 130-139.

Namias, J., 1964: Seasonal persistence and recurrence of European blocking during 1958-1960. *Tellus*, **16**, 91-107.

Nigam, S., and R. S. Lindzen, 1989: The sensitivity of stationary waves to variations in the basic state zonal flow. *J. Atmos. Sci.*, **46**, 1746-1768.

Pacanowski, R. C., K. Dixon, and A. Rosati, 1993: The GFDL modular ocean model users guide. *GFDL Ocean Group Tech. Rep.*, **No. 2**. Geophysical Fluid Dynamics Laboratory, Princeton, USA, 46pp.

Palmer, T. N., 1999: A nonlinear dynamical perspective on climate prediction. *J. of Clim.*, **12**, 575-591.

Panagiotopoulos, F., M. Shahgedanova, and D. B. Stephenson, 2002: A review of Northern Hemisphere winter-time teleconnection patterns. *European Research Course on Atmosphere (ERCA)*, **5** (Ed. C. Boutron), J. Phys IV, 12 (PR10): 27-47, EDP Sciences, France.

Plumb, R. A., 1985: On the three-dimensional propagation of stationary waves. *J. Atmos. Sci.*, **42**, 217-229.

Press, W. H., S. A. Teukolsky, W. T. Vetterling, and B. P. Flannery, 1992: Numerical recipes in C. Cambridge University Press, 994pp.

Rex, D., 1950: Blocking action in the middle troposphere and its effect upon regional climate. *Tellus*, **2**, 196-211.

Shapiro, R. 1971: Smoothing, filtering and boundary effects. *Rev Geophys Space Phys*, **8**, 359-387.

Shutts, G. J., 1983: Propagation of eddies in diffluent jet streams: eddy vorticity forcing of blocking flow fields. *Quart. J. Roy. Meteor. Soc.*, **109**, 737-761.

Simmons, A. J., 1982: The forcing of stationary wave motion by tropical diabatic heating. *Quart. J. Roy. Meteor. Soc.*, **108**, 503-534.

Simmons, A. J., J. M. Wallace, and G. W. Branstator, 1983: Barotropic wave propagation and instability, and atmospheric teleconnection patterns. *J. Atmos. Sci.*, **40**, 1363-1392.

Smyth, P., K. Ide, and M. Ghil, 1999: Multiple regimes in Northern Hemisphere height fields via mixture model clustering. *J. Atmos. Sci.*, **56**, 3704-3723.

Takaya, K., and H. Nakamura, 2001: A formulation of a phase-independent wave-activity flux for stationary and migratory quasigeostrophic eddies on a zonally varying basic flow. *J. Atmos. Sci.*, **58**, 608-627.

Thompson, D. W., and J. M. Wallace, 1998: The Arctic Oscillation signature in the wintertime geopotential height and temperature field. *Geophys. Res. Lett.*, **25**, 1297-1300.

Thompson, D. W., and J. M. Wallace, 2000: Annular Modes in the extratropical circulation. Part I: Month-to-month variability. *J. Clim.*, **13**, 1000-1016.

Tsou, C.-H., and P. J. Smith, 1990: The role of synoptic/planetary- scale interactions during the development of a blocking anticyclone. *Tellus*, **42**, 174-193.

Ulbrich, U. and M. Christoph, 1999: A shift of the NAO and increasing storm track activity over Europe due to anthropogenic greenhouse gas forcing. *Clim. Dyn.*, **15**, 551-559.

Uryu, M., 1974: Mean zonal flows induced by a vertically propagating Rossby wave packet. *J. Meteor. Soc. Japan.*, **52**, 481-490.

Verkley, W. T. M., 1984: The construction of barotropic modons on a sphere. *J. Atmos. Sci.*, **41**, 2492-2504.

von Storch H., and F. W. Zwiers, 1999: Statistical analysis in climate research. Cambridge University Press, 494pp.

Walker, G. T. and E. W. Bliss, 1932: World Weather V. *Memoirs of the Royal Meteorological Society*, **4**, 53-83.

Wallace, J. M., 1996: Observed climatic variability: Spatial structure. *Decadal Climate Variability: Dynamics and Predictability*, D. Anderson and J. Willebrand, Eds., Elsevier, 31-81.

Wallace, J. M., and D. S. Gutzler, 1981: Teleconnections in the geopotential height field during the Northern Hemisphere winter. *Mon. Wea. Rev.*, **109**, 784-812.